



**INVESTIGATION OF FIELD-COLLECTED DATA USING DIFFUSE,
SPECULAR, FORWARD, AND REVERSE RADIATIVE TRANSFER MODELS**

THESIS
MARCH 2015

Dimitar M. Stoyanov
Second Lieutenant, USAF

AFIT-ENP-MS-15-M-100

DEPARTMENT OF THE AIR FORCE
AIR UNIVERSITY

AIR FORCE INSTITUTE OF TECHNOLOGY

Wright-Patterson Air Force Base, Ohio

DISTRIBUTION STATEMENT A.
APPROVED FOR PUBLIC RELEASE; DISTRIBUTION UNLIMITED.

The views expressed in this thesis are those of the author and do not reflect the official policy or position of the United States Air Force, Department of Defense, or the United States Government.

This material is declared a work of the U.S. Government and is not subject to copyright protection in the United States.

AFIT-ENP-MS-15-M-100

INVESTIGATION OF FIELD-COLLECTED DATA USING DIFFUSE AND
SPECULAR, FORWARD AND REVERSE RADIATIVE TRANSFER MODELS

THESIS

Presented to the Faculty

Department of Engineering Physics

Graduate School of Engineering and Management

Air Force Institute of Technology

Air University

Air Education and Training Command

In Partial Fulfillment of the Requirements for the

Degree of Master of Science in Applied Physics

Dimitar M. Stoyanov, BS

Second Lieutenant, USAF

March 2015

DISTRIBUTION STATEMENT A.
APPROVED FOR PUBLIC RELEASE; DISTRIBUTION UNLIMITED.

AFIT-ENP-MS-15-M-100

INVESTIGATION OF FIELD-COLLECTED DATA USING DIFFUSE AND
SPECULAR, FORWARD AND REVERSE RADIATIVE TRANSFER MODELS

Dimitar M. Stoyanov, BS
Second Lieutenant, USAF

Committee Membership:

Dr. M. A. Marciniak
Chair

Dr. M. T. Eismann
Member

Dr. J. Meola
Member

Abstract

This research focuses on investigating the effect of specular and diffuse properties of a set of eight materials on diffuse-only and diffuse-specular radiative transfer models in the wavelength range of 7-14 microns. The materials were selected and measured by the Sensors Directorate, Air Force Research Laboratory (AFRL/RV) as a set of panels in two orientations, flat and at 45° with respect to the ground, where the materials range in reflective and specular properties. The collected field data includes sky down-welling spectral radiance, ground spectral radiance, panel temperatures, and panel spectral reflected radiance at both orientations. The radiative transfer models used in this research use field- and laboratory-collected data to calculate the spectral reflected radiance from each panel. The laboratory-collected data is comprised of spectral hemispherical, specular, and diffuse directional reflectance (HDR, SDR, and DDR) at incident angles of 20°, 30°, 40°, 45°, 50°, 60°, and 70°, as collected by an SOC-100 HDR Reflectometer from Surface Optics Corporation. The modeled spectral reflected radiances are compared to field-collected spectral reflected radiances in order to gauge each radiative transfer model for its accuracy in modeling each panel. Additionally, a diffuse-only reverse radiative transfer model is developed and used in order to model the spectral HDR of the materials. The modeled spectral HDR values are compared to laboratory-collected spectral HDR data, and the reverse model is gauged for its accuracy in modeling each panel.

Acknowledgments

I would like to thank my advisor, Dr. Michael A. Marciniak, for his immense, continuing help and guidance during my research. Additionally, I would like to thank Dr. Joseph Meola for providing me with great data and periodic re-vectoring in the course of my work.

Dimitar M. Stoyanov

Table of Contents

	Page
Abstract	iv
Table of Contents	vi
List of Figures	ix
List of Tables	xiv
I. Introduction	1
General Issue	1
Problem Statement.....	2
Research Objectives /Hypotheses.....	3
Research Focus	4
Investigative Questions	4
Methodology.....	4
Assumptions/Limitations.....	5
Implications	6
Preview	6
II. Literature Review	7
Chapter Overview.....	7
Problems with Simple, Lambertian-Only Models.....	7
Interest in Remote Measurements	9
Summary.....	10
III. Theory	11
Chapter Overview.....	11
Interaction of Radiation with Matter	11
Kirchhoff's Radiation Law.....	12

Opaque Surfaces	13
Planck’s Blackbody Radiation Equation	13
Lambertian Approximation	14
Lambertian Sources	15
SOC-100 HDR Reflectometer and Reflectance Data.....	15
Simple Radiative Transfer Model (HDR only)	19
Expanded Radiative Transfer Model (HDR, DDR, and SDR).....	20
Diffuse-Only Reverse Radiative Transfer Model.....	22
Tipped-Panel Scene	22
Integration of Hemispherical Radiance	25
Trapezoidal Integration	28
Solar Irradiance	28
RMS Relative Difference Metric.....	32
Spectral Angle Mapper Metric	32
IV. Methodology	34
Chapter Overview.....	34
Field Data Collection.....	34
Infragold® Measurements	38
PLEXUS (using Modtran 4.0 V2R1)	47
Importing and Re-sampling Data	50
Radiative Transfer Model.....	50
Reverse Radiative Transfer Model.....	51
Model Angular Parameters.....	51

Summary.....	51
V. Analysis and Results	53
Chapter Overview.....	53
Accuracy of Spline Interpolation in Resampling of Data	53
Hemispherical Irradiance at Panel.....	55
Solar Contribution	57
Infragold® Modeling.....	58
Measured vs. Optimized Panel Temperatures	62
Diffuse-Only Radiative Transfer Model	64
Diffuse-Specular Radiative Transfer Model	75
Comparison of Diffuse-Only and Diffuse-Specular Models.....	86
PLEXUS as a Tool for Reverse Radiative Transfer Modeling	88
Reverse Radiative Transfer Model.....	89
Summary.....	91
VI. Conclusions and Recommendations	93
Chapter Overview.....	93
Investigative Questions Answered	93
Conclusions of Research	94
Significance of Research	95
Recommendations for Future Research.....	96
Appendix A.....	98
Appendix B	102
Appendix C	106
Bibliography	114

List of Figures

	Page
Figure 1. Irradiance Incident on a Surface.....	12
Figure 2. Schematic of the SOC-100 HDR Reflectometer.....	16
Figure 3. Simple Tipped-Panel Scene Geometry.....	23
Figure 4. Integration of Hemispherical (Sky and Ground) Radiance.....	26
Figure 5. Radiometry of a Solar Disk.....	29
Figure 6. Mean field-collected sky radiances.....	37
Figure 7. Standard deviation of the field-collected sky radiances.....	37
Figure 8. HDR, DDR, and SDR of an aged sample of Infragold®.....	40
Figure 9. Spectral reflected radiance of the flat Infragold® panel.....	41
Figure 10. Spectral reflected radiance of the 45° tipped Infragold® panel.....	42
Figure 11. Mean and standard deviation of the measured spectral reflected radiances from the flat Infragold® panel.....	43
Figure 12. Mean and standard deviation of the measured spectral reflected radiances from the 45° tipped Infragold® panel.....	43
Figure 13. HDR, SDR, and DDR of panel M8 (laminated safety glass) at 30° angle of incidence.....	45
Figure 14. HDR, SDR, and DDR of panel M1, flame-sprayed aluminum, at 10 microns, as a function of angle of incidence.....	46
Figure 15. Sky down-welling radiance at zenith for the mean field-collected and PLEXUS-generated data.....	48

Figure 16. Sky down-welling radiance at 30° from zenith for the mean field-collected and PLEXUS-generated data.	48
Figure 17. Sky down-welling radiance at 60° from zenith for the mean field-collected and PLEXUS-generated data	49
Figure 18. Sky down-welling radiance at 90° from zenith for the mean field-collected and PLEXUS-generated data.	49
Figure 19. Interpolated versus original data	55
Figure 20. Relative difference of PLEXUS sky irradiance data as compared between the hemispherical integration of four samples versus 91 samples	56
Figure 21. Solar and sky irradiance at panel M1 (flame-sprayed aluminum)	58
Figure 22. Measured and modeled spectral reflected radiances for the best matching case in modeling the measured reflected radiance from Infragold®.	59
Figure 23. Measured and modeled spectral reflected radiances for the worst matching case in modeling the measured reflected radiance from Infragold®	60
Figure 24. Measured and modeled reflected radiances at M12 (foamboard) for the diffuse-only model	63
Figure 25. The measured and modeled reflected radiances at M1 (flame-sprayed aluminum) for the diffuse-only model.	64
Figure 26. The measured and modeled reflected radiances at M9 (flame-sprayed aluminum) for the diffuse-only model.	64
Figure 27. The measured and modeled reflected radiances at M2 (320-grit sandpaper) for the diffuse-only model.	65

Figure 28. The measured and modeled reflected radiances at M10 (320-grit sandpaper) for the diffuse-only model.....	65
Figure 29. The measured and modeled reflected radiances at M3 (high emissivity, low reflectance material) for the diffuse-only model.....	66
Figure 30. The measured and modeled reflected radiances at M11 (high emissivity, low reflectance material) for the diffuse-only model.....	66
Figure 31. The measured and modeled reflected radiances at M4 (foamboard) for the diffuse-only model.	67
Figure 32. The measured and modeled reflected radiances at M12 (foamboard) for the diffuse-only model.	67
Figure 33. The measured and modeled reflected radiances at M5 (radiant barrier) for the diffuse-only model.	68
Figure 34. The measured and modeled reflected radiances at M13 (radiant barrier) for the diffuse-only model.	68
Figure 35. The measured and modeled reflected radiances at M6 (medium emissivity material) for the diffuse-only model.	69
Figure 36. The measured and modeled reflected radiances at M14 (medium emissivity material) for the diffuse-only model.	69
Figure 37. The measured and modeled reflected radiances at M7 (black vehicle paint) for the diffuse-only model.	70
Figure 38. The measured and modeled reflected radiances at M15 (black vehicle paint) for the diffuse-only model.....	70

Figure 39. The measured and modeled reflected radiances at M8 (laminated safety glass) for the diffuse-only model.....	71
Figure 40. The measured and modeled reflected radiances at M16 (laminated safety glass) for the diffuse-only model.	71
Figure 41. The measured and modeled reflected radiances at M1 (flame-sprayed aluminum) for the diffuse-specular model.	75
Figure 42. The measured and modeled reflected radiances at M9 (flame-sprayed aluminum) for the diffuse-specular model.	75
Figure 43. The measured and modeled reflected radiances at M2 (320-grit sandpaper) for the diffuse-specular model.	76
Figure 44. The measured and modeled reflected radiances at M10 (320-grit sandpaper) for the diffuse-specular model.	76
Figure 45. The measured and modeled reflected radiances at M3 (high emissivity, low reflectance material) for the diffuse-specular model.	77
Figure 46. The measured and modeled reflected radiances at M11 (high emissivity, low reflectance material) for the diffuse-specular model.	77
Figure 47. The measured and modeled reflected radiances at M4 (foamboard) for the diffuse-specular model.	78
Figure 48. The measured and modeled reflected radiances at M12 (foamboard) for the diffuse-specular model.	78
Figure 49. The measured and modeled reflected radiances at M5 (radiant barrier) for the diffuse-specular model.	79

Figure 50. The measured and modeled reflected radiances at M13 (radiant barrier) for the diffuse-specular model.	79
Figure 51. The measured and modeled reflected radiances at M6 (medium emissivity material) for the diffuse-specular model.	80
Figure 52. The measured and modeled reflected radiances at M14 (medium emissivity material) for the diffuse-specular model.	80
Figure 53. The measured and modeled reflected radiances at M7 (black vehicle paint) for the diffuse-specular model.	81
Figure 54. The measured and modeled reflected radiances at M15 (black vehicle paint) for the diffuse-specular model.	81
Figure 55. The measured and modeled reflected radiances at M8 (laminated safety glass) for the diffuse-specular model.	82
Figure 56. The measured and modeled reflected radiances at M16 (laminated safety glass) for the diffuse-specular model.	82

List of Tables

	Page
Table 1. Distances used in modeling solar irradiance at the Earth	31
Table 2. Mean HDR, SDR, DDR, and emissivity ε across the 7-14 μ m wavelength range for the eight panels at the angle of incidence of tipped panels (30°).	47
Table 3. Relative difference between measured and diffuse-only modeled reflected radiance of Infragold®, across the 7-14 μ m band.	60
Table 4. SAM values between measured and diffuse-only modeled reflected radiance of Infragold®, across the 7-14 μ m band.	61
Table 5. Mean and standard deviation of thermocouple temperatures, and diffuse-only optimized panel temperatures.	72
Table 6. Relative difference between measured and optimal panel temperatures using the diffuse-only model.	72
Table 7. Relative difference between measured and modeled diffuse-only reflected radiance data, across the 7-14 μ m band..	73
Table 8. SAM values between measured and modeled diffuse-only reflected radiance data.	73
Table 9. Mean and standard deviation of thermocouple temperatures, and diffuse- specular optimized panel temperatures.	83
Table 10. Relative difference between measured and optimal panel temperatures using the diffuse-specular model.	84
Table 11. RMS relative difference between measured and modeled diffuse-specular reflected radiance data.	84

Table 12. SAM values between measured and modeled diffuse-specular reflected radiance data.....	84
Table 13. Difference in RMS relative difference between measured and modeled reflected radiance between the diffuse-only and diffuse-specular models.	86
Table 14. Difference in spectral angles between the diffuse-only and diffuse-specular models.	87
Table 15. The mean relative difference between mean measured down-welling radiance and PLEXUS-generated down-welling radiance is presented per zenith angle.....	88
Table 16. Relative difference between SOC-100 reflectometer measured and reverse-modeled reflectance data for panels across 7-14 μ m.	89
Table 17. SAM values between SOC-100 reflectometer measured and reverse, diffuse-only modeled reflectance data for panels across 7-14 μ m.	90

INVESTIGATION OF FIELD-COLLECTED DATA USING DIFFUSE AND SPECULAR, FORWARD AND REVERSE RADIATIVE TRANSFER MODELS

I. Introduction

General Issue

Industry and researchers in the realm of remote sensing who have the select needs of detection and the accurate modeling of surfaces have often relied on various methods in order to represent the optical properties of materials. The optical properties of a material may vary greatly from point to point on its surface due to the randomness in geometry and the material composition, leading to an array of considerations that span a wide range of variables, such as angle of incidence, angle of reflection, and wavelength. This span of variables in turn is not only increasingly difficult to model accurately, but also very difficult to obtain, which begs for further research into the extent of complexity in radiative transfer models.

An ideal method for modeling of materials is the representation of a material's surface properties using bi-directional reflectance distribution functions (BRDFs) (Durikovic, 2014:87; Ientilucci, 2009:1-2). BRDFs are generally either empirical functions fit to observed data, or functions built from first principles, and sometimes partially built by intuition (Torrance, 1967:1108-1111; Shell, 2004:12-17). The functions model the amount of reflectance per solid angle that a surface has for any given angle of incidence, and at any given angle of reflectance. However, obtaining BRDF data for an array of materials is very demanding on time, as the reflectance of a surface has to be measured for every incident and reflected angle, and across a spectral range that is

sampled with a sufficiently small step size. Current methods of measuring BRDFs are not only time-consuming, but are also performed at one wavelength per measurement set, and so, the time required to acquire a spectral BRDF of a surface is very impractical and also potentially inaccurate for wavelength ranges outside of the particular measured wavelengths.

Problem Statement

It is very difficult to obtain and use spectral BRDFs due to aforementioned reasons, while the need to accurately model the spectral and reflective properties of materials has increased. One work indicative of this uses computer-based simulations of the BRDF of vegetation canopy as opposed to actual measurements, in order to determine how the reflectance of the canopies varies with different parameters (including row orientation, row distance, and phenological stage). The research culminates in showing that their system, the hyperspectral simulation of canopy reflectance (HySimCaR) is accurate, and able to be used as a replacement to BRDF measurements, where they claim that BRDF measurements are time-consuming and require specific instruments, though only for specific vegetation canopies (Kuester, 2014:2096:2106).

As commonly known, solar energy peaks in the visible, and not in the infrared bands, and has much less total power infrared bands when compared to thermal emissions. However, the solar contribution in a radiative transfer scene in the long-wave infrared (LWIR) has been shown to be significant under the right circumstances. This was done using a Lambertian and MERL nickel-shaped BRDF models (Butler, 2014:1-

10), suggesting that accurate BRDFs are required to account for the significance of the small amount of solar radiance in LWIR.

The end goal of modeling surfaces in this research is to construct a radiative transfer model which can calculate the total spectral reflected radiance from a given surface. This spectral reflected radiance is a function of incident sources of spectral radiance, the reflectance properties of the material (diffuse and specular), and the self-emission of the material. Therefore, this paper investigates the use of diffuse-only and diffuse-specular radiative transfer models to develop a baseline from which to judge the more-accurate spectral BRDF-based radiative transfer models.

Research Objectives /Hypotheses

The need to represent the spectral reflected radiance of a material using different radiative transfer models necessitates a code-based framework that may utilize data from different sources, and may use different modeling methods. This objective is necessitated in order to verify that the utilized models are able to represent different sets of data while maintaining a common trend in accuracy. One hypothesized trend is that the diffuse-specular radiative transfer model will be generally more accurate than the diffuse-only radiative transfer model, and that there will be materials for which the diffuse-only model will not be accurate. This determination has to be made by taking the average performance of each model across different sets of data, each of which represents different materials.

The accuracy of the diffuse-only and diffuse-specular radiative transfer models may best be gauged when compared to a spectral BRDF radiative transfer model.

However, since spectral BRDF data is not available, the simpler models have to be gauged against one another, and their accuracy is gauged against field-collected data.

Research Focus

This research focuses on analyzing field-collected data and comparing it against data generated by diffuse-only and diffuse-specular radiative transfer models.

Furthermore, the accuracy of each method is compared against the field-collected data, and appropriate conclusions are drawn. Additionally, a diffuse-only reverse radiative transfer model is carried out using the best-possible matching data in order to determine the feasibility of recognizing a material using remote sensing.

Investigative Questions

How accurate is a diffuse-only model in modeling the reflected radiance of materials? How does this accuracy vary across different materials?

How accurate is a diffuse-specular model, and is it better than the diffuse-only model, in modeling the reflected radiance of materials?

Can the current version of PLEXUS (using MODTRAN 4.0) be used to generate sky down-welling radiance for the modeling of reflected radiance of materials?

Is a diffuse-only reverse radiative transfer model feasible, and what are its performance characteristics when used to model a variety of materials?

Methodology

The investigative questions were answered by using a combination of field-collected, lab-collected, and modeled data in MATLAB® code in order to generate reflected radiances from a variety of materials, where each result was compared to the

actual, field-measured total radiance in the case of the forward radiative transfer models, and lab-measured material reflectance in the case of the reverse radiative transfer model.

In order to secure confidence in the final results, some of the methods used in the radiative transfer models, namely the resampling of data and integration of hemispherical radiance, were verified for their accuracy.

Lastly, the performance of all models of interest was gauged on a per-material basis in order to determine the best use for each model, and to identify possible improvements to the models.

Assumptions/Limitations

The primary assumption made for this research is that the field data is accurate and representative of the actual characteristics of the radiances present during the collection. Furthermore, I assume that the data collected in the lab setting, using the SOC-100 HDR Reflectometer, is also representative of the materials which were sampled.

Modeling the radiative transfer in a given scene would be ideal if comprehensive data is collected in regards to material reflectance, down-welling radiance from the atmosphere, and up-welling radiance from the surroundings of the material in question. The amount of data, however, is limited as the reflectance of materials is measured only at certain angles, the down-welling radiance is measured only at certain zenith angles, and the up-welling radiance from surrounding objects is not available. Furthermore, the collection of data is limited to the 7-14 μm range.

Implications

A success on the part of this research would improve the fidelity of radiative transfer models that may be used in computer-generated graphics and in remote sensing. Additionally, a success may indicate whether the specularity of a material may or may not be an important factor to consider in radiative transfer models.

Preview

The rest of the paper will outline the theory used for the research. Following this, the methodology used in generating data that will be presented in the analysis and results of the research will be explained. Lastly, the applicable conclusions that are drawn from the results are formed.

II. Literature Review

Chapter Overview

The purpose of this chapter is to introduce the points that Lambertian-only models are generally lacking in accurately modeling real scenes. Additionally, I show that there is an on-going interest in remote sensing, where the use of radiative transfer models is of importance.

Problems with Simple, Lambertian-Only Models

Lambertian-only models are known, by definition, to not be representative of realistic scenes. In some instances, the Lambertian-only model may be perfectly fine, such as when modeling very diffuse and non-specular surfaces, as is shown in this research. For many materials, however, the accuracy has been of question because the specular component of reflectance can significantly affect the observed radiance in or near specular observation directions (Ientilucci, 2009:6-7).

Another work indicative of this has shown that using only Lambertian reflectance was found to be insufficient in an array of angles. When attempting to model even the reflectance of diffuse white paint, the accuracy of the model decreased for angles near the specular reflection direction, even though the surface was roughened before application of the paint, to make it more diffuse (Earp, 2007:276-278). As one may guess, even new methods used in calculating radiative transfer take interest in the specularity of surfaces. A calculation method which minimizes on the use of ray-tracing for radiative transfer was shown to be different when accounting for the specular properties of the modeled surfaces, as opposed to using a Lambertian-only model. A comparison of the newly-

modeled data with known data showed that the specular model was more accurate (Sae, 2006:872-880).

On the note of generating surface images, it was found that stereo image analysis produces much more accurate data when taking into account the specular properties of materials for non-Lambertian surfaces. The results were shown to be far more accurate, with far fewer outliers, when the specular properties of the surfaces were accounted for, as stereo image analysis is generally much more accurate for diffuse (non-specular) surfaces (Wöhler, 2009:172).

Lastly, a paper characterizing silicon photodiodes has shown that silicon materials have a reflectance which is dependent on both the specular and diffuse properties of the material, which are important when properly modeling that reflectance. The specularity of the material was even shown to be wavelength dependent, where it has a linear change at wavelengths less than 950nm, but exponentially grows beyond 960nm (Xu, 2009:133-134), showing that Lambertian models may easily fail in certain wavelength ranges, even if they were observed to work properly at other wavelengths.

All of the aforementioned examples were performed in the lab environment, or using previous results to gauge computer-based models. This raises the hypothesis that the same case will be observed when using field-collected measurements, where models may be shown to be more accurate when considering the specular properties of non-Lambertian materials.

Interest in Remote Measurements

Remote sensing applications generally require as much accuracy as can be had when attempting to recognize materials at a distance. One such application is satellite imagery, where 3.7 μ m irradiance data from the Advanced Very High Resolution Radiometer (AVHRR) was used to gauge other measurements, such as collected data from Thekaekara and, separately, Fontenla. These measurements required accurate modeling of the bidirectional reflectance of the earth and atmosphere, upon which the verification of the data sets hinged (Platnick, 2007:124-125).

Established models that simulate down-welling radiance are also of importance. Two such models are MODTRAN 4 and S6, which were compared in atmospheric radiative transfer models, and gauged against each other. The models consistently produced up to 11% in error (as computed by the author) from one another when more complex parameters were being used, but the error would drop to 1% when the models were simplified (by taking steps such as assuming no aerosols), (Callieco, 2011:1367-1368). This raises significant questions on the reliability of either of the radiative transfer software, though MODTRAN 4 is shown to be accurate when using more computationally-intensive algorithms, in a separate paper. However, this required that custom-made algorithms be used in order to uncouple MODTRAN 4's atmospheric optical parameters from the surface reflectance (Guanter, 2009:1420). This further raises questions on whether PLEXUS, a utility designed to simplify the use of MODTRAN 4, would be able to easily model atmospheric down-welling radiance, and more generally whether MODTRAN 4 is reliable without making scenario-specific modifications to its code. Regardless, the tool continues to be used by researchers for the modeling of down-

welling radiance, for purposes such as the investigation of adjacency effects in radiative transfer models (Yang, 2009:6020).

Interestingly, and as is the case in this paper, some researchers take the step of making direct and situational measurements of down-welling radiance, as opposed to using modeling software to simulate such radiances. The author of one such paper stated that modeling software have difficulty in accurately generating sky radiance and solar irradiance from given meteorological parameters (Wilson, 2008:1943).

Summary

In summary, there is a lot of interest in accurate remote sensing applications, which largely hinges on properly accounting for the reflective properties of materials. This means that non-Lambertian models should be used, the first step of which is to include the specular reflection of materials. Modeling software, however, should be used very carefully and with caution due to the difficulty in accurately representing down-welling radiance. Fortunately, this research included measured down-welling radiances, and is only partly focused on attempting to use PLEXUS to reproduce these measurements.

III. Theory

Chapter Overview

The purpose of this chapter is to present basic theory and the theory behind approximations and the models used for this research. Additionally, a BRDF-based representation of spectral reflected radiance is simplified into the models used in this paper. Lastly, the operation and use of a relevant device, a reflectometer, is explained.

Interaction of Radiation with Matter

The interaction of radiation with matter can be explained, in a simple form, by use of the law of conservation of energy. As depicted in Figure 1, the law states that the energy E_o incident onto a surface must equal the sum of the transmitted, absorbed, and reflected energies, given as $E_o\tau$, $E_o\alpha$, and $E_o\rho$, respectively, such that

$$E_o = E_o\tau + E_o\alpha + E_o\rho \quad (1)$$

where the coefficients τ , α , and ρ are, respectively, the transmittance, absorptance, and reflectance of the material. Dividing both sides of equation (1) by E_o yields

$$1 = \tau + \alpha + \rho \quad (2)$$

It is important to remember what is actually happening at the boundary – a set of transverse electromagnetic waves is interacting with the atoms and molecules of which the surface is comprised. This means that the waves will interact differently with this surface depending on of what atoms and molecules it is made, and depending on what frequencies the waves have. Because of this, the coefficients in equation (2) are better

presented as $\tau(\lambda)$, $\alpha(\lambda)$, and $\rho(\lambda)$. The wavelength dependence becomes especially important to remember in the next section, Kirchhoff's Radiation Law.

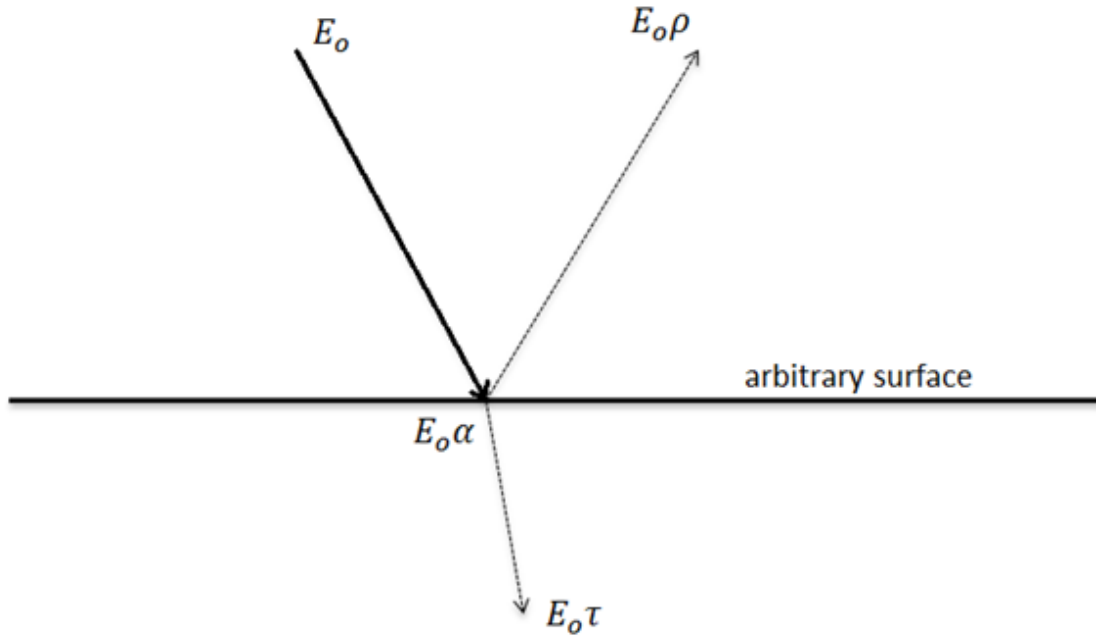


Figure 1. Conservation of energy demands that all energy, E_o , that is incident on a surface, must equal the sum of the transmitted, absorbed, and reflected energies, which are $E_o\tau$, $E_o\alpha$, and $E_o\rho$, respectively. The coefficients τ , α , and ρ are, respectively, the transmittance coefficient, absorbance coefficient, and reflection coefficient of the surface.

Kirchhoff's Radiation Law

Kirchhoff's radiation law is of specific importance to this thesis. The law states that, at thermal equilibrium, a material's spectral emissivity, the fraction of radiance it would emit compared to that of a blackbody at the same temperature, is equivalent to its spectral absorptance. Due to Kirchhoff's law, the following spectral relationship is established:

$$\varepsilon(\lambda) = \alpha(\lambda) \quad (3)$$

Opaque Surfaces

Opaque surfaces are those which do not transmit any energy. Thus, all energy is either absorbed or reflected. This is represented by equation (2), where $\tau = 0$, such that

$$\alpha(\lambda) = 1 - \rho(\lambda) \quad (4)$$

More importantly, conservation of energy coupled with Kirchhoff's radiation law allow a relationship to form between the emissivity, $\varepsilon(\lambda)$, and the reflectance, $\rho(\lambda)$, of the material, such that

$$\varepsilon(\lambda) = 1 - \rho(\lambda) \quad (5)$$

Planck's Blackbody Radiation Equation

A blackbody's spectral radiance L_{bb} is expressed by Planck's radiation law, and is given as

$$L_{bb}(\lambda, T) = \frac{2hc^2}{\lambda^5} \frac{1}{e^{\frac{hc}{\lambda kT}} - 1} \quad (6)$$

where h is Planck's constant, c is the speed of light, λ is the wavelength, k is Boltzmann's constant, and T is the temperature of the applicable material. Considering the self-emission of a surface, the radiance, L_{self} , may be represented using equations (5) and (6), such that

$$L_{self}(\lambda, T) = \varepsilon(\lambda)L_{bb}(\lambda, T) \quad (7)$$

$$L_{self}(\lambda, T) = (1 - \rho(\lambda))L_{bb}(\lambda, T) \quad (8)$$

Lambertian Approximation

The reflected spectral radiance from a surface can be very accurately given by the use of spectral BRDFs, where the spectral radiance in each observation direction (given by reflected radiance angles θ_r and ϕ_r) is the sum of the fractions of all of the incident spectral irradiance sources, E_i , that originated from the incident direction (given by angles θ_i and ϕ_i) that were strictly reflected in the given observation direction by the material's BRDF f_{BRDF} . This is given by

$$L_r(\theta_r, \phi_r, \lambda) = f_{BRDF}(\theta_i, \phi_i, \theta_r, \phi_r, \lambda) \cdot E_i(\theta_i, \phi_i, \lambda) \quad (9)$$

Not only are spectral BRDFs difficult and time-consuming to obtain, but as one may expect, they are also computationally intensive. The most common simplification to equation (9) is to disregard any dependence on angles. As such, the incident spectral irradiance is summed over all incident directions, and the outbound spectral radiance is considered to be Lambertian. Due to this, the reflectance $\rho(\lambda, \theta_i, \phi_i)$ can be defined by

$$\begin{aligned} \rho(\theta_i, \phi_i, \lambda) \\ = \int_0^{2\pi} \int_0^{\frac{\pi}{2}} f_{BRDF}(\theta_i, \phi_i, \theta_r, \phi_r, \lambda) \cos(\theta_r) \sin(\theta_r) d\theta_r d\phi_r \end{aligned} \quad (10)$$

$$\rho(\theta_i, \phi_i, \lambda) = \pi f_{BRDF}(\theta_i, \phi_i, \lambda) \quad (11)$$

It is understood that L_r is now independent of the outbound angles (θ_r and ϕ_r), and that the sine term in the integral of equation (10) accounts for the solid angle

calculation, while the cosine term accounts for the projected source area as off-normal angles are integrated. Of course, it is important to note that because of the cosine term, the calculated term is π when the spectral radiance is calculated over 2π steradians. The reflected radiance L_r is then given by

$$L_r(\lambda) = \frac{\rho(\lambda, \theta_i, \phi_i)}{\pi} E_i(\lambda, \theta_i, \phi_i) \quad (12)$$

Lambertian Sources

The Lambertian approximation may be used when propagating all of the reflected/emitted spectral radiance of a source to another element at some distance. The Lambertian approximation, in that respect, allows one to carry the total radiance L of a material outside of the solid angle integral (just as before), such that the flux at some point in space is given by

$$\Phi = \int L dA \int \cos(\theta) \sin(\theta) d\theta d\phi \quad (13)$$

If the source is a Lambertian hemisphere, the incident irradiance E_i may be calculated, similarly to equation (10), as

$$E_i = L_i \int_0^{2\pi} \int_0^{\frac{\pi}{2}} \cos(\theta_i) \sin(\theta_i) d\theta_i d\phi_i \quad (14)$$

$$E_i(\lambda) = \pi L_i(\lambda) \quad (15)$$

SOC-100 HDR Reflectometer and Reflectance Data

The SOC-100 HDR Reflectometer by Surface Optics Corporation, without modifications, collects hemispherical directional reflectance (HDR), diffuse directional

reflectance (DDR), and specular directional reflectance (SDR). Using a blackbody as a radiance source, each measurement involves the comparison of spectral reflected radiance, at a given reflectance angle, between a given sample and a gold reference. Measurements can also be polarized (parallel and perpendicular) or unpolarized. The blackbody source's radiance reaches the sample stage by the use of a gold hemi-ellipsoidal mirror as shown in Figure 2, where the source blackbody and the sample stage are positioned in the two foci of the hemi-ellipsoid, whose reflectance is taken to be flat, at 1, across the wavelength spectrum of interest. Each measurement returns the spectral reflectance of a sample as measured against the gold reference standard.

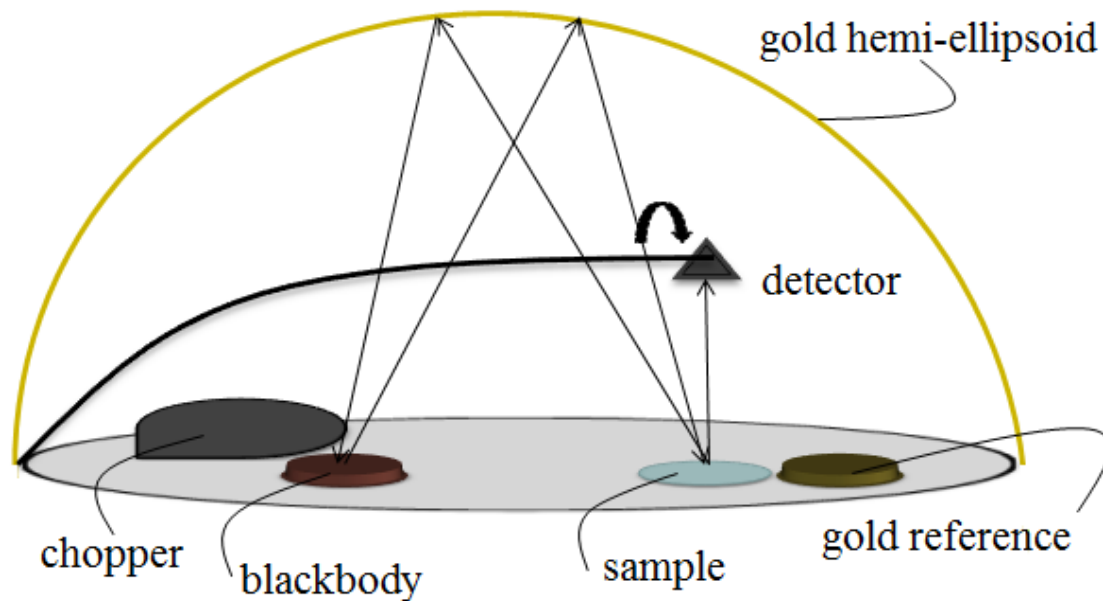


Figure 2. A reflectance measurement is taken from a sample by comparing its reflected radiance with that of a gold reference, when illuminated by a source blackbody. The illumination is possible by use of a reflecting gold-plated hemi-ellipsoid, where the foci are at the blackbody and at the sample/reference. A chopper is used to block off the source blackbody's radiance in order to take a reference reading of the sample's self-emission, which is subtracted out to acquire the sample's reflectance.

Reflected Radiance Measurement

A measurement of HDR is taken by measuring the amount of reflected radiance of a given sample, $L_{r-sample}$, to the reflected radiance from a gold reference, L_{r-gold} . Furthermore, each measurement is performed by taking two readings: one where the source blackbody is covered by a blackbody chopper (considered ‘on’), and one where the source blackbody is not covered (considered ‘off’). This additional step is taken in order to account for the self-emission of the sample. The HDR is then given by

$$\rho_{sample} \approx \frac{L_{r-sample-off} - L_{r-sample-on}}{L_{r-gold-off} - L_{r-gold-on}} \rho_{gold} \quad (16)$$

This measurement is then repeated for each desired reflectance angle of measurement by moving the detector, where the effective measurement range of the angles is 6° to 80° with respect to the sample normal. Any measurement beyond the effective range of angles is unreliable due to limitations in the device, as listed in the device's manual (“SOC-100 User’s Manual”:1).

Repeated Measurements

The SOC-100 reflectometer allows for increasing the number of measurements, whereby the reflected radiance from the gold reference is re-measured, or increasing the number of scans, where only the sample is re-measured using an even number of scans (as the sample has to be measured once with the chopper occluding the source blackbody and once with the chopper away from the source blackbody). In other words, two measurements with eight scans means that, for each measurement angle, the SOC-100

will measure the gold reference once, perform four scans with the chopper actuated and four scans with the chopper un-actuated, and repeat this one more time for a total of two 'measurements.'

The inherent noise in the SOC-100 reflectometer has been noted to decrease with an increasing number of measurements and/or scans, as would be commonly expected. However, there was no noted difference between a change in the number of scans per measurement versus the number of measurements, when considering the total number of scans performed (i.e., one measurement with 32 scans is equivalent to four measurements with eight scans). However, the time required to measure a sample is higher with an increased number of measurements than it is with a proportionally increased number of scans. Furthermore, the noise in measurements is sufficiently reduced with a total number of 32 scans, leading to the conclusion that optimal data collection is performed at one measurement with 32 scans.

Hemispherical Directional Reflectance

Each regular measurement of the SOC-100 reflectometer results in a value corresponding to the HDR of the material. This is different from a BRDF measurement in that the HDR measurement corresponds to integrated incident radiance, as the sample is illuminated by the source blackbody, and from all directions due to the gold, reflective hemi-ellipsoidal mirror. The BRDF integrated over a 2π Sr incident hemisphere is equal to the HDR, so using HDR inherently means that information is lost in regards to the radiance incident from particular directions.

Additionally, it is worth noting that the HDR of a material is interchangeable with

the directional hemispherical reflectance (DHR) of that material, as the BRDF produces the same result when integrated over either the incident or outbound angles for diffuse reflectors (Eismann, 2012:Ch 5, 33).

Diffuse Directional Reflectance and Specular Directional Reflectance

The SOC-100 reflectometer measures diffuse directional reflectance (DDR) by using a motorized beam blocker to stop the radiance of the source blackbody in the specular measurement direction, where “specular” is defined as the solid angle subtended by the beam blocker in the specular direction. Thus, only the non-specular radiance is allowed to illuminate the sample during measurement. With each such measurement, the collection software automatically acquires the specular directional reflectance (SDR) by taking the difference between the HDR and DDR, where the SDR is given by

$$\rho_{SDR} = \rho_{HDR} - \rho_{DDR} \quad (17)$$

Simple Radiative Transfer Model (HDR only)

A simple radiative transfer model can be made by taking all of the expected contributions to the incident irradiance on a panel and modeling the reflected radiance using only the HDR of the given material. If the reflected radiance is considered to only be diffuse, then equation (12) applies to this case with the addition of the reflection coefficient, ρ , given as ρ_{HDR} .

The sources of irradiance given by E_i in equation (12) are listed in the next section. Adding the self-emission of the panel, from equation (8), yields

$$L = L_r(\lambda) + L_{self}(\lambda) \quad (18)$$

$$L = \rho_{HDR}(\lambda) \frac{E_i(\lambda)}{\pi} + (1 - \rho_{HDR}(\lambda))L_{bb}(\lambda, T) \quad (19)$$

Expanded Radiative Transfer Model (HDR, DDR, and SDR)

The simple radiative transfer model can be expanded by accounting for the specular reflectance of a material. This requires that the data for the SDR of the material is known, which can be provided by a device such as the SOC-100 reflectometer. Since the HDR, as shown in equation (17), is the sum of the DDR and SDR, expanding the model requires that the HDR be split into its DDR and SDR components, where each one acts upon the respective radiance. The DDR is applied to the sum of all radiance incident onto a material, while the SDR is applied to only the portion of the radiance incident on the sample that is taken to be from the specular direction. The reflected radiance from a hemisphere L_{r-hemi} (such as from the atmosphere), under the expanded model, is given by

$$L_{r-hemi} = \rho_{DDR} \frac{E_{hemi}}{\pi} \quad (20)$$

where the material is taken to be a Lambertian reflector when using DDR, ρ_{DDR} is the diffuse reflectance, and E_{hemi} is the irradiance incident from the observable hemisphere as seen by a flat facet of the material.

The reflected radiance from the specular component of the material's reflectance L_{r-spec} is the radiance that a viewing detector would be observing when looking at the material when the material is essentially acting as a mirror across the spectrum. Of course, the material is not a mirror, and the SDR captures this spectral behavior. The specular reflected radiance L_{r-spec} is thus given as

$$L_{r-spec} = \rho_{SDR} L_{spec} \quad (21)$$

The extended radiative transfer model also includes the radiance contribution from the sun, $L_{r-solar}$. The contribution is applied to the Lambertian, diffuse reflectance of the material, and is given by

$$L_{r-solar} = \rho_{DDR} \frac{E_{solar}}{\pi} \quad (22)$$

where E_{solar} is the solar irradiance as attenuated by an atmospheric transmittance τ_a . In the case where the solar irradiance is in the specular viewing direction, then the specular reflectance, ρ_{SDR} is used in equation (22) in place of the diffuse reflectance, ρ_{DDR} .

Combining all of the aforementioned pieces leads to a total reflected radiance L_r given by

$$L_r = L_{r-hemi} + L_{r-solar} + L_{r-spec} \quad (23)$$

$$L_r = \frac{\rho_{DDR}}{\pi} (E_{hemi} + E_{solar}) + \rho_{SDR} L_{spec} \quad (24)$$

Lastly, any material has self-emission given as in equation (8),

$$L_{self} = L_{bb} (1 - \rho_{HDR}) \quad (25)$$

where L_{bb} is a blackbody emission at the material's temperature, and the emissivity ϵ of the material is given by

$$\epsilon = 1 - \rho_{HDR} \quad (26)$$

Thus, the total radiance L outbound from an object, in this expanded radiative transfer model, is

$$L = L_r + L_{\text{self}} \quad (27)$$

$$L = \frac{\rho_{DDR}}{\pi} (E_{\text{hemi}} + E_{\text{solar}}) + \rho_{SDR} L_{\text{spec}} + L_{bb}(1 - \rho_{HDR}) \quad (28)$$

Diffuse-Only Reverse Radiative Transfer Model

The HDR of a material may be determined by using a reverse radiative transfer model. In order to do this, equation (19) is rearranged to solve for ρ_{HDR} , such that

$$L = \rho_{HDR}(\lambda) \frac{E_i(\lambda)}{\pi} + L_{bb}(\lambda, T) - \rho_{HDR}(\lambda) L_{bb}(\lambda, T) \quad (29)$$

$$L - L_{bb}(\lambda, T) = \rho_{HDR}(\lambda) \left(\frac{E_i(\lambda)}{\pi} - L_{bb}(\lambda, T) \right) \quad (30)$$

$$\rho_{HDR}(\lambda) = \frac{L - L_{bb}(\lambda, T)}{\frac{E_i(\lambda)}{\pi} - L_{bb}(\lambda, T)} \quad (31)$$

Tipped-Panel Scene

An actual scene needs to be considered in order to make use of the radiative transfer model. For this, consider a flat panel of arbitrary size placed at some tipping angle, θ_{tip} , with respect to the ground's plane (the x - y plane), as shown in Figure 3.

The viewing vector r_v at which a specular reflection is observed is given by the angle θ_{obs} , which is the complementary to the zenith angle, and φ_{obs} , the azimuth angle as taken from the x -axis, towards the y -axis. It is important to note that the $-y$ -axis is

presented in the figure, as opposed to its positive counterpart, which means that the setup uses a right-handed coordinate system. This choice was made so that the tipping rotation would be performed about the y -axis when the panel is observed in the shown orientation.

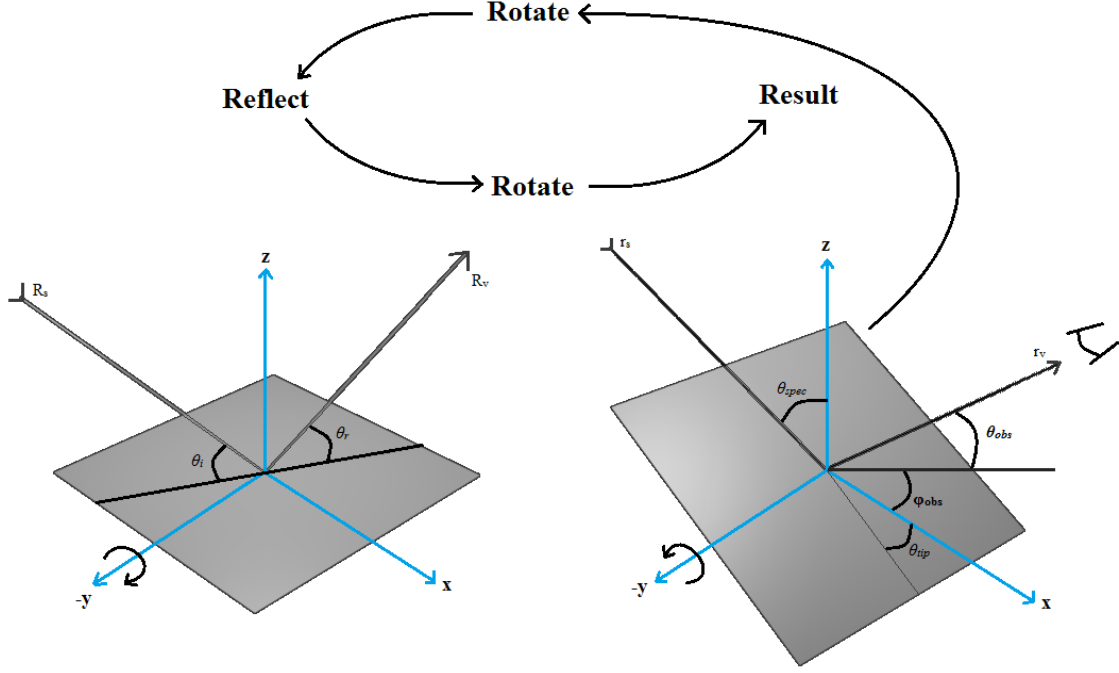


Figure 3. The viewing vector r_v , as given by the viewing angles θ_{obs} and ϕ_{obs} , is rotated into the coordinate system of the tipped panel, which is tipped by an angle θ_{tip} with respect to the ground (x - y plane), to acquire the rotated viewing angle R_v . This vector is then reflected using the law of reflection, $\theta_r = \theta_i$, to acquire the rotated specular source vector R_s . Finally, R_s is rotated into the original coordinate system to produce the specular source vector r_s , which contains all information needed to calculate the specular source angle θ_{spec} as given from zenith.

The source of the specular reflection is described by the specular source vector r_s , which is used to determine the angle θ_{spec} as extended from zenith. The angle θ_{spec} is sufficient in describing the specular source as the used sky and ground radiances are azimuthally independent, removing the need of an azimuthal angle. To obtain θ_{spec} , r_v is constructed from the viewing angles θ_{obs} and ϕ_{obs} , and then is rotated about the y -axis

using the rotation matrix R , as given in equations (32) and (33), which produces the rotated viewing angle R_v .

$$R_v = Rr_v \quad (32)$$

$$R_v = \begin{bmatrix} \cos(\theta_{tip}) & 0 & \sin(\theta_{tip}) \\ 0 & 1 & 0 \\ -\sin(\theta_{tip}) & 0 & \cos(\theta_{tip}) \end{bmatrix} r_v \quad (33)$$

After the initial rotation, the rotated specular source vector, given by R_s , is determined using the law of reflection, $\theta_r = \theta_i$, by applying a reflection matrix on the transformed viewing vector, R_v , such that

$$R_s = \begin{bmatrix} 1 & 0 & 0 \\ 0 & 1 & 0 \\ 0 & 0 & -1 \end{bmatrix} R_v \quad (34)$$

The vectors are then rotated about the y-axis in the reverse direction, again by θ_{tip} , in order to transform the rotated specular source vector back to the original coordinate system, such that

$$r_s = \begin{bmatrix} \cos(-\theta_{tip}) & 0 & \sin(-\theta_{tip}) \\ 0 & 1 & 0 \\ -\sin(-\theta_{tip}) & 0 & \cos(-\theta_{tip}) \end{bmatrix} R_s \quad (35)$$

Lastly, the specular source angle θ_{spec} is calculated using the specular source vector and the appropriate trigonometric relationships, as given in equation (36), where \hat{x} , \hat{y} , and \hat{z} are the unit vectors in the direction of the x-axis, y-axis, and z-axis, respectively.

$$\theta_{spec} = 90^\circ - \tan^{-1} \left(\frac{r_s \cdot \hat{z}}{\sqrt{(r_s \cdot \hat{x})^2 + (r_s \cdot \hat{y})^2}} \right) \cdot \frac{360^\circ}{2\pi} \quad (36)$$

The specular source angle θ_{spec} is used to determine which points of data must be used from the available sky and ground down-welling radiance data.

Integration of Hemispherical Radiance

For the field experiments, the spectral irradiance on a material is calculated by assuming the surrounding atmosphere may be approximated as an azimuthally-symmetric hemisphere broken into rings of some angular width $d\theta$. For a flat material, the hemisphere can expectedly be entirely the atmosphere. For a tipped material, however, the hemisphere will be a combination of atmosphere and ground. This inevitably changes the amount of radiance incident on the material, not only because the atmosphere becomes optically thicker at higher angles with respect to zenith, but also because the ground is most commonly a Lambertian blackbody. The proper integration of the hemispherical spectral radiance into incident spectral irradiance requires a more complicated approach.

As is shown in Figure 4, a point at the origin will have a hemispherical view such that zenith is oriented directly upwards as seen on the page. Assuming that the sky radiance has azimuthal symmetry (i.e., it is independent of the phase angle), the radiance can be integrated without azimuthal dependence in the top region (green). This region's irradiance, E_{ind} , is given simply as

$$E_{ind} = \int_0^{2\pi} \int_0^{\theta_{tip}} L(\theta, \lambda) \cos(\theta) \sin(\theta) d\theta d\varphi \quad (37)$$

where the calculation is much like the one performed for the Lambertian approximation, as shown in equation (14).

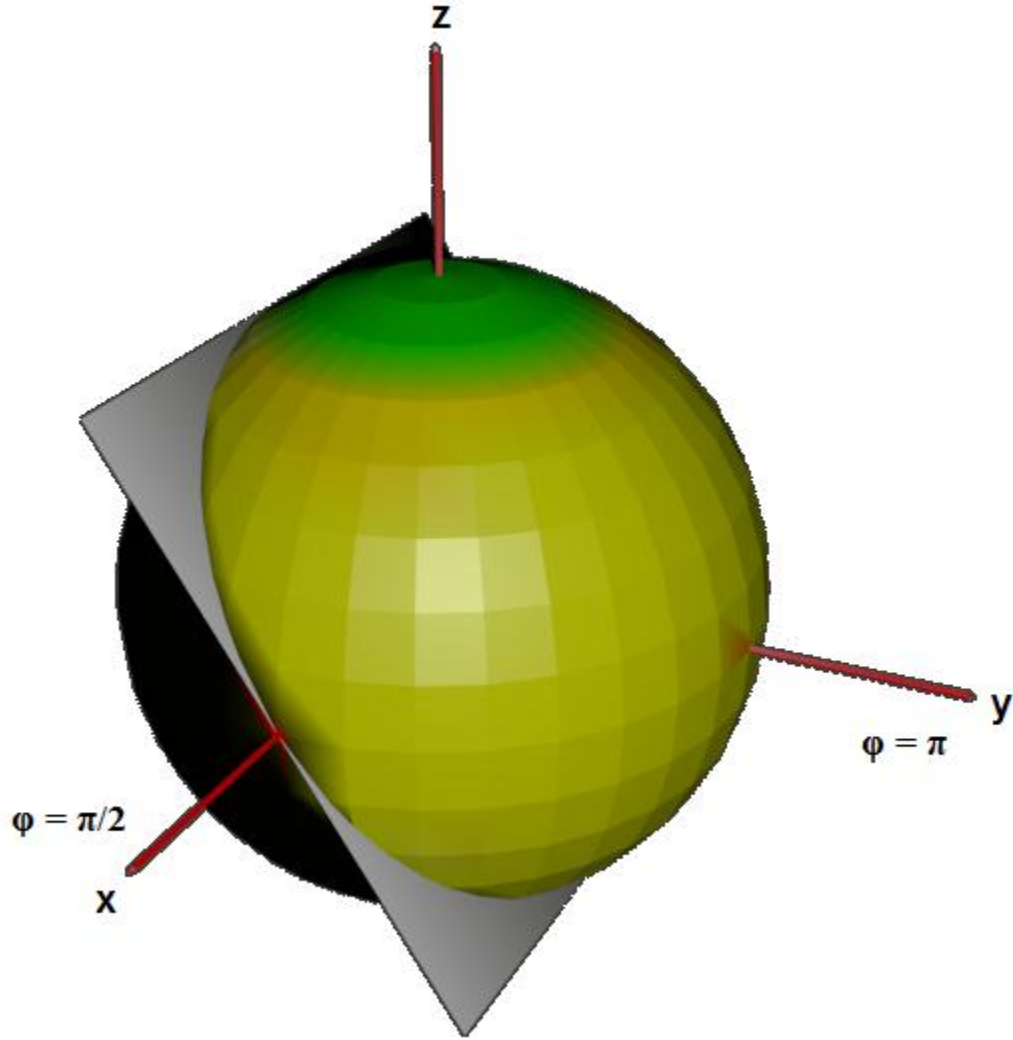


Figure 4. The portion of the sphere to the right of the intersecting plane represents a hemisphere surrounding the center point of the plane. The top region represents the φ -independent portion of the integration. The integration over the rest of the hemisphere is dependent on φ , which complicates the integration. In a real setting, the hemisphere is cut in two pieces by the x-y plane, where the upper piece is the solid angle subtended by the atmosphere and the lower piece is the solid angle subtended by the ground.

Integrating over the rest of the hemisphere (yellow region) requires the integration to be modified to account for the dependence on the initial angle φ , as it is no longer

spanning the whole 2π range. As shown in Figure 4, θ is at 90° when that elevation angle is pointing along the y axis. Here, φ only covers a region from $\pi/2$, through π , to $3\pi/2$. Additionally, as the hemisphere is itself azimuthally symmetric, one may calculate only half of the integration and multiply it by two. As such, the angle φ may span the range of $\varphi_{initial}$ to π . A fair bit of geometry shows that

$$\phi_{initial} = \cos^{-1}\left(\frac{\tan(\theta_{tip})}{\tan(\theta)}\right) \quad (38)$$

Lastly, since the sky and ground likely do not have spectral radiances that can be represented by a single smooth function, they must be integrated separately. Due to the problem setup, the sky-ground boundary is precisely at 90° in θ . The sky-borne irradiance, E_{sky} , is therefore the sum of equation (37) and the integration of the φ -dependent region, and is given as

$$E_{sky} = E_{ind} + 2 \int_{\theta_{tip}}^{\frac{\pi}{2}} \int_{\cos^{-1}(\frac{\tan(\theta_{tip})}{\tan(\theta)})}^{\pi} L(\theta, \lambda) \cos(\theta) \sin(\theta) d\theta d\varphi \quad (39)$$

The ground portion E_{gnd} is, similarly, given as

$$E_{gnd} = 2 \int_{\theta_{tip}}^{\frac{\pi}{2}} \int_0^{\cos^{-1}(\frac{\tan(\theta_{tip})}{\tan(\theta)})} L(\theta, \lambda) \cos(\theta) \sin(\theta) d\theta d\varphi \quad (40)$$

Equations (39) and (40) come together in order to form E_{hemi} as presented in equation (28), and this is given as

$$E_{hemi} = E_{sky} + E_{gnd} \quad (41)$$

Trapezoidal Integration

For this research, trapezoidal integration was utilized in order to perform the integrals shown in equation (39) such that the sky is broken up into azimuthally-symmetric rings. As such, the integration limits of the zenith angle, θ , were broken up into the respective regions as necessitated by available data (0° , 30° , 60° , and 90° in zenith). It is important to use a sufficiently-small step size for the integration such that the trapezoids match the actual data as smoothly as possible. As such, the sky radiance data was interpolated from the aforementioned angles to 91 points, corresponding to 0° to 90° .

Solar Irradiance

There are numerous ways to model the irradiance given by the Sun. The choice for this paper is to model the Sun as a Lambertian blackbody disk at a distance of 1 astronomical unit from the Earth. Using equation (6), the Sun's radiance is given as

$$L_{solar} = \frac{2hc^2}{\lambda^5} \frac{1}{e^{\frac{hc}{\lambda k T_{sun}}} - 1} \quad (42)$$

where the T_{sun} is the Sun's temperature, which is taken to be 5778 K. Because the Sun is so far from the Earth, it is a sufficiently-accurate practice to assume one astronomical unit as the distance, and to take the Sun's irradiance as delivered onto the solid angle subtended by the Earth (as opposed to the solid angle subtended by a particular panel). The solid angle approximation, of course, assumes that the irradiance of the Sun does not vary much from one point on the Earth to another. However, the tilt at which a panel is placed with respect to the solar irradiance is important and is taken into account.

The solar flux delivered to the Earth is given by, using equation (13),

$$\Phi_{solar} = \int L_{solar} dA \int \int \sin(\theta) d\theta d\phi \quad (43)$$

Since the Sun is considered to be a flat disk, the solar radiance L_{solar} is also independent of the area, and can be pulled out of the integral completely. The double integral over the area then becomes nothing more than the area of the solar disk. The second double integral represents the solid angle subtended by the Earth, where θ is the angle which extends from the on-axis line to the edge of the Earth's area, and ϕ represents the radial portion of the integration, as shown in Figure 5.

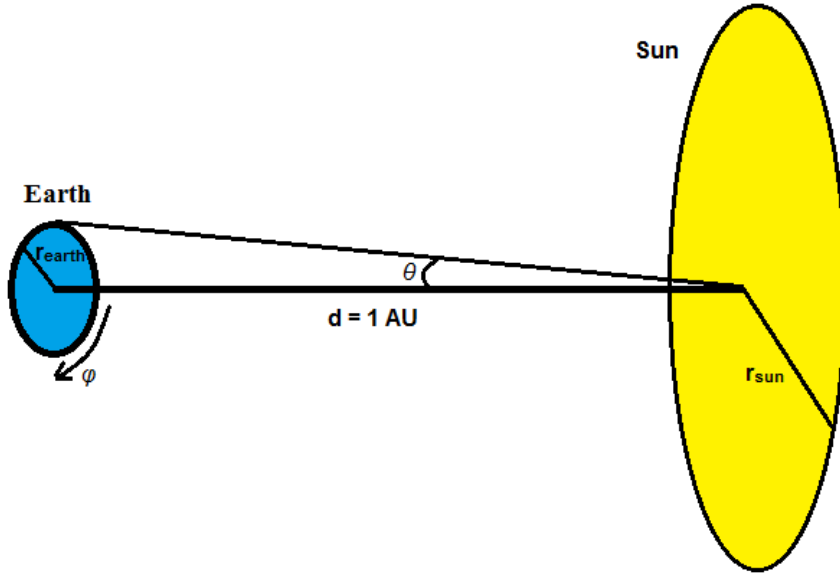


Figure 5. A solar disk of radius r_{sun} emits radiance towards the Earth, with radius r_{earth} from a distance d of 1 AU. The distance is so large that a small angle approximation can be made such that the angle θ varies insignificant amounts when drawn from any point of the Sun towards the Earth's edge. The same reasoning can be applied to justify disregarding which point on the Earth is actually of interest, as they all receive approximately the same amount of flux.

To calculate the flux received at the Earth, populate equation (43) to account for the parameters of interest. The flux is then given by

$$\Phi_{solar} = L_{solar} A_{sun} \int_0^{2\pi} \int_0^{\theta_{max}} \sin(\theta) d\theta d\phi \quad (44)$$

$$\Phi_{solar} = L_{solar} \pi r_{sun}^2 \cdot 2\pi(1 - \cos(\theta_{max})) \quad (45)$$

With a little geometry, θ_{max} can be calculated as

$$\theta_{max} = \arctan\left(\frac{r_{earth}}{d}\right) \quad (46)$$

Thus, the solar flux delivered to the Earth is

$$\Phi_{solar} = 2\pi^2 r_{sun}^2 \left(1 - \cos\left(\arctan\left(\frac{r_{earth}}{d}\right)\right)\right) L_{solar} \quad (47)$$

The fact that the distance between the Sun and the Earth is much larger than either the Sun's or the Earth's radius allows the use of the small angle approximation (in regards to θ) such that it can be assumed that the irradiance delivered to one point on the Earth is nearly indistinguishable from that delivered to another point. In other words, the solar irradiance E_{solar} is independent of the differential area element of the Earth, and is therefore given as

$$E_{solar} = \frac{\Phi_{solar}}{A_{earth}} \tau_a = \frac{\Phi_{solar}}{\pi r_{earth}^2} \tau_a \quad (48)$$

where τ_a is the atmospheric transmittance.

Plugging in the solar flux yields

$$E_{solar} = 2\pi \frac{r_{sun}^2}{r_{earth}^2} \left(1 - \cos\left(\arctan\left(\frac{r_{earth}}{d}\right)\right)\right) L_{solar} \tau_a \quad (49)$$

The last piece to be included results from the fact that the projected area upon which the Sun is radiating may be smaller than the total area of an irradiated panel.

Therefore, E_{solar} must be scaled by the cosine of the angle between the panel's normal \hat{n}_p , and the solar irradiance source's normal, \hat{n}_s , where both normal vectors are unit vectors with a magnitude of 1. Geometrically, the angle between them is represented by the relationship

$$\cos(\hat{n}_p, \hat{n}_s) = \hat{n}_p \cdot \hat{n}_s \quad (50)$$

where the unit vectors may be presented in terms of the angles θ_s and φ_s , and θ_p and φ_p , which are the elevation and azimuth angles of the source and panel vectors, respectively.

Equation (49), scaled by equation (50), is now ready to be used in the radiative transfer model as given by equations (19) and (28). The values utilized for equation (49) are listed in Table 1.

Table 1. Distances used in modeling solar irradiance at the Earth

	Length (km)
r_{sun}	695,800
r_{earth}	6,371
d	149,597,871

RMS Relative Difference Metric

This research involves comparing two spectra – one measured and one modeled – in order to gauge the accuracy of the tested models with the measured data. The overall accuracy can be gauged using a per-wavelength relative root-mean-square difference of the measured, L_{meas} , versus the modeled, L_{model} , spectral reflected radiances, given as

$$RMS = \sqrt{\frac{1}{N} \sum_i \left[\frac{L_{model}(\lambda_i) - L_{meas}(\lambda_i)}{L_{meas}(\lambda_i)} \right]^2} \quad (51)$$

where N is the total number of points across the wavelength spectrum, and λ_i is the wavelength at each measured (or modeled) point i . Equation (51) may also be used for any other spectra, such as the measured and modeled spectral reflectance of a material.

It is important to note that the RMS metric is much more reliable in showing the relative difference in magnitudes between the two spectra (per wavelength) than it is showing the accuracy in spectral features. For this reason, a second metric – Spectral Angle Mapper (SAM) – is utilized.

Spectral Angle Mapper Metric

The spectral angle mapper metric gauges how well measured and modeled reflected radiances compare spectrally, though it loses information on the magnitudes of the radiances. For this research in particular, this is done by allowing every wavelength within the spectra to be represented as its own dimension, where the measured and modeled spectra are represented as 1-dimensional vectors. The spectral angle, r_{SAM} , is then given as the angle between the two vectors (Eismann 2012:Ch 14, 31-32), such that

$$r_{SAM} = \cos^{-1} \left(\frac{L_{model} \cdot L_{meas}}{\|L_{model}\| \|L_{meas}\|} \right) \quad (52)$$

The smaller that the angle between the two vectors is, the more alike they are spectrally. Again, this metric may also be used for spectral reflectance as opposed to spectral reflected radiance. Also, since the relative RMS difference metric loses spectral information, while the SAM metric loses information in magnitude, the two methods combined provide a clear picture of how well two spectra compare.

IV. Methodology

Chapter Overview

The purpose of this chapter is to outline the origin of applicable data, and how that data is used in the radiative transfer models. First is presented information about the field-collected data, which includes sky down-welling radiance, panel reflected radiances, panel temperatures, and Infragold® reflected radiances. Next, the lab-collected (using the SOC-100 HDR Reflectometer) reflectance data for a sample of each material is presented, followed by a discussion on the generation of sky down-welling radiance and atmospheric transmittance using PLEXUS.

Much of the collected and generated data do not have the same resolutions, necessitating the subsequent discussion of how all data is imported and re-sampled. After, the models which utilize this data – forward and reverse radiative transfer models – are discussed, followed by a short discussion on the specific geometry utilized within the models.

Field Data Collection

An array of data was collected in a real setting. The data includes the spectral reflected radiance (in the range of 7-14 μ m) from eight different panels, where the collection occurred with one set of panels flat against the ground (surface normal pointing at zenith), while a second set of panels was tipped at 45° with respect to zenith. The observation angle of the collection was loosely kept the same from panel to panel, at approximately 45° in azimuth (from the panel normal's projection onto the ground plane), and 40° in zenith. As a truth-check, an Infragold® panel was also positioned next

to each panel and measured at the same angle at which each panel was measured. The Infragold® measurements were used primarily to verify that the radiative transfer models function properly.

The panels ranged in emissivity, reflectance, and specularity. The flat panels are designated as M1 through M8, while their tipped equivalents are M9 through M16. Sky spectral radiance (also at 7-14 μ m) was collected next to each of the panels at angles of -30°, 0°, 30°, 60°, 90°, and 105° with respect to zenith, where the 105° measurement is considered to be the ground measurement. It is important to note that the 105° angle is not the only one pointing at ground, but that the 90° angle also observes ground due to hilly terrain. Figure 6 shows the mean sky radiance data from each angle calculated from all the measurements, while Figure 7 shows the respective standard deviations. The shown standard deviations range from 25 to 225 μ W/cm²Sr μ m, largely due to both the increase in ambient temperatures and the change in cloud profiles with time. The ambient temperatures would be expected to be the dominant effect, but one would expect that if that was the case, then the standard deviation of the 30° zenith case would be much more like the 0° and 60° cases. The fact that it is not suggests that cloud profiles must have had a significant temporal effect on the down-welling radiances. Each set of measurements took an average of 17 minutes to take, in the following order: down-welling measurements, tipped panel reflected radiance, tipped Infragold® reflected radiance, flat Infragold® reflected radiance, and flat panel. The time between the first down-welling measurement and the reflected radiance of the tipped panel averaged 4 minutes. Therefore, it can be expected that there were at least 4 minutes between the first down-welling measurement and the measurement of Infragold® and panel reflected

radiances, allowing more time for the down-welling radiance to change before those reflected radiance measurements are made.

The measurements were performed between approximately 1600 and 1800 GMT, where the ambient temperatures ranged from 18C to 22C, and the sky was partly cloudy. The temperature values were downloaded from online databases for the location of the field collection and used to model the self-emission of the Infragold® panels, as unlike the rest of the materials, the Infragold® did not have thermocouples.

The solar position at the date and location of measurements ranged (over the precise time of collection) approximately from 57° to 42° in zenith, and 113° to 147° in azimuth, respectively, where North is considered 0° in azimuth (and is 180° off from the tipped panel's normal projection, as the tipped panel faced South). The corresponding specular reflections for flat panels were away from the observing FTIR for all angles, as the solar reflection headed due North, while the FTIR was positioned South of the panels. The tipped panels (tipped towards South) had a solar specular reflection angles ranging from 70° to 55° in zenith, to 235° to 206° in azimuth, respectively, and were calculated using rotation matrices given in the Tipped-Panel Scene section in Chapter III, where both ranges are outside of the observation orientation of the FTIR, resulting in negligible solar contributions.

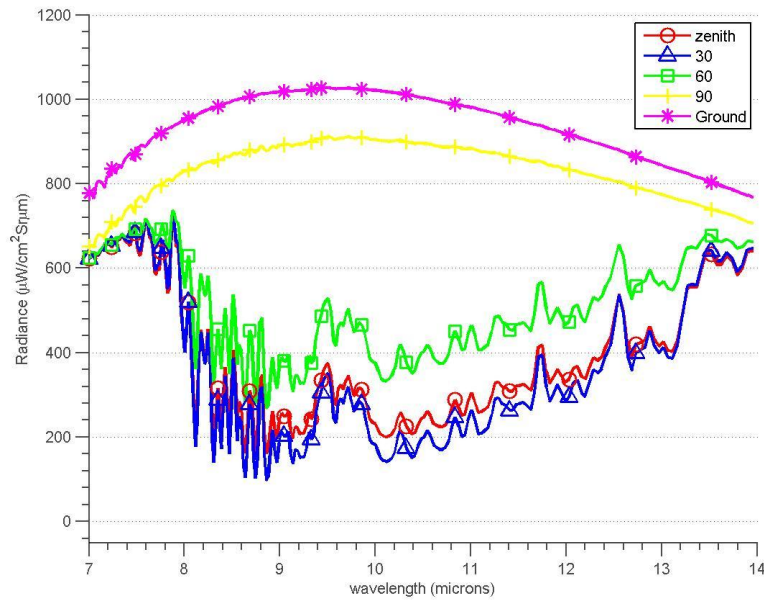


Figure 6. The mean field-collected sky radiances are shown. Though more data was gathered, only the data of interest, zenith, 30°, 60°, and 90° from zenith, and ground radiance is included. This data contributes to the reflected radiance that is modeled.

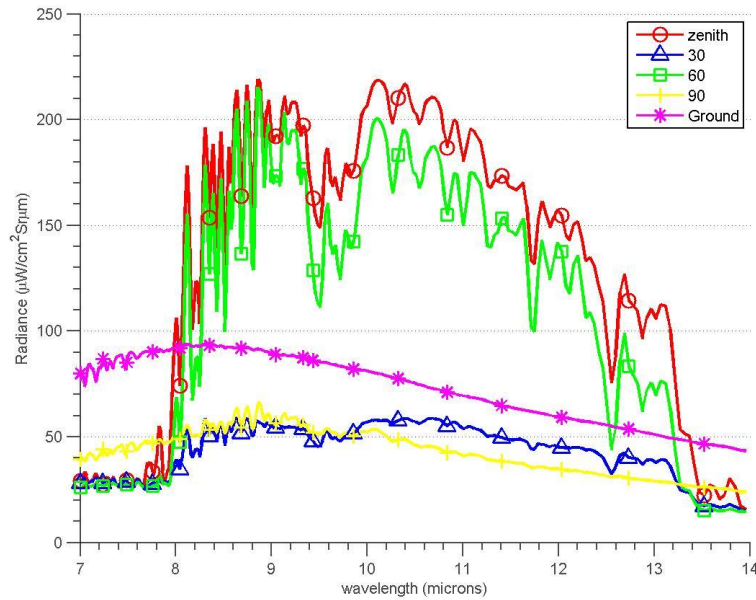


Figure 7. The standard deviation of the field-collected sky radiances are shown. Though more data was gathered, only the data of interest - zenith, 30°, 60°, and 90° from zenith, and ground radiance - is included. This data contributes to the reflected radiance that is modeled.

Lastly, every panel had five thermocouples from which temperature readings were taken. The temperature measurements (and their standard deviations) were averaged from five thermocouples on each panel, giving a single measurement temperature and a corresponding standard deviation, across each panel's thermocouples. These will be presented in Chapter V. The standard deviation for each panel was divided by the measured temperature, and an average across all panels was taken, giving an average panel temperature measurement uncertainty of 1.74%. This value represents a quantitative measurement of how, on average, the thermocouple temperatures deviated from the average for each thermocouple set.

Infragold® Measurements

The Infragold® spectral reflected radiance measurements were used as a sanity-check for the diffuse-only and diffuse-specular forward models. A pristine sample of Infragold® was not available for reflectance measurements with the SOC-100, so it was assumed that its HDR is spectrally flat with a reflectance of 0.94 as presented on the company's website, for the 7-14 μ m band. It is important to note here that the reflectance of the Infragold® cannot be backed out using field-collected measurements because, again, the temperature of the panel is unknown. As such, both modeling the reflected radiance of Infragold® and modeling the reflectance of Infragold® will produce results that are dependent on the modeled self-emission of the Infragold® panel. Therefore, a choice was made to only model the reflected radiance of the Infragold® for each measurement made in the field, and to gauge the variation in accuracy by comparing the modeled reflected radiance to measured reflected radiances.

An older sample of Infragold® was measured, and is shown in Figure 8. The sample is still spectrally flat, but it is also of lower reflectance than what is advertised on the company's website. This may be owed to the fact that the sample may be considered aged and/or weathered. However, in order to best represent the reflectance of the Infragold®, a quantity for SDR or DDR is required to augment the accepted HDR of 0.94. Therefore, the assumption is made that the aged sample has specularity still indicative of the specularity of the field-used Infragold®. As such, the SDR can be given as approximately a flat value of 0.06, which is calculated by taking the product of the accepted HDR by the ratio of the mean SDR/HDR of the aged sample across the wavelengths. The reflectance may be represented as a single number without much loss (for all wavelengths) in accuracy since the aged sample is mostly spectrally flat.

No measurements were made of the temperature of the field-used Infragold®, which largely complicates the goal of producing accurate modeled spectral reflectances. Though the Infragold® itself may have a very high reflectance, it was contained within a wooden frame that would drive the temperature of the material to higher values, producing a source of error, albeit a small one as the emissivity of the material is low due to Kirchoff's Law. As mentioned previously, the ambient temperatures were utilized to represent the Infragold® temperature throughout the date, though a flat 10°C were added so that the values would float near the thermocouple temperatures of the next most reflective material, the radiant barrier M5.

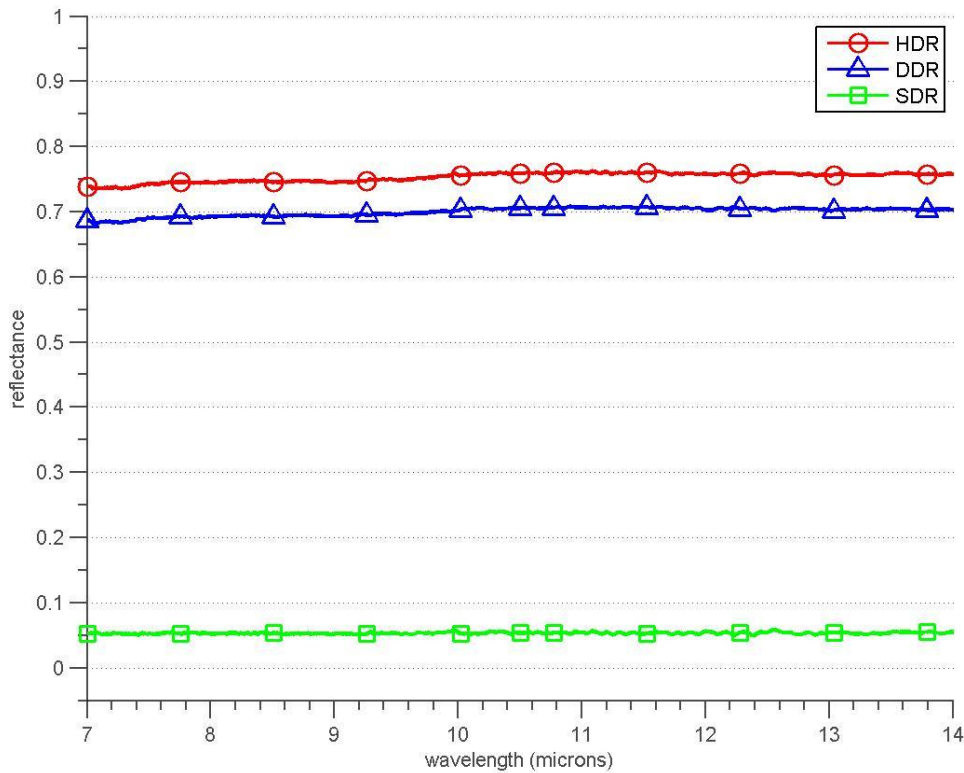


Figure 8. This plot shows the HDR, DDR, and SDR of an aged sample of Infragold®. Though it does not reach an HDR of 0.94 (as presented for Infragold® on the producer’s website), it is expectedly spectrally flat, and it does have a low specular ratio of SDR/HDR as the HDR is above 0.7 and the SDR is below 0.1.

The collected Infragold® data is presented in Figures 9 and 10, where the flat and tipped panel measurements are ranked in order of measurement by time. The measured radiances, however, did not increase in order of time. Since the ambient temperatures changed smoothly and in one direction, one would expect the same to happen with the radiance reflected from the Infragold® panels, as the down-welling radiance can be expected to change smoothly with time. This is not the case, leaving only the changing cloud cover as the external source in variation of down-welling radiance.

Figures 11 and 12 present additional data – the mean and standard deviation of flat and tipped (at 45°) Infragold® panels. The deviation of the radiance ranges between approximately 20 and 90 $\mu\text{W}/\text{cm}^2\text{Sr}\mu\text{m}$ for the flat measurements, and 20 and 80 $\mu\text{W}/\text{cm}^2\text{Sr}\mu\text{m}$ for tipped measurements. A portion of the deviations are owed to the changing ambient temperatures, thereby increasing the down-welling radiance, though some is also attributed to the changing cloud cover, as the measured radiance did not increase in time in a single direction.

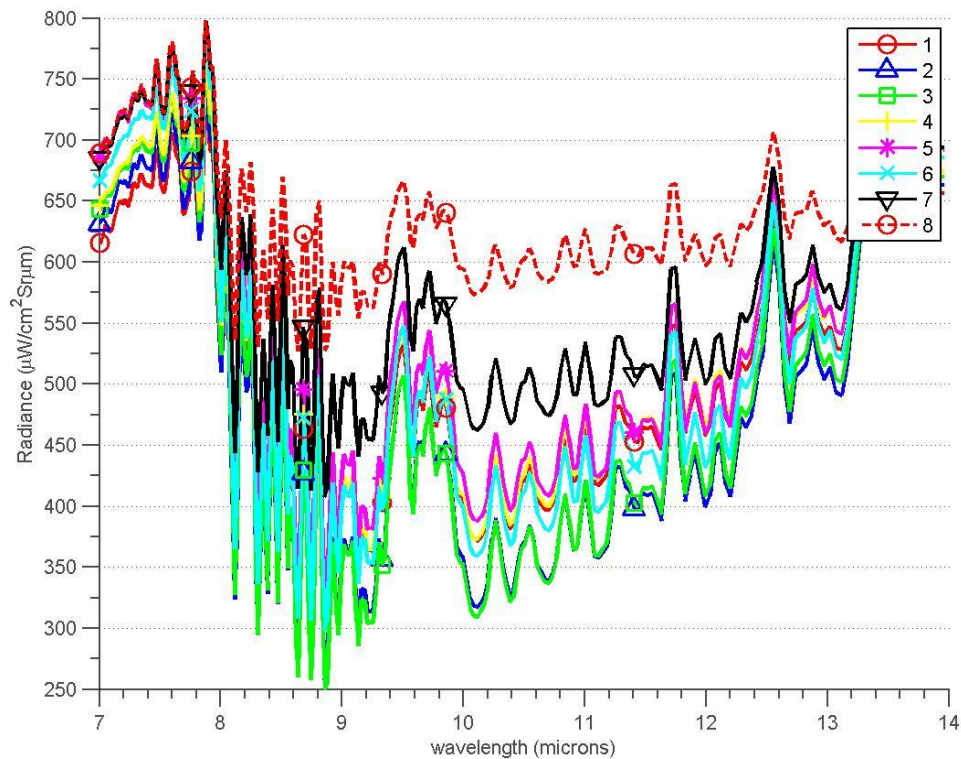


Figure 9. This plot shows the spectral reflected radiance of the flat Infragold® panel as measured during eight different times, which are ranked in order in the legend. The ambient temperatures during measurement time increased in one direction, though the measured reflected radiances do not rank in order of radiance from lowest to highest, suggesting that changing cloud cover significantly affected measurements over time.

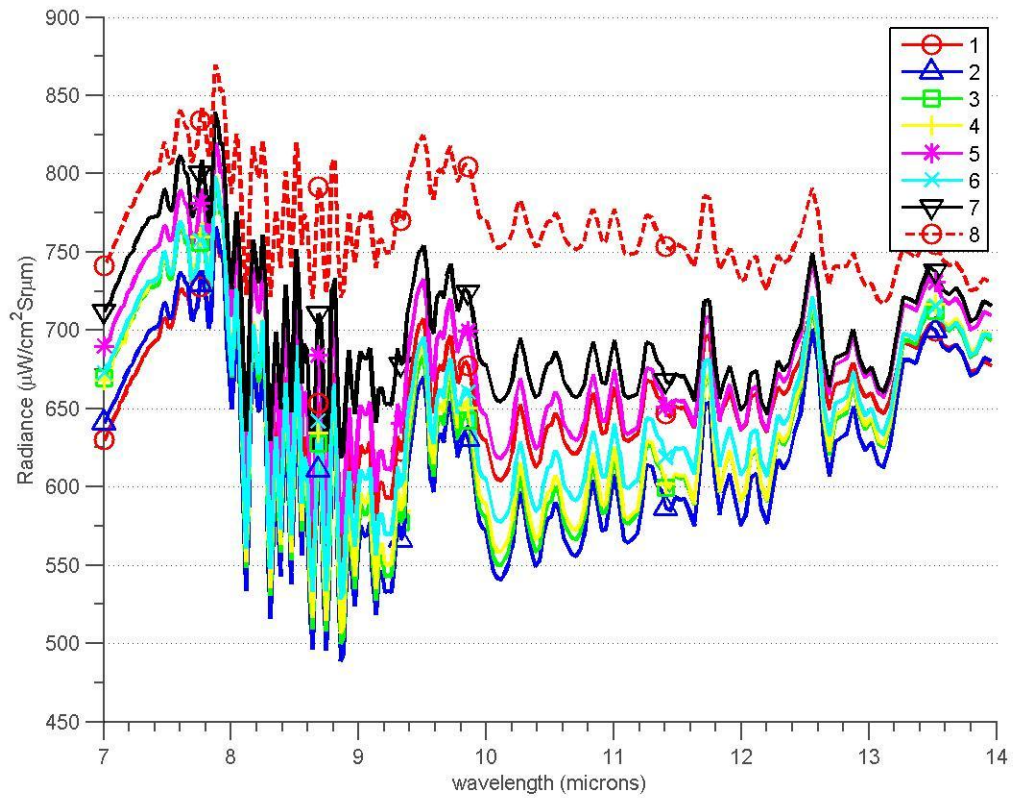


Figure 10. This plot shows the spectral reflected radiance of the 45° tipped Infragold® panel as measured during eight different times, which are ranked in order in the legend. The ambient temperatures during measurement time increased in one direction, though the measured reflected radiances do not rank in order of radiance from lowest to highest, suggesting that changing cloud cover significantly affected measurements over time.

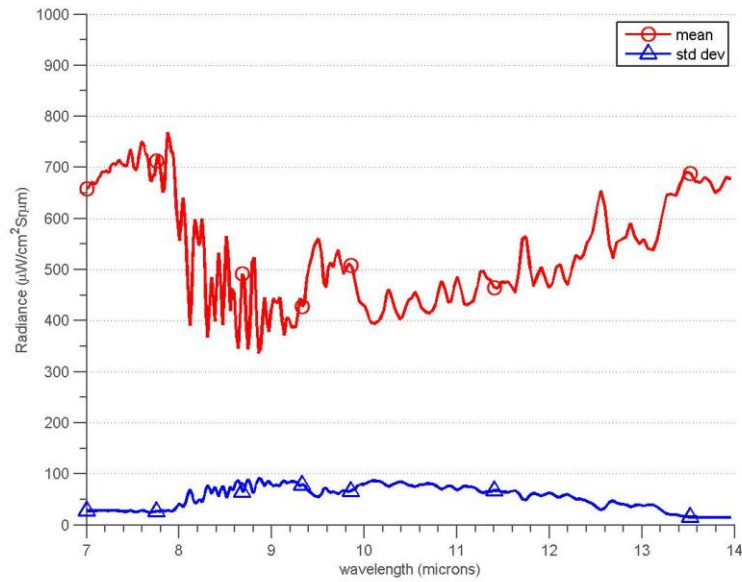


Figure 11. This plot shows the mean and standard deviation of the measured spectral reflected radiances from the flat Infragold® panel, as measured at eight different times. The measured radiance varies between approximately 20 and nearly 90 $\mu\text{W}/\text{cm}^2\text{Sr}\mu\text{m}$, likely owed to changing ambient temperatures and cloud cover as supported by Figures 9 and 10.

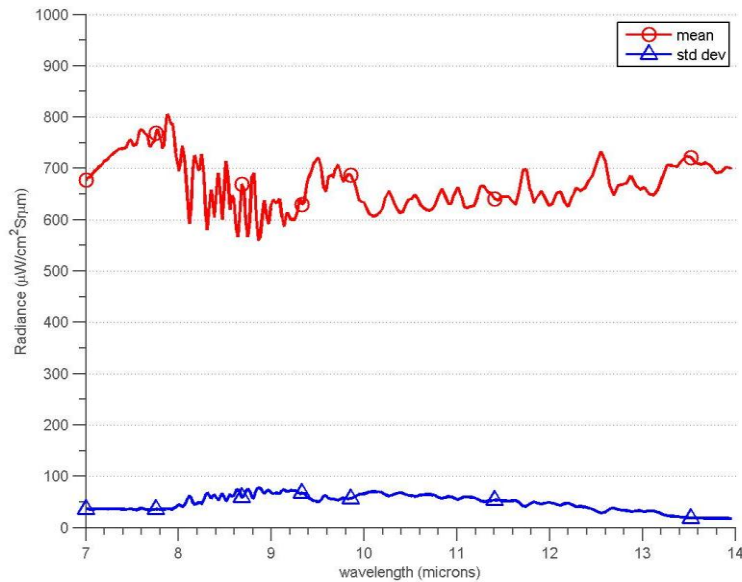


Figure 12. This plot shows the mean and standard deviation of the measured spectral reflected radiances from the 45° tipped Infragold® panel, as measured at eight different times. The measured radiance varies between approximately 20 and nearly 80 $\mu\text{W}/\text{cm}^2\text{Sr}\mu\text{m}$, likely owed to changing ambient temperatures and cloud cover as supported by Figures 9 and 10.

SOC-100 Reflectometer Data Collection

The collection of spectral HDR, SDR, and DDR data on samples of materials M2, M5, and M6 was performed using one measurement and 32 scans with the source blackbody at 700°C. Samples of materials M1, M3, M4, M7, and M8, however, were measured using one measurement and eight scans, with a source blackbody at 450°C, in order to avoid damage to the samples (reduced exposure time). This was also necessitated as fumes from heated samples may inadvertently coat the gold hemi-ellipsoidal mirror and the optics of the device and rendering the SOC-100 reflectometer less accurate. Additionally, the measurements were unpolarized, again in order to reduce the total exposure time of the sample to the source blackbody.

The collected data is in the range of 2-25 μm , even though only the range of 7-14 μm was utilized for research. The data was collected at angles of reflectance (with respect to the sample's normal) of 20°, 30°, 40°, 45°, 50°, 60°, and 70°. Figure 13 is shown as a sample of one of the panels, M8, when observed at 30°. The data suggests that the material is not very reflective as the highest peak is below 30% reflectance, but is very specular, as the SDR line closely follows the HDR line. Additionally, the DDR is generally low compared to the total HDR, as the DDR is always below 2% reflectance.

Due to the limitation in the SOC-100 reflectometer, no data was taken below 20° or above 70° in reflectance angle. In order to allow for any reflectance angle to be used, the data was interpolated to reflect an important statement made by Fresnel's equations (Hecht 1998), that at angles of incidence (correspondingly, reflectance angles here) which approach 90°, any material becomes increasingly reflective.

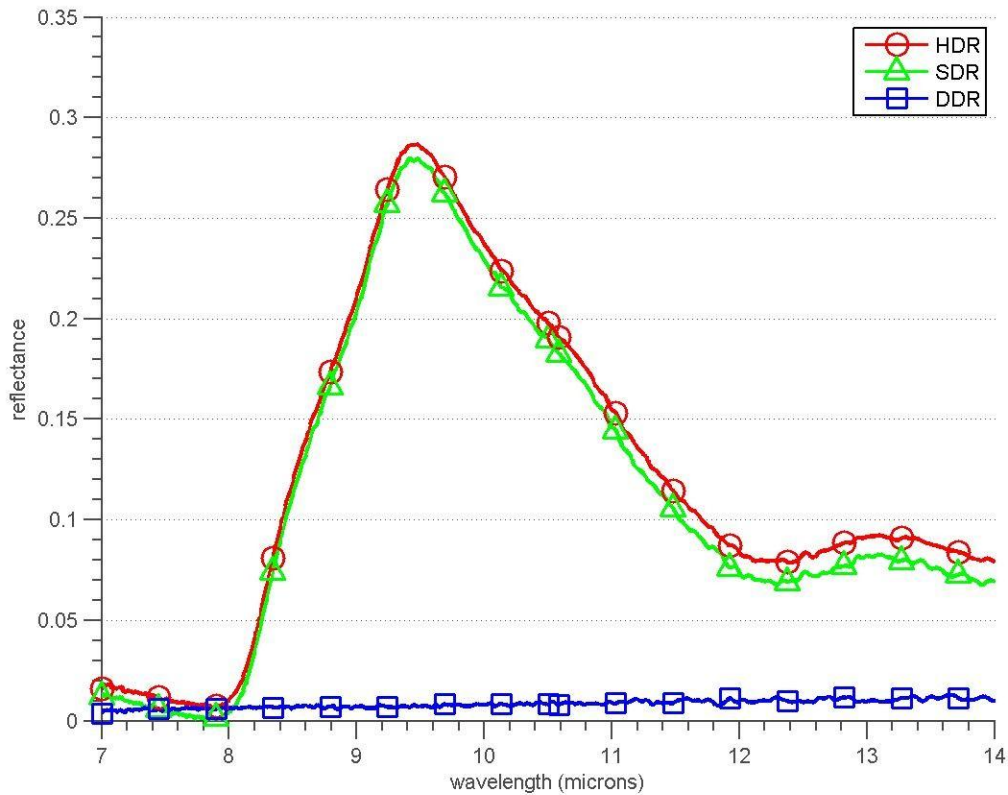


Figure 13. The HDR, SDR, and DDR of panel M8 (laminated safety glass) at 30° angle of incidence are presented. The sample has an overall low reflectance as it is less than 0.30. It is, however, very specular, which is evident by the SDR line closely following the HDR line. Conversely, the material is minimally diffuse. This plot is presented as an example. The rest of the reflectance plots may be found in Appendix A.

The collected SOC-100 reflectometer data was, during interpolation, also interpolated across the range of angles from zero to 90°. A sample of the interpolated data at one particular wavelength (10μm) is shown in Figure 14, where the HDR and SDR of the material approach one as the reflectance angle approaches 90°. As expected, the DDR simultaneously approaches zero. Plots of the rest of the panels are shown in the Appendix B.

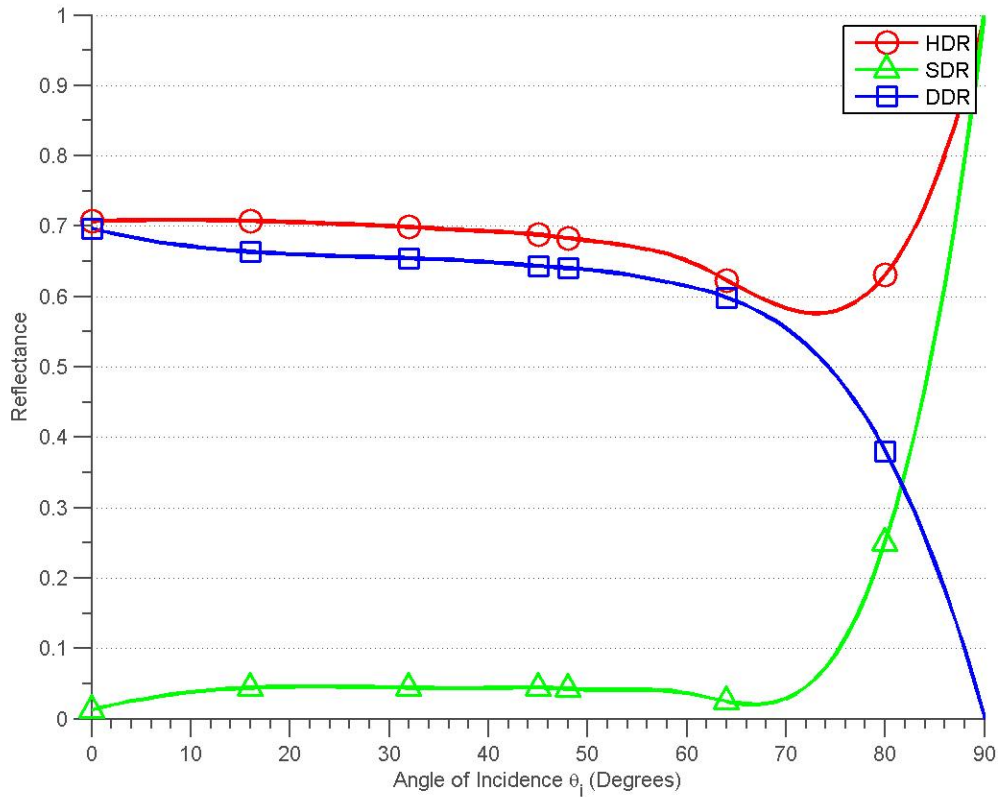


Figure 14. The HDR, SDR, and DDR of panel M1, flame-sprayed aluminum, are given at 10 microns, as a function of angle of incidence. This is data which was interpolated to reflect that all materials have a reflectance which approaches one as the angle of incidence approaches 90°. In this figure, the HDR and SDR are shown to reflect this rule, while the DDR decreases to zero as expected.

The panels were characterized depending on their properties as measured by the SOC-100 reflectometer in the categories of reflectance, specularity, diffuseness, and emissivity, as given by their average HDR, average SDR, average DDR, and average emissivity, ε , respectively, across the 7-14 μm . Additionally, the specularity of each material is given as the quotient of the HDR and SDR, where a higher number indicates a more specular material. The information is presented in Table 2.

Table 2. Mean HDR, SDR, DDR, and emissivity ε across the 7-14 μm wavelength range for the eight panels at the angle of incidence of tipped panels (30°).

Panel	HDR	SDR	DDR	Specularity (SDR/HDR)	$\varepsilon = (1 - \text{HDR})$
M1	0.66	0.042	0.62	0.064	0.34
M2	0.076	0.0022	0.073	0.029	0.92
M3	0.078	0.0014	0.078	0.018	0.92
M4	0.12	0.060	0.057	0.5	0.88
M5	0.95	0.84	0.11	0.88	0.052
M6	0.21	0.011	0.20	0.052	0.79
M7	0.060	0.052	0.0083	0.87	0.94
M8	0.14	0.13	0.0088	0.93	0.86

PLEXUS (using Modtran 4.0 V2R1)

PLEXUS was used to generate data to account for the atmospheric effects when modeling solar irradiance. The data was generated using parameters which match the field collection conditions as closely as possible.

Additionally, PLEXUS was used to generate sky spectral radiance data in order to compare to field-collected data, as shown in Figures 15-18. If the generated radiances are sufficiently close to the field-collected radiances, then PLEXUS may be used as a replacement, and more importantly could account for the sky radiances in reverse radiative transfer models, where measured sky radiance at a specific location is likely not known. The performance of these plots is discussed later, in Chapter V, though it is readily apparent that the PLEXUS radiances do not closely match the mean field downwelling measured radiances.

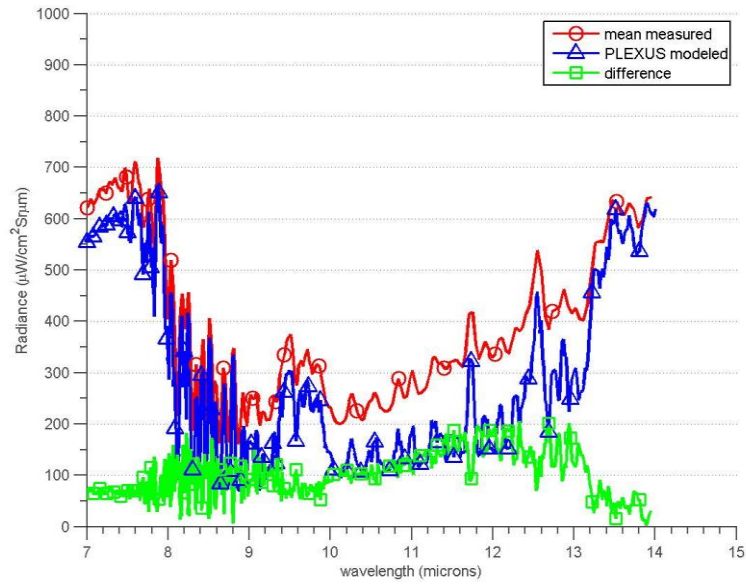


Figure 15. The sky down-welling radiance at zenith is shown for the mean field-collected and PLEXUS-generated data. The general spectral features match, though the field data appears much more smoothed than the PLEXUS data, and the PLEXUS data has less radiance across the spectrum, likely because cloud cover data was not rigorously modeled.

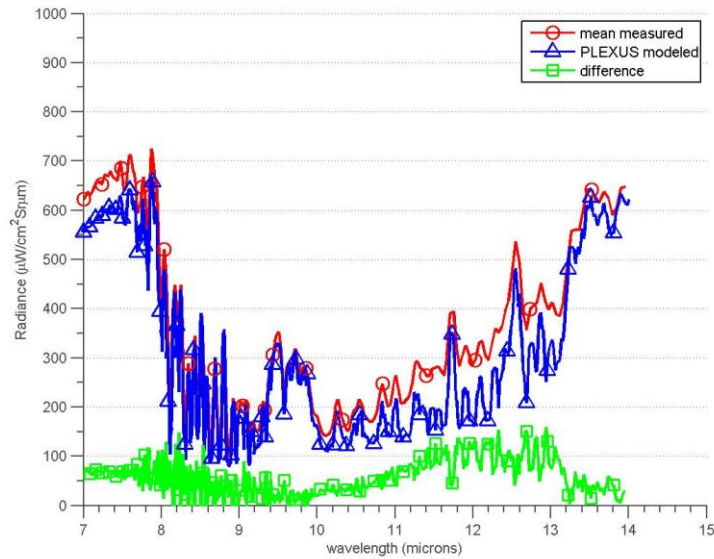


Figure 16. The sky down-welling radiance at 30° from zenith is shown for the mean field-collected and PLEXUS-generated data. The general spectral features match, though the field data appears much more smoothed than the PLEXUS data, and the PLEXUS data has less radiance across the spectrum, likely because cloud cover data was not rigorously modeled.

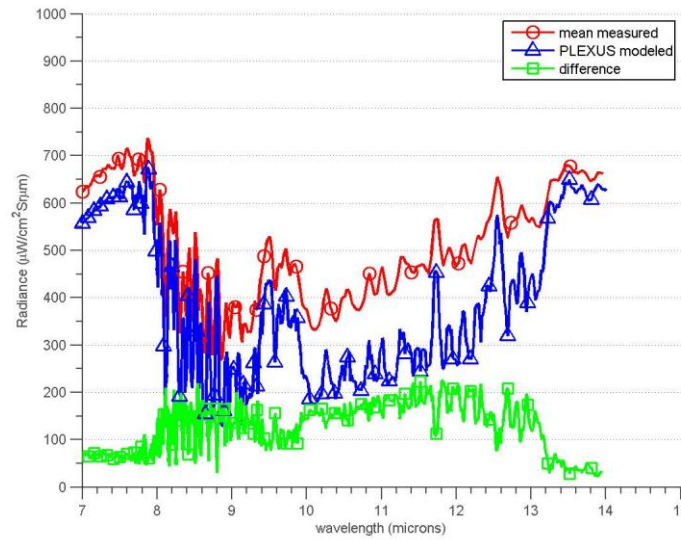


Figure 17. The sky down-welling radiance at 60° from zenith is shown for the mean field-collected and PLEXUS-generated data. The general spectral features match, though the field data appears much more smoothed than the PLEXUS data, and the PLEXUS data has less radiance across the spectrum, likely because cloud cover data was not rigorously modeled.

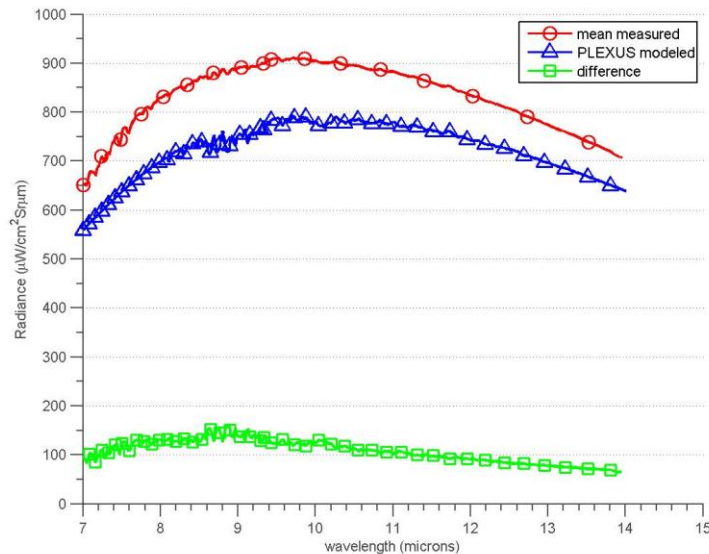


Figure 18. The sky down-welling radiance at 90° from zenith is shown for the mean field-collected and PLEXUS-generated data. The general spectral features match, though the field data appears much more smoothed than the PLEXUS data, and the PLEXUS data has less radiance across the spectrum, likely because cloud cover data was not rigorously modeled.

Importing and Re-sampling Data

Data to be used for the radiative transfer model could have any number of differences which would make it unusable without specific transformations. Such differences include primarily the units of the data, the range of the data, the number of data points in the given range, and the linearity of data, where the spacing between two data points may or may not be constant. The code written for this research was designed such that it may import any sort of data as long as it has the appropriate units. The range, number of data points, and relative spacing between each data point are automatically accounted for by using a spline interpolation function. This interpolation function forces all imported data to fit to a particular range in wavelength, with a particular number of data points, where the spacing between all data points is made constant. This is important as any physical simulation which uses an array of discrete values for its simulation must have those values matching in range and spacing.

Furthermore, the research requires the continued re-modeling of all available data in order to find the most accurate method which represents collected data. For this, the code's design is powerful in allowing an experimenter to use different sources of data at will. This, of course, includes all field data, SOC-100 reflectometer data, and PLEXUS-generated data used for this paper.

Radiative Transfer Model

The radiative transfer model described in Chapter III was used in both the diffuse-only and the diffuse-specular forms. The sky down-welling radiance, the ground radiance, and the reflectance data (HDR, SDR, and DDR) were obtained from the field-

collected and lab-collected data, while the solar radiance, atmospheric transmittance, and panel self-emission were modeled. None of the PLEXUS data was used in the radiative transfer models as it did not match the measured down-welling radiance data upon visual inspection.

Reverse Radiative Transfer Model

The reverse radiative transfer model was used for only the diffuse-only case, due to the difficulty, in the time permitted, of fitting a reflected radiance in two variables, the HDR and SDR, as opposed to fitting it to only the HDR (which is a direct calculation).

Model Angular Parameters

Each model was performed using estimated observation elevation and azimuth angles, where these angles were assumed to be the same during the collection of data from panel to panel. The estimated angles of 40° from zenith and 45° in azimuth necessitated a specular observation angle, θ_{spec} of 63° from zenith as calculated using equation (36). This specular angle corresponds to 27° above the horizon. It is important to note that the angles may vary some since the measuring FTIR was positioned from one panel to the next, but it is assumed that the variation would not cause a significant change in the observed spectral reflected radiances.

Summary

The collection of field and lab data was introduced, providing many specific details of the collection, and showing the mean and standard deviation of down-welling radiances at different angles across all panels. It is shown that the deviation at 0° and 60° from zenith is significantly higher than at 30° and 90° , raising questions about the

variation of the down-welling radiance. This was also evident in the measurement of Infragold® time-ordered reflected radiance, and standard deviation. Furthermore, reflectance of aged Infragold® was shown, and the use of specific HDR and SDR was justified.

The HDR, SDR, and DDR, specularity, and emissivity data of each individual panel were presented. Additionally, the use of PLEXUS was explained as a tool for generating atmospheric transmittance and down-welling radiance at different angles. Lastly, the importance of resampling data was explained, and an overview of the use of the radiative transfer model and the reverse radiative transfer model was given, along with a short discussion on parameters used in the models.

V. Analysis and Results

Chapter Overview

This chapter introduces all data collected using the methodology given in Chapter IV. Subsequently, an analysis and results are presented, allowing for appropriate conclusions to be made regarding the accuracy of the diffuse-only and diffuse-specular radiative transfer models, and the feasibility of a reverse radiative transfer model for material identification.

First, a fundamental method used in the code base, spline interpolation, and how accurate it is to any (expected) degree of interpolation is established. This is followed by a short, related analysis of how different the hemispherical integration is when it is performed with few (four) and many (91) samples of data, in order to give credence to the use of only four points of field down-welling radiance data (0° , 30° , 60° , and 90° from zenith). Then, the importance of the solar irradiance in the radiative transfer models is gauged as a whole. Subsequently, the results and the analysis of the performance of both the diffuse-only and diffuse-specular radiative transfer models are presented, followed by an analysis on a reverse, diffuse-only radiative transfer model.

Accuracy of Spline Interpolation in Resampling of Data

The code written for this paper heavily relies on cubic spline interpolation in order to resample all available data to the same, chosen base range of wavelengths and angles (if applicable). Therefore, it is of interest that the cubic spline interpolation can accurately fill in missing values for those data sets which are smaller than the chosen data set, and that it can down-sample data which has a lot more data points per wavelength

range. It is understood, however, that spectral features will be eliminated in down-sampling, and will not be recovered during up-sampling, due to the nature of interpolation.

It would be ideal to obtain some empirical metric that shows the difference between original and interpolated data. This is especially challenging to do because the mathematical comparison could only be made if the same number of values existed in both sample sets. Inherently, however, the interpolated sample set has more or fewer data points, and so the easiest practical way of comparing the two data sets becomes to simply plot them on the same axes.

As is shown in Figure 19, the difference between the imported data and its interpolated equivalent cannot be seen, as the two curves overlap completely. This would not be the case, however, if the original set of data was down-sampled by a sufficient amount. For this reason, all calculations made subsequently up-sample data to match the sample set with the highest resolution. In other words, a one-dimensional grid of points is used to represent, for example, both spectral reflectance and measured spectral radiances. This grid is always refined to match the number of points equal to the number of points of the highest resolution data that is used. Naturally, the interpolated data will therefore always match the original data, but will not become more accurate, as presented by the example Figure 19.

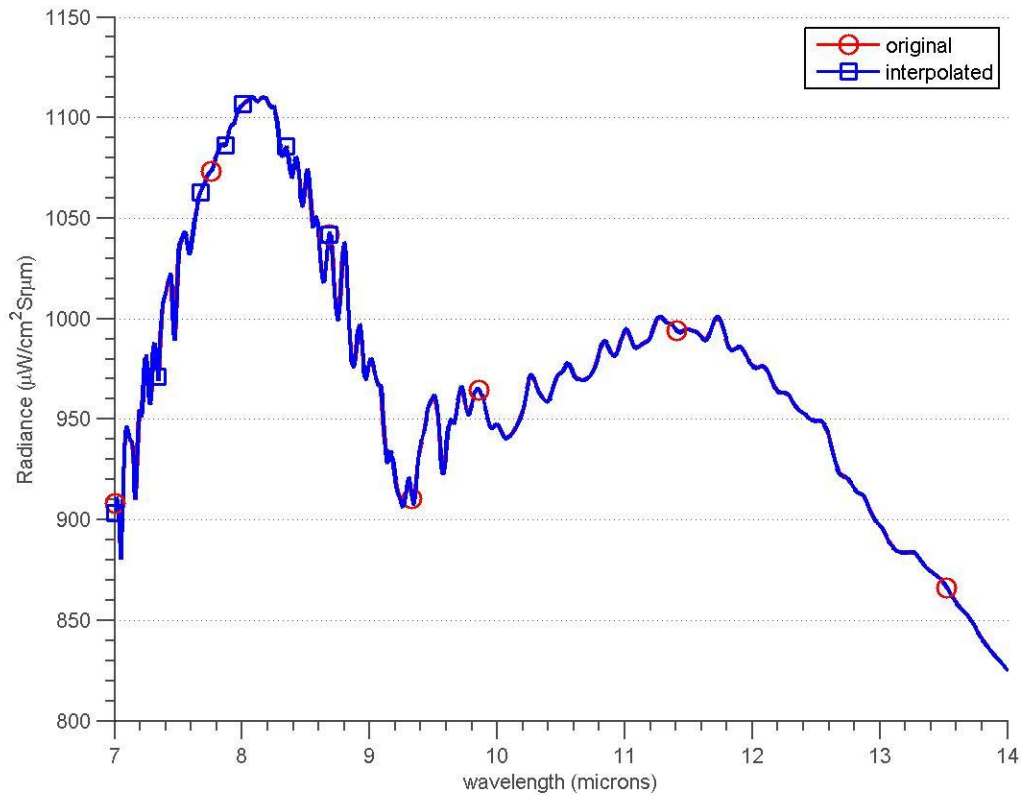


Figure 19. This plot shows panel M16 (tipped auto-glass) as an example, and shows that there is no difference in interpolated data when compared to original data. The two curves overlap completely. This means that the prolific use of interpolation within the code base will not cause any errors in the radiative transfer model, as all of the spectral features are preserved as long as the data is not down-sampled.

Hemispherical Irradiance at Panel

A potential source of error that was investigated was the amount of error present when integrating all radiance from the visible hemisphere, where only a few data points are available to represent the hemispherical data (as opposed to a comprehensive set of data covering many viewing angles). As a check, the amount of error was gauged with the help of PLEXUS, though the generated data was not used for any of the subsequent research. PLEXUS radiance data was generated from 0° to 90° with respect to zenith,

with a step size of 1° , yielding 91 sets of data. This large set of data was used to generate E_{hemi} as given in equation (41), and was compared to an equivalently-generated hemispherical irradiance using only four sets of the 91 sets of data, which were chosen at angles 0° , 30° , 60° , and 90° from zenith.

As shown in Figure 20, the relative difference between the two sets of data is very low, ranging from below 0.3% to above -0.5%, with a root-mean-square value of $0.178 \mu\text{W}/\text{cm}^2$ (when averaged over the wavelength range). It is important to note, however, that larger deviations between the data may exist if, for example, the 30° viewing angle included cloud cover, while the rest did not. This would increase the error for a low-sampled set of data as compared to a more comprehensive set of data.

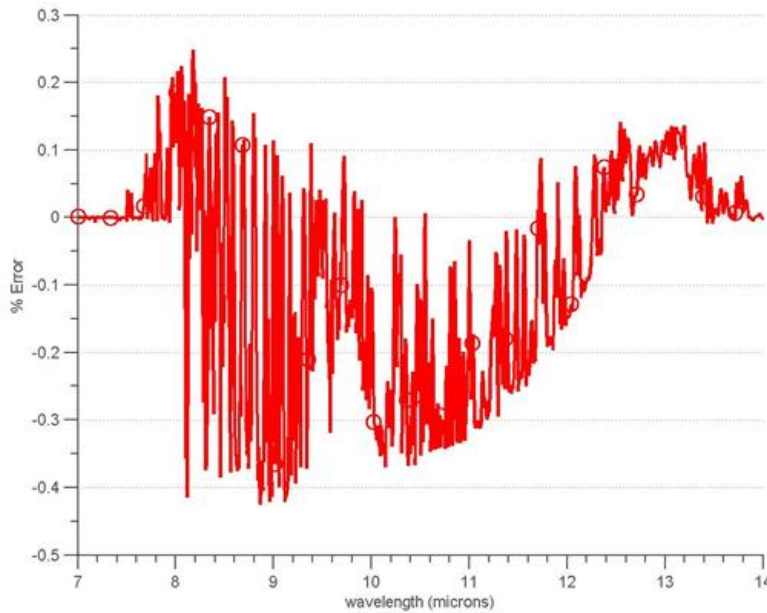


Figure 20. The percent error of PLEXUS sky irradiance data as compared between the hemispherical integration of four samples versus 91 samples is shown. There indeed is a difference, but it is very small and loosely bound between -0.5% and 0.3%. The RMS of the two data sets used, across the shown spectrum, is $0.178 \mu\text{W}/\text{cm}^2$, which is a negligible amount.

Solar Contribution

It is commonly understood that solar radiation is very relevant in the visible and near-infrared spectra when compared to terrestrial emissions. In the mid-infrared spectrum, solar radiation is very comparable to terrestrial emissions, while in the long-wave infrared range, solar radiation largely dwarfs in comparison to the thermal emissions of objects, terrain, and the atmosphere at standard (atmospheric) temperatures (Eismann, 2012:Ch 5, 22-29).

The solar contribution to the radiative transfer model was modeled and included in order to confirm that it will have a small effect on the total reflected radiance from a given panel. Furthermore, it would make the model more accurate especially in the specific case where the solar radiation is incident onto a panel in the specular direction of the observation angle. An example of the solar contribution for the non-specular case is shown in Figure 21, where the modeled incident solar irradiance is significantly smaller when compared to the modeled sky irradiance.

The comparatively small amount of solar irradiance available means that it has a very small effect on a panel's reflected radiance, in both the diffuse and the specular cases (unless the Sun is in the specular direction of the observer). As stated in Chapter IV, the field measurements were never made with the sun in the specular direction.

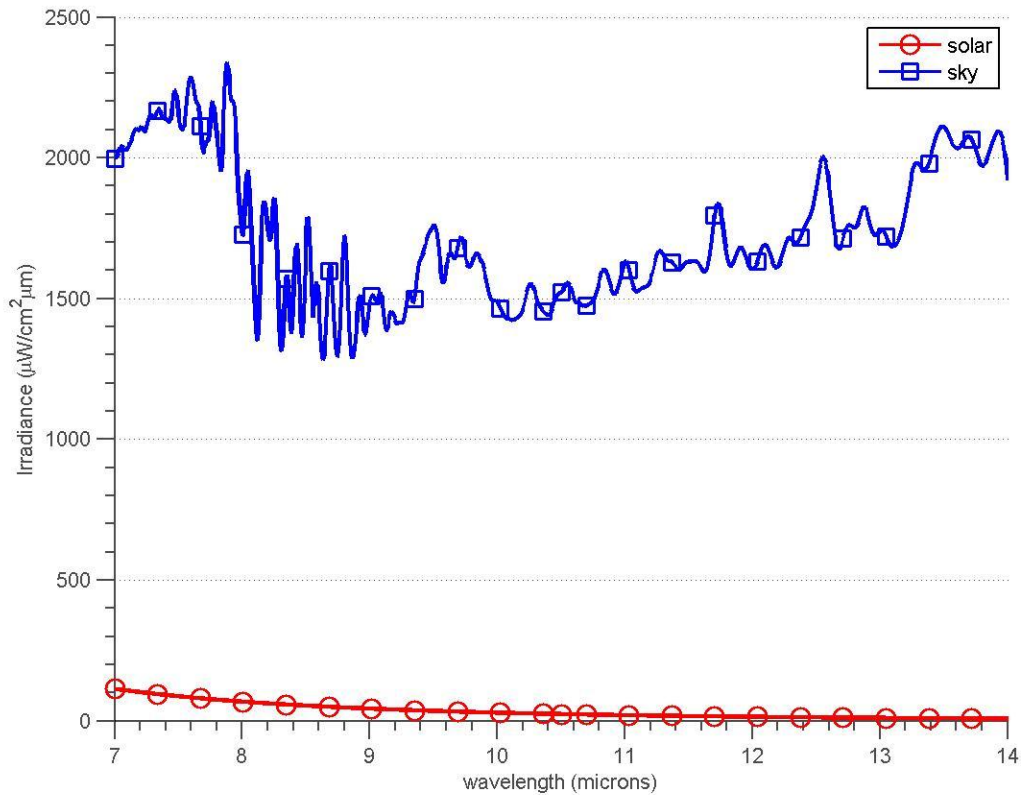


Figure 21. The solar and sky irradiance at panel M1 (flame-sprayed aluminum) are shown as an example, where the sun's position is outside of the specular viewing angle. The modeled solar irradiance is much smaller than the modeled sky irradiance, which is expected in the 7-14 μ m (long-wave infrared) wavelength range. This shows that the solar irradiance plays a very small part in properly modeling reflected radiance, except in the specular direction, where a high SDR may become a significant contribution in the case of a low DDR.

Infragold® Modeling

The Infragold® measurements were used in order to verify that the radiative transfer models work properly. Since no temperature measurements of the panels were made, the models were carried out assuming the temperature of the panel is 10°C above the ambient temperature at the time of measurement. This is realistic in that the resulting temperatures roughly match those of the mean thermocouple measurements of the other

most reflective material on the site – the radiant barrier, M5. This is furthermore acceptable as the temperature does not have a very dominating effect on the reflected radiance, since it controls the self-emission of the Infragold®, which is low due to the very low emissivity of Infragold®.

The best and worst cases are shown in Figures 22 and 23, where all other measurements produced results somewhere in between the two cases. The relative difference between measured and modeled data is presented in Tables 3 and 4 in order to give a complete picture of how closely the data match. The data is presented only for the diffuse-only model, as since the SDR of Infragold® is low, the diffuse-specular model did not produce significantly different results.

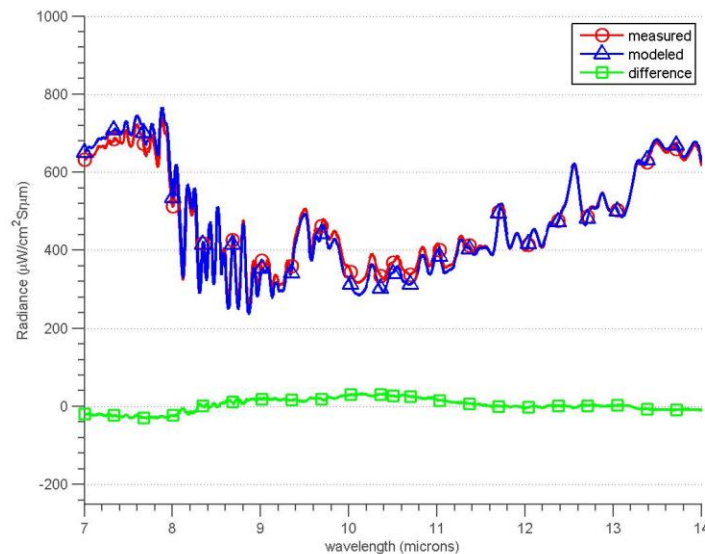


Figure 22. The measured and modeled spectral reflected radiances are given for the best matching case in modeling the measured reflected radiance from Infragold®. The difference between the two is notably low, where the relative difference metric of the two is shown in Table 3, at time 1632 GMT.

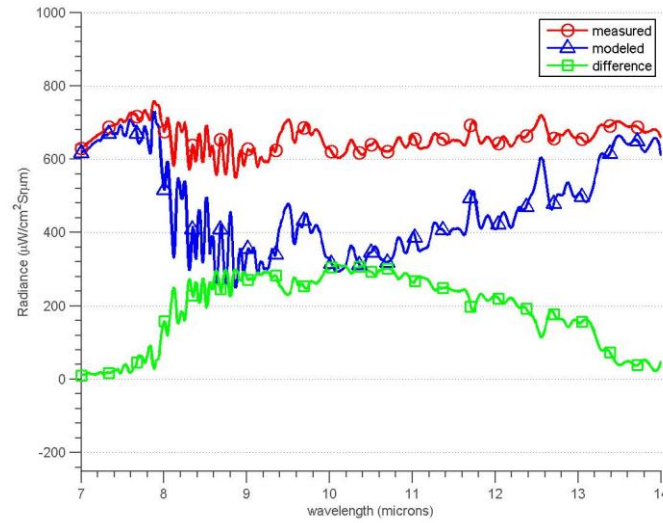


Figure 23. The measured and modeled spectral reflected radiances are given for the worst matching case in modeling the measured reflected radiance from Infragold®. The difference between the two is notably high, where the relative difference metric of the two is shown in Table 3, at time 1615 GMT. The difference vaguely resembles a blackbody curve, and likely indicates that a cloud was present during the measurement of the panel, but not during the measurement of the down-welling radiance a few minutes prior.

Table 3. Relative difference between measured and diffuse-only modeled reflected radiance of Infragold®, across the 7-14μm band.

Measurement Time (GMT)	RMS Relative Difference (%)	Measurement Time (GMT)	RMS Relative Difference (%)
1615	33.60	1730	7.09
1617	25.52	1732	19.22
1630	17.81	1746	21.36
1632	4.12	1748	11.11
1650	12.14	1801	19.48
1652	15.74	1802	11.81
1705	22.37	1816	22.04
1706	15.72	1817	20.76

Table 4. SAM values between measured and diffuse-only modeled reflected radiance of Infragold®, across the 7-14 μ m band.

Measurement Time (GMT)	Spectral Angle (°)	Measurement Time (GMT)	Spectral Angle (°)
1615	12.56	1730	2.36
1617	8.97	1732	5.97
1630	7.02	1746	7.67
1632	1.98	1748	3.50
1650	3.51	1801	7.35
1652	4.67	1802	4.65
1705	7.60	1816	7.92
1706	5.27	1817	8.15

The presented relative differences and spectral angles are a result of the difference between measured reflected radiances and the corresponding measured down-welling radiances. Since the measurements were not made simultaneously, but taken over, on average, a 4-minute time period, it is plausible that the down-welling radiance would be affected by changing cloud cover. Additionally, changes in the position of the Infragold® would change the radiance delivered from other surroundings. Since no measurements were made on the radiance outbound from the surroundings, adjacency effects also remain a probable cause for variations in the difference between measured reflected radiance, and the modeled reflected radiance produced using the measured down-welling radiances.

In the next section, the measured and modeled reflected radiances from panels of different materials were compared by finding the differences in thermocouple temperatures of the panels, and the panel temperature required in order to achieve a best fit of measured versus modeled reflected radiances. This self-emission temperature optimization was not performed for the Infragold® modeling because, though the relative

differences in reflected radiance may not be so large (as given in Table 3), since the emissivity of Infragold® is so small (1-0.94), then the self-emission temperatures are optimized to unrealistic values in order to account for that relative difference in measured versus modeled reflected radiance. The optimization was performed but is not presented as optimized temperatures ranged approximately from -50°C to 150°C, and the relative differences between measured and modeled reflected radiance are sufficient in showing how much the measured down-welling radiance varied. This is because the primary contributor to the modeled reflected radiance is the measured down-welling radiance, and there should be minimal difference, from one position and time to another, between measured and modeled Infragold® reflected radiances. Since the same Infragold® was used for each experiment, and so long as the measured down-welling radiances accurately represented the actual radiance incident on the Infragold® at each measurement point and time, then the relative difference between measured and modeled reflected radiances would be consistent, which it is not, as shown in Table 3.

Measured vs. Optimized Panel Temperatures

Initial modeling of the reflected radiance at each panel, which used the mean thermocouple temperatures at that panel as the panel temperature, showed a significant difference, across all panels, when compared to the measured spectra. One such example is given in Figure 24, where panel M12 is presented as modeled using the measured thermocouple temperature for the panel's self-emission component. Though the spectral features appear to match, the two spectra are different in magnitude. An educated guess was made that a likely cause could be an inaccuracy in the temperatures used, thereby

producing an error in the self-emission of each panel. Therefore, the panel temperatures were allowed to ‘float’ such that an optimal temperature was found for each, where that temperature produced the least-possible RMS relative difference as given by equation (51). The measured and modeled reflected radiance subsequently matched very well, as depicted in Figure 32. The differences in measured and optimized temperatures were recorded and are presented later in this chapter.

The optimization by panel temperature was repeated for both the diffuse-only and the diffuse-specular models, as they are expected to produce different reflected radiances during optimization. Therefore, each would have different corresponding optimized temperatures. The determination of which model performs better than the other is therefore dependent on how close each of the models is able to match the measured thermocouple temperatures.

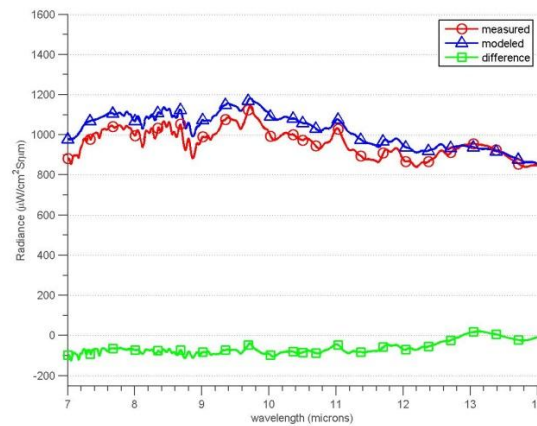


Figure 24. The measured and modeled reflected radiances at M12 (foamboard) are shown for the diffuse-only model, as an example. The spectral features seem to vaguely match up (calculated spectral angle of 1.76°), though the two spectra are off in magnitude, with a calculated relative difference of 7.19%. Optimizing the modeled spectra by varying the temperature forces the modeled spectra to match the measured spectra in magnitude, as shown in Figure 32.

Diffuse-Only Radiative Transfer Model

All panels were modeled through the diffuse-only radiative transfer model. The following figures show the measured and modeled (optimized) reflected radiances.

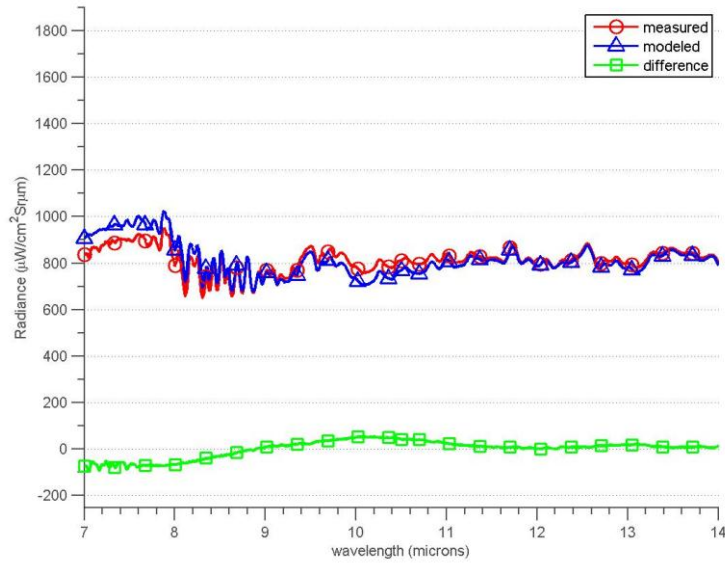


Figure 25. The measured and modeled reflected radiances at M1 (flame-sprayed aluminum) are shown for the diffuse-only model.

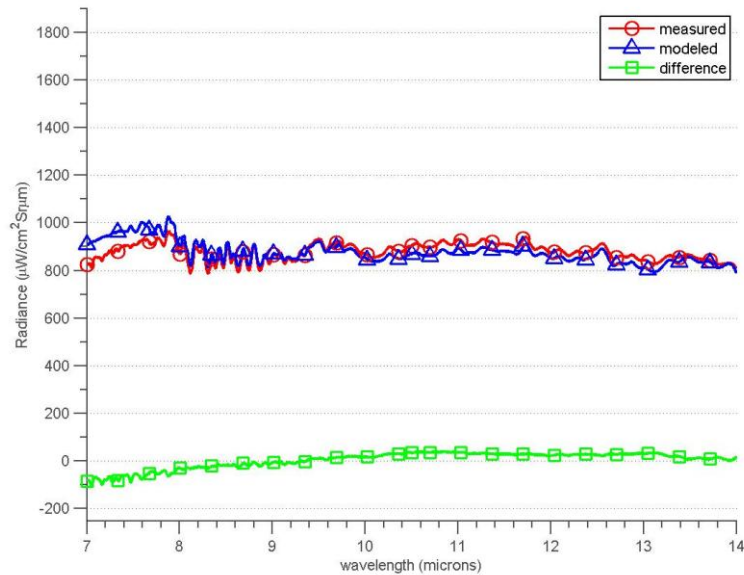


Figure 26. The measured and modeled reflected radiances at M9 (flame-sprayed aluminum) are shown for the diffuse-only model.

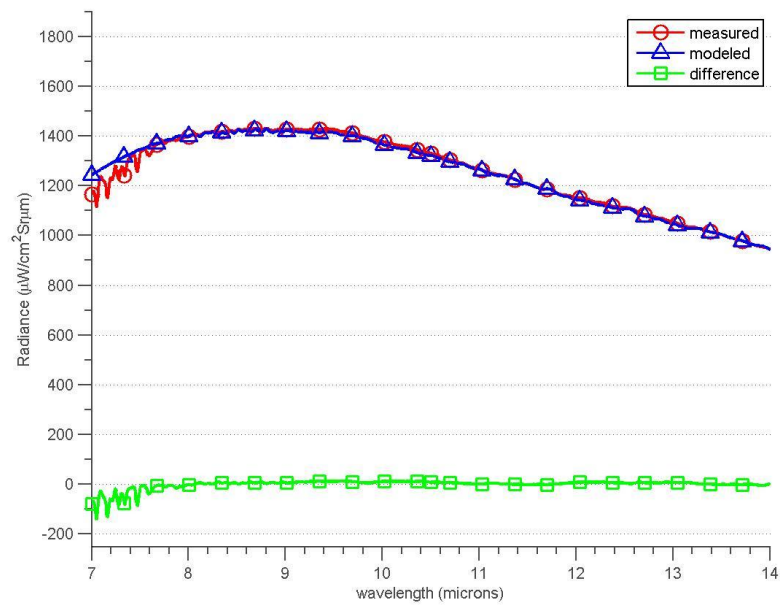


Figure 27. The measured and modeled reflected radiances at M2 (320-grit sandpaper) are shown for the diffuse-only model.

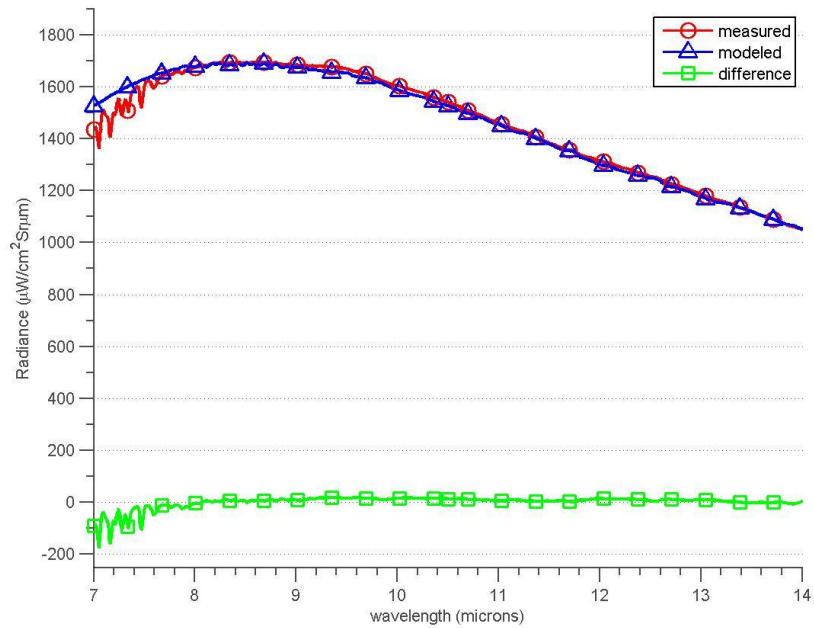


Figure 28. The measured and modeled reflected radiances at M10 (320-grit sandpaper) are shown for the diffuse-only model.

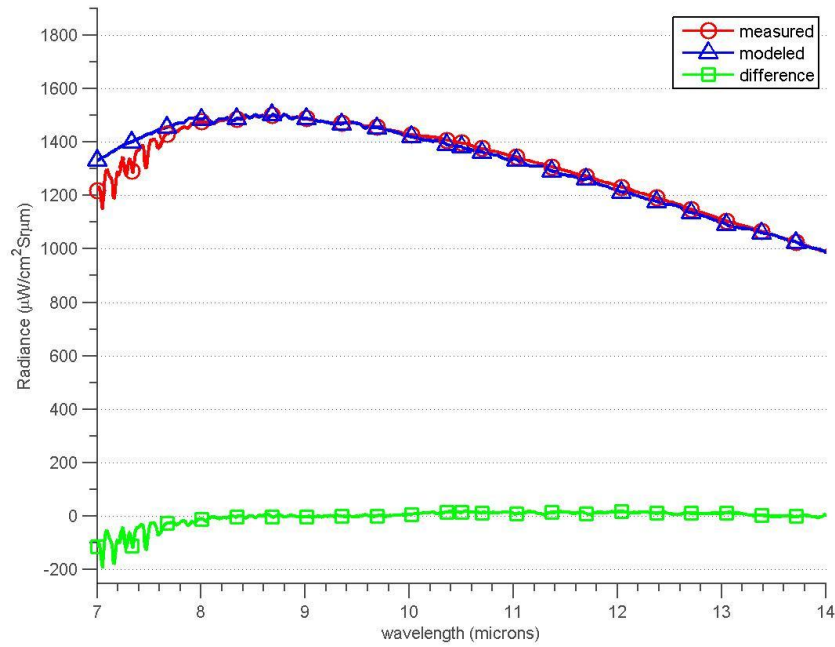


Figure 29. The measured and modeled reflected radiances at M3 (high emissivity, low reflectance material) are shown for the diffuse-only model.

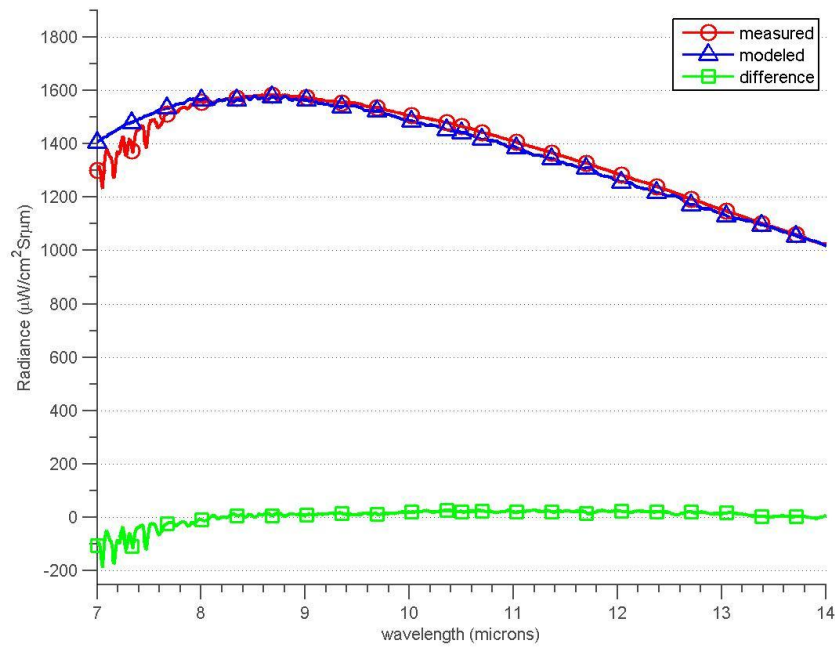


Figure 30. The measured and modeled reflected radiances at M11 (high emissivity, low reflectance material) are shown for the diffuse-only model.

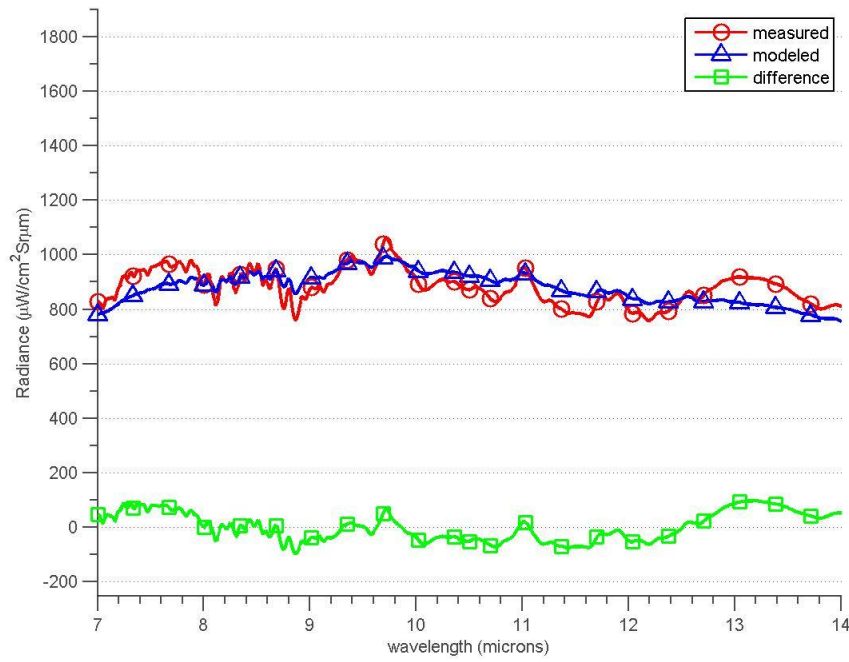


Figure 31. The measured and modeled reflected radiances at M4 (foamboard) are shown for the diffuse-only model.

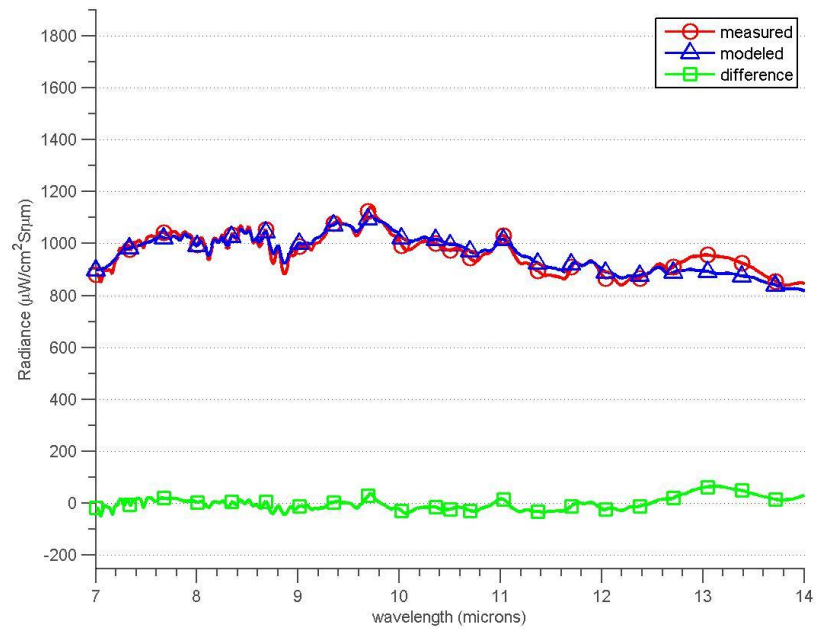


Figure 32. The measured and modeled reflected radiances at M12 (foamboard) are shown for the diffuse-only model.

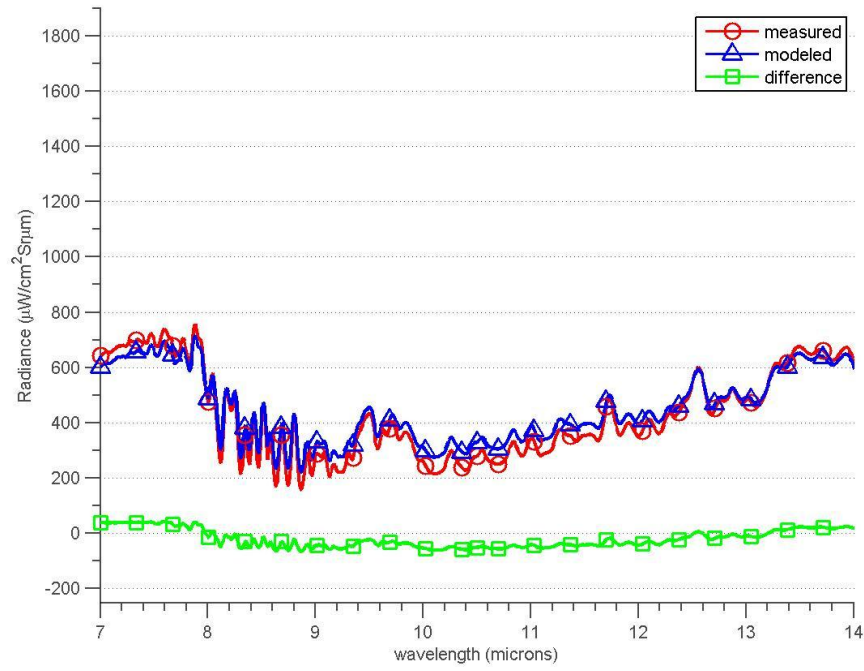


Figure 33. The measured and modeled reflected radiances at M5 (radiant barrier) are shown for the diffuse-only model.

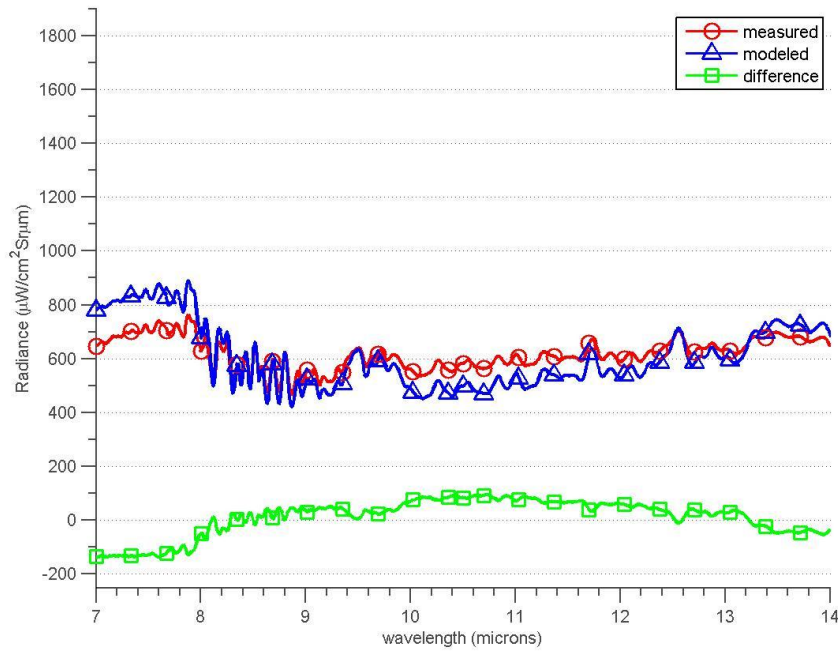


Figure 34. The measured and modeled reflected radiances at M13 (radiant barrier) are shown for the diffuse-only model.

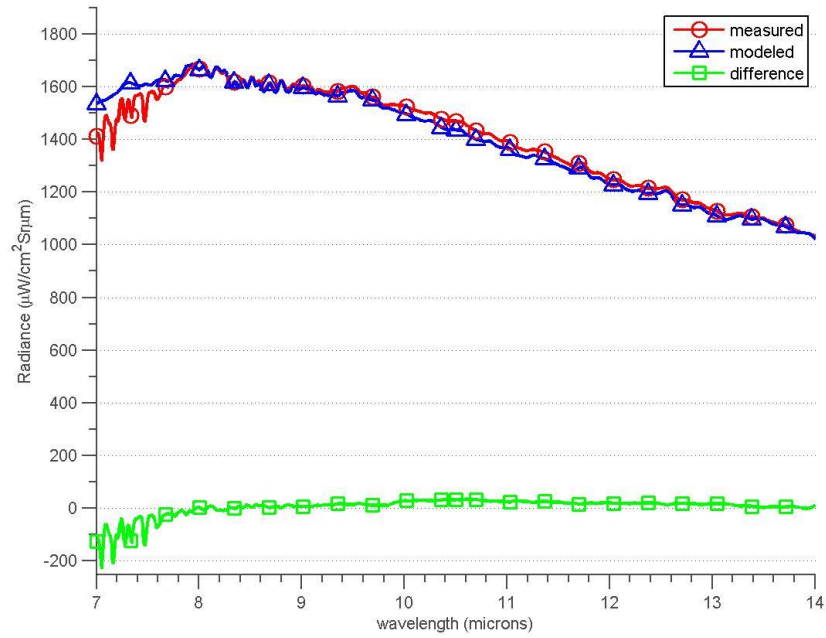


Figure 35. The measured and modeled reflected radiances at M6 (medium emissivity material) are shown for the diffuse-only model.

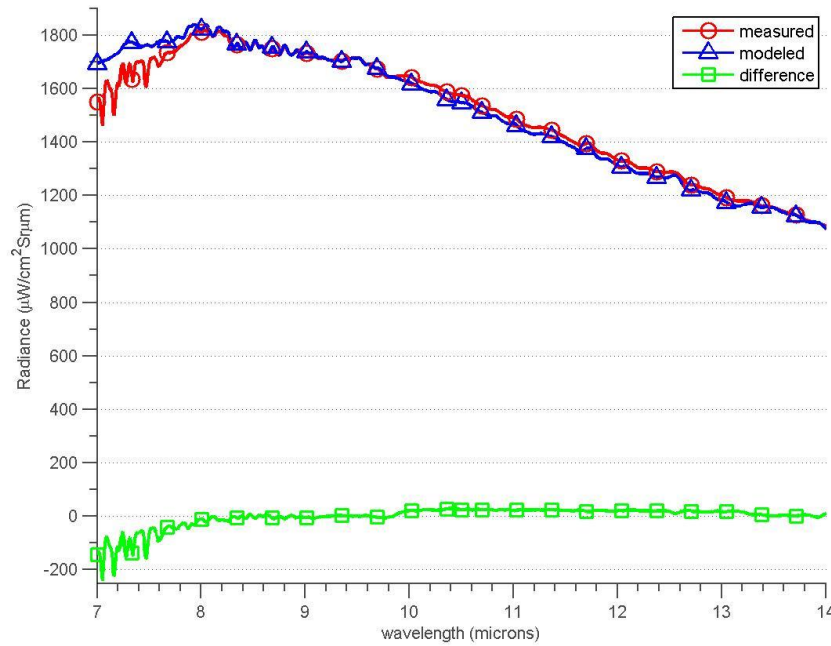


Figure 36. The measured and modeled reflected radiances at M14 (medium emissivity material) are shown for the diffuse-only model.

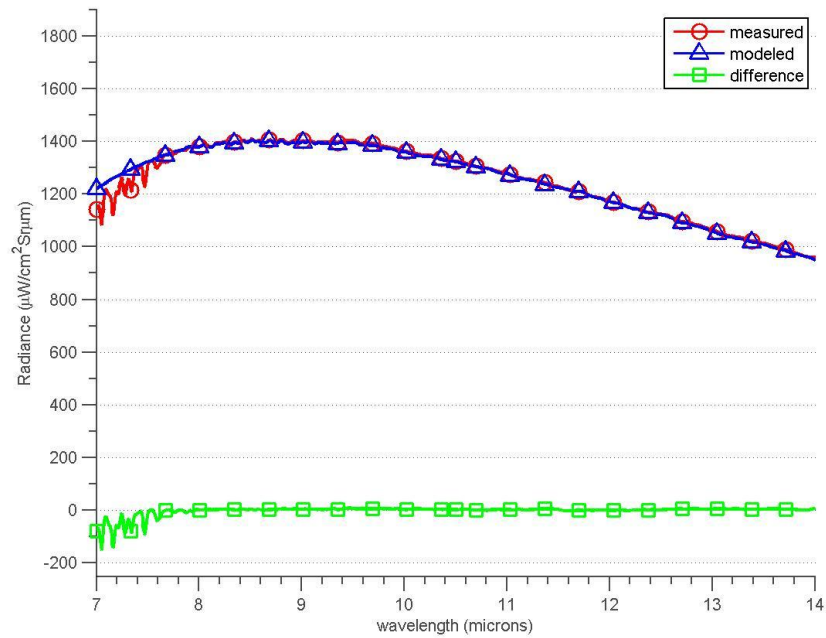


Figure 37. The measured and modeled reflected radiances at M7 (black vehicle paint) are shown for the diffuse-only model.

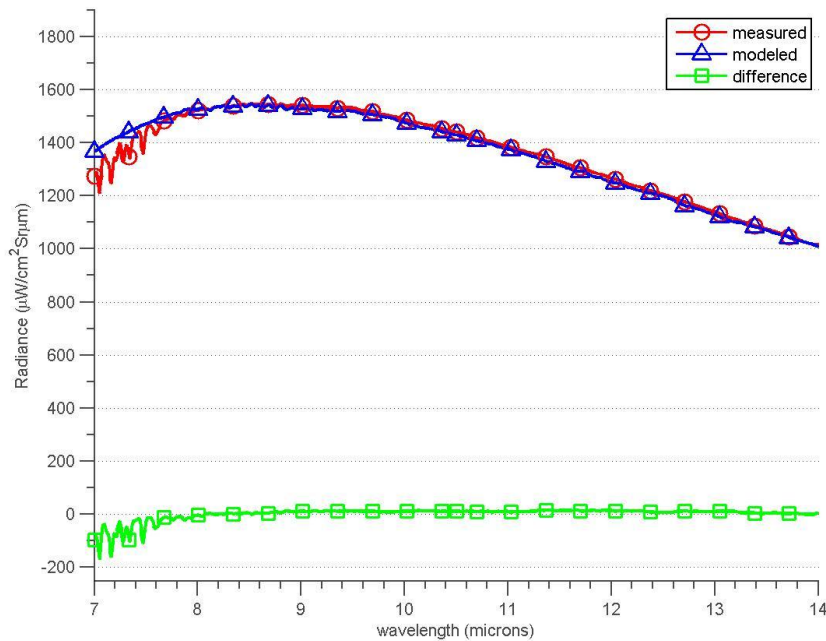


Figure 38. The measured and modeled reflected radiances at M15 (black vehicle paint) are shown for the diffuse-only model.

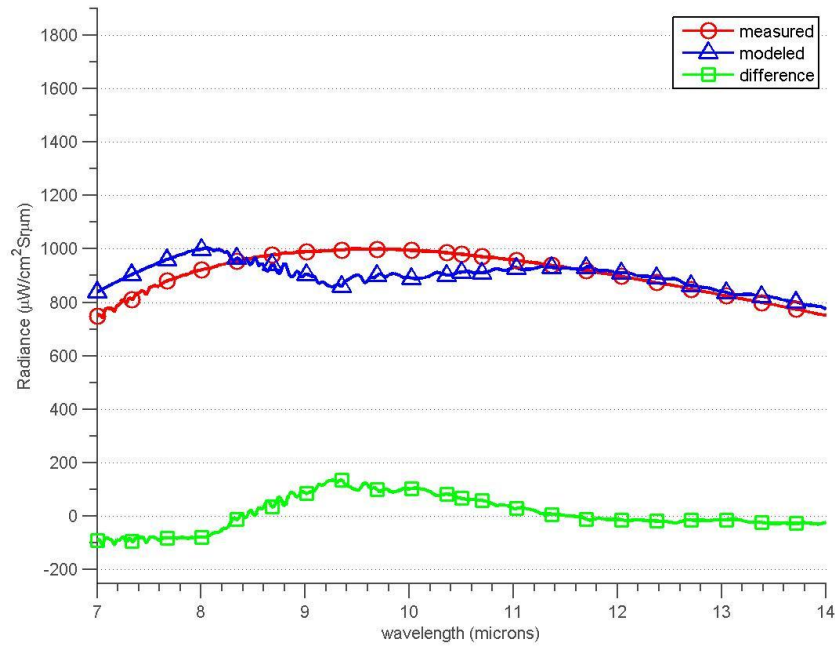


Figure 39. The measured and modeled reflected radiances at M8 (laminated safety glass) are shown for the diffuse-only model.

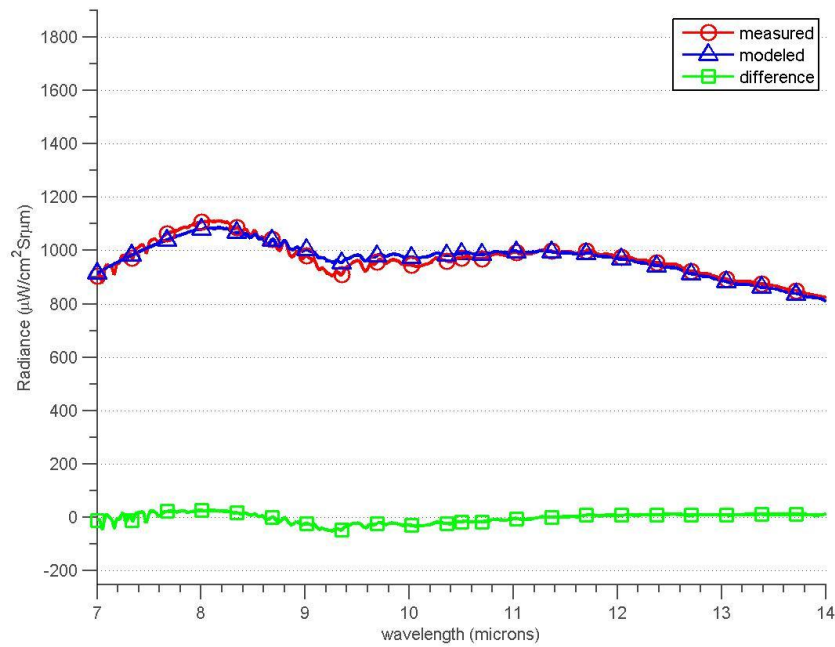


Figure 40. The measured and modeled reflected radiances at M16 (laminated safety glass) are shown for the diffuse-only model.

The mean and standard deviation of the thermocouple temperatures are shown in Table 5, along with the optimized temperatures, for each panel. Table 6 shows the relative difference between the measured and optimized temperatures that was subsequently acquired.

Table 5. Mean and standard deviation of thermocouple temperatures, and diffuse-only optimized panel temperatures.

Panel	Thermocouple Mean Temp (°C)	Thermocouple Standard Deviation (°C)	Optimized Temp (°C)
M1	56	0.260	64
M2	54	3.363	52
M3	53	0.364	56
M4	39	1.084	30
M5	29	0.539	-23
M6	67	0.594	69
M7	48	0.473	51
M8	35	0.217	32
M9	60	0.332	61
M10	66	2.772	63
M11	57	0.421	59
M12	43	0.677	38
M13	35	0.849	107
M14	73	0.823	75
M15	52	0.976	57
M16	39	0.342	36

Table 6. Relative difference between measured and optimal panel temperatures using the diffuse-only model.

Panel $\theta_{tip}=0^\circ$	Relative Difference (%)	Panel $\theta_{tip}=45^\circ$	Relative Difference (%)
M1	2.52	M9	0.22
M2	0.70	M10	0.80
M3	0.96	M11	0.64
M4	3.11	M12	1.49
M5	20.68	M13	19.04
M6	0.72	M14	0.59
M7	0.92	M15	1.39
M8	1.09	M16	0.91

For a more complete picture, Table 7 shows the corresponding relative differences between the measured and optimized, modeled spectra, and Table 8 shows the respective spectral angles for each panel.

Table 7. Relative difference between measured and modeled diffuse-only reflected radiance data, across the 7-14 μ m band..

Panel $\theta_{tip}=0^\circ$	RMS Relative Difference (%)	Panel $\theta_{tip}=45^\circ$	RMS Relative Difference (%)
M1	4.46	M9	3.87
M2	1.61	M10	1.70
M3	2.34	M11	2.32
M4	5.97	M12	2.68
M5	13.05	M13	10.78
M6	2.52	M14	2.53
M7	1.64	M15	1.90
M8	6.83	M16	1.93

Table 8. SAM values between measured and modeled diffuse-only reflected radiance data.

Panel $\theta_{tip}=0^\circ$	Spectral Angle ($^\circ$)	Panel $\theta_{tip}=45^\circ$	Spectral Angle ($^\circ$)
M1	2.60	M9	2.22
M2	0.88	M10	0.97
M3	1.27	M11	1.27
M4	3.38	M12	1.49
M5	4.52	M13	6.30
M6	1.44	M14	1.48
M7	0.87	M15	1.04
M8	3.96	M16	1.09

It is evident from Table 6 that most of the optimal panel temperatures were less than approximately 3% different than the measured thermocouple temperatures for all panels, except M5 and M13. This means that there is very adequate agreement between what the diffuse-only model simulated, and what the thermocouples recorded, when

comparing the panel temperatures. The corresponding RMS relative difference in reflected radiance for each panel is less than approximately 7% for all panels, except, again, M5 and M13. This means that the measured and modeled spectra for the panels agree closely in magnitude. The last evidence to support the diffuse-only model is Table 5, showing that the spectral angle between the measured and modeled spectral reflected radiance is also very low, less than approximately 4% for all panels except M5 and M13. It is important to note that an angle of 0° would be an ideal match, while an angle of 90° would be a complete mismatch. Panels M5 and M13 are both radiant barrier materials, and have the highest reflectance and specularity of all panels, as shown in Table 2. Looking at Figure 33 and 34, it is evident that the spectra still match fairly well. The optimized temperature for M5 of -23°C and M13 of 107°C are extreme and certainly incorrect. The reason they are so extreme is because the model represents the emissivity of materials as 1 minus the HDR reflectance, and since the radiant barrier is so reflective, its self-emission has a negligible contribution to the modeled reflected radiance, requiring extreme changes in temperature in order to either raise or lower so that it matches the measured reflected radiance. This further supports the idea that, though the error is presented as an error in the temperatures, this is really a result of the difference between the down-welling radiance from when the sky measurements were taken, and when the panel's reflected radiance was measured. The rest of the panels have optimized temperatures that much more closely match the measured thermocouple mean temperatures because the rest of the materials have fairly low reflectance, allowing the self-emission to more easily account for differences between measured reflected radiances, and modeled reflected radiances that were not yet optimized.

Diffuse-Specular Radiative Transfer Model

All panels were also modeled through the diffuse-specular radiative transfer model. The following figures show the measured and modeled reflected radiances.

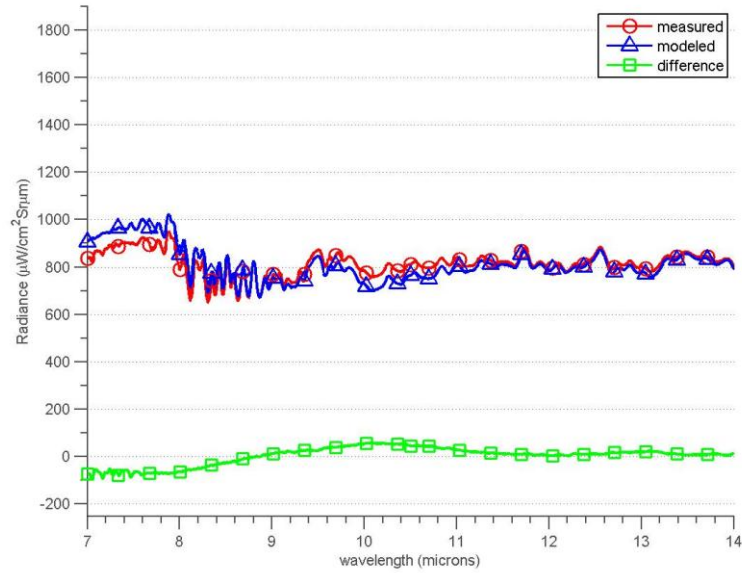


Figure 41. The measured and modeled reflected radiances at M1 (flame-sprayed aluminum) are shown for the diffuse-specular model.

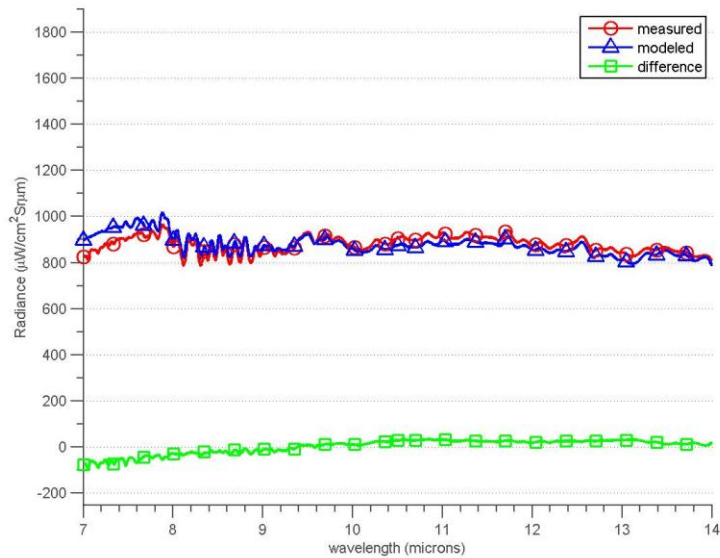


Figure 42. The measured and modeled reflected radiances at M9 (flame-sprayed aluminum) are shown for the diffuse-specular model.

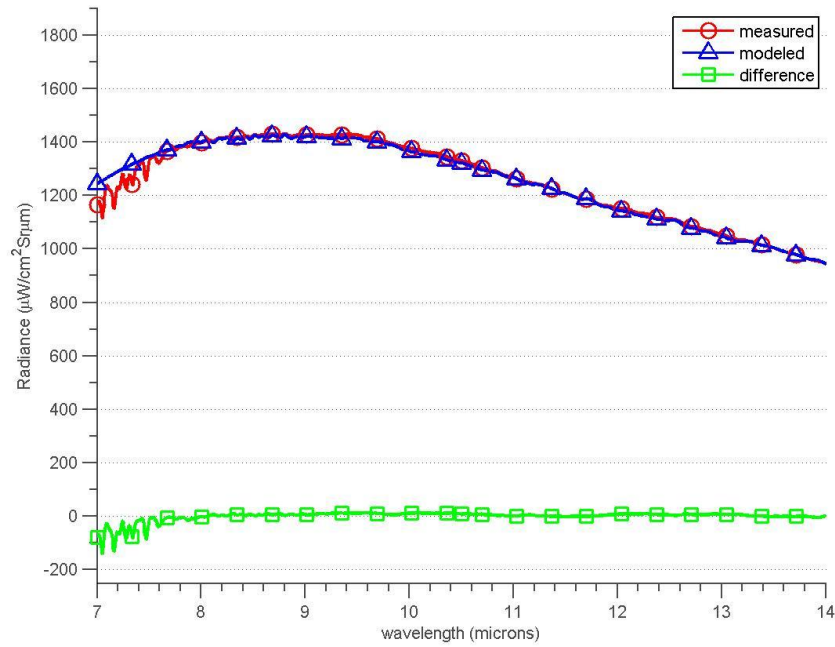


Figure 43. The measured and modeled reflected radiances at M2 (320-grit sandpaper) are shown for the diffuse-specular model.

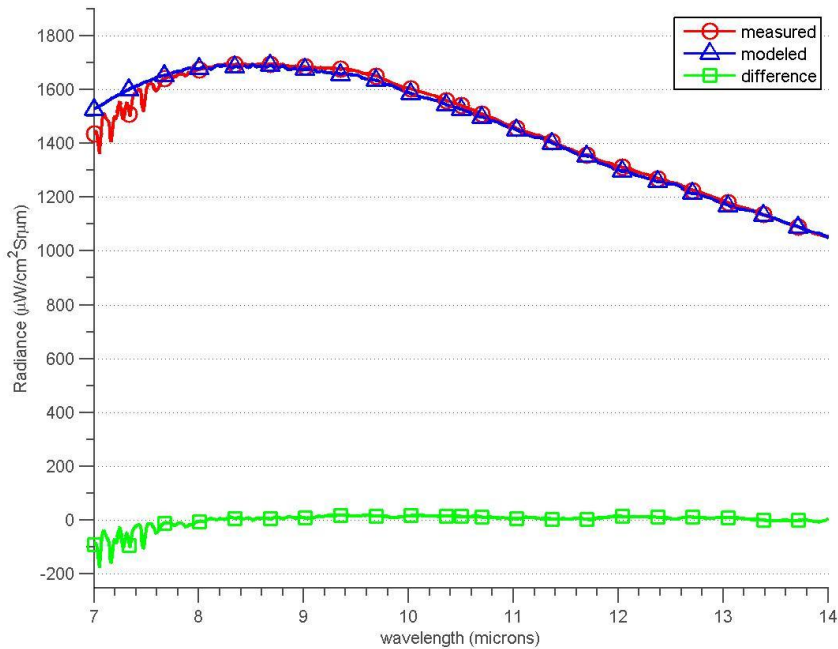


Figure 44. The measured and modeled reflected radiances at M10 (320-grit sandpaper) are shown for the diffuse-specular model.

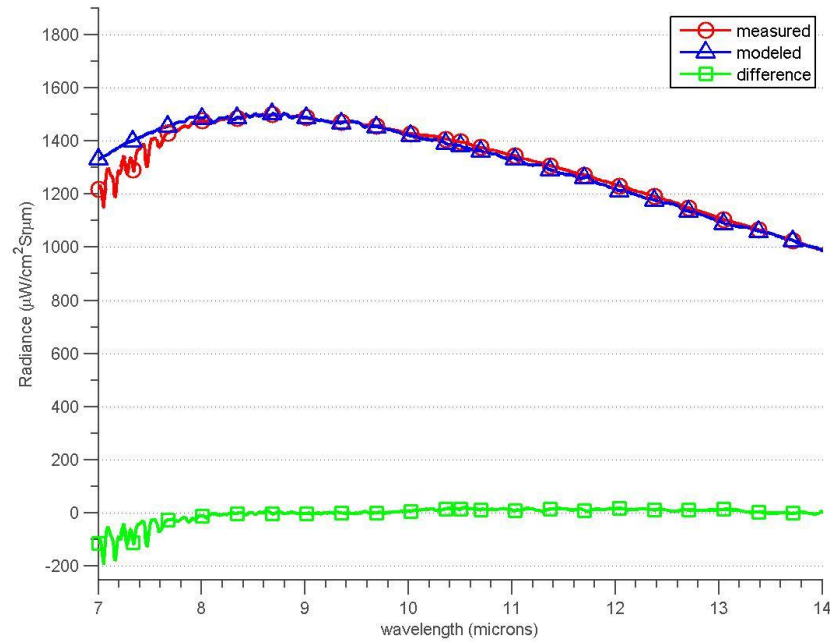


Figure 45. The measured and modeled reflected radiances at M3 (high emissivity, low reflectance material) are shown for the diffuse-specular model.

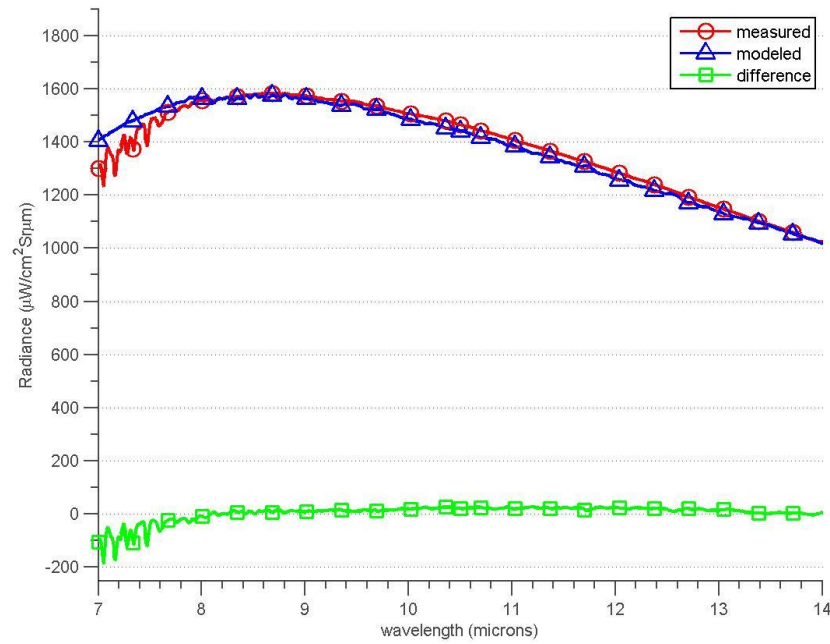


Figure 46. The measured and modeled reflected radiances at M11 (high emissivity, low reflectance material) are shown for the diffuse-specular model.

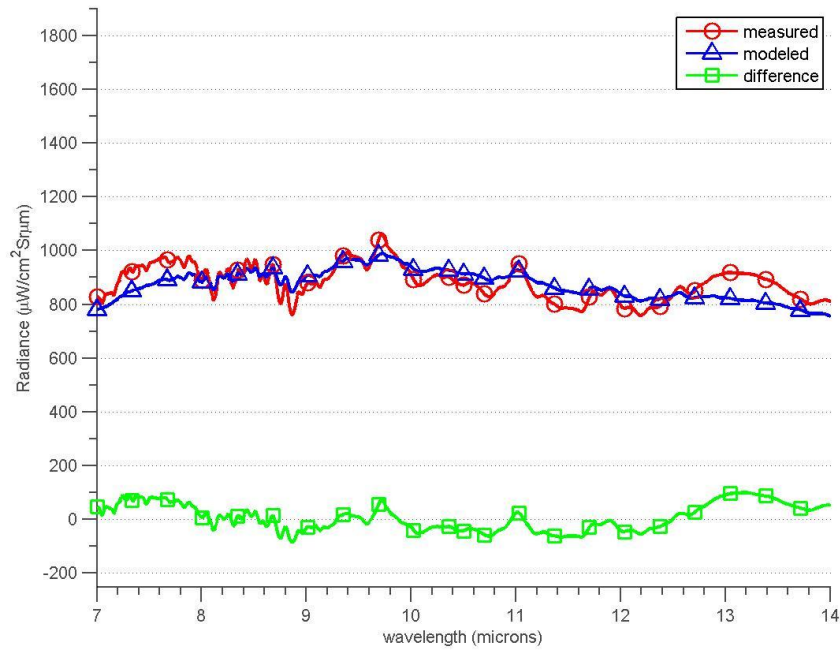


Figure 47. The measured and modeled reflected radiances at M4 (foamboard) are shown for the diffuse-specular model.

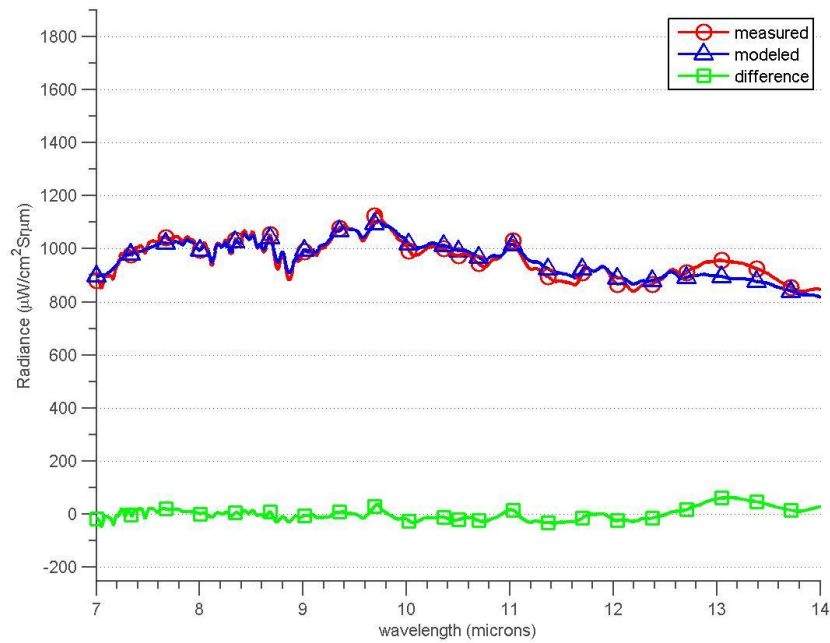


Figure 48. The measured and modeled reflected radiances at M12 (foamboard) are shown for the diffuse-specular model.

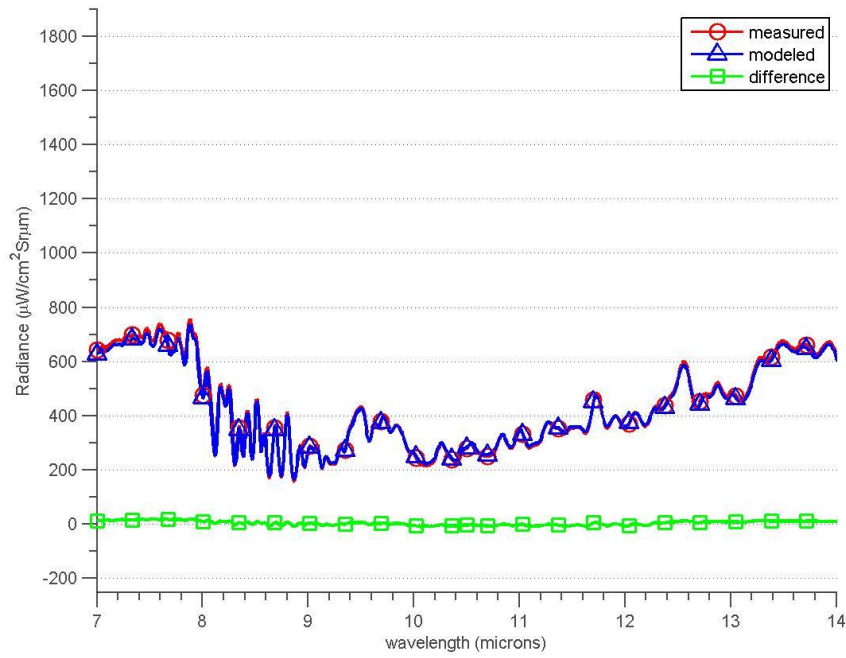


Figure 49. The measured and modeled reflected radiances at M5 (radiant barrier) are shown for the diffuse-specular model.

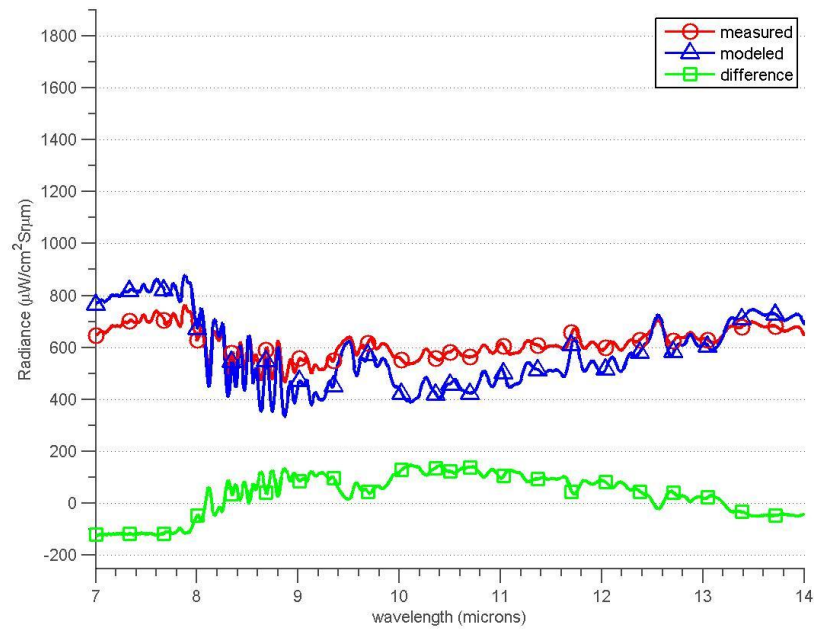


Figure 50. The measured and modeled reflected radiances at M13 (radiant barrier) are shown for the diffuse-specular model.

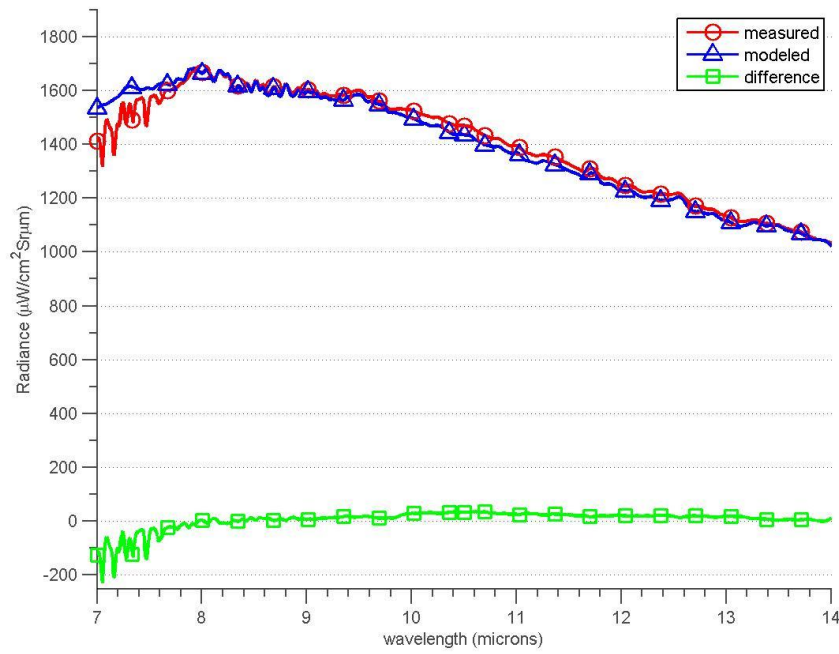


Figure 51. The measured and modeled reflected radiances at M6 (medium emissivity material) are shown for the diffuse-specular model.

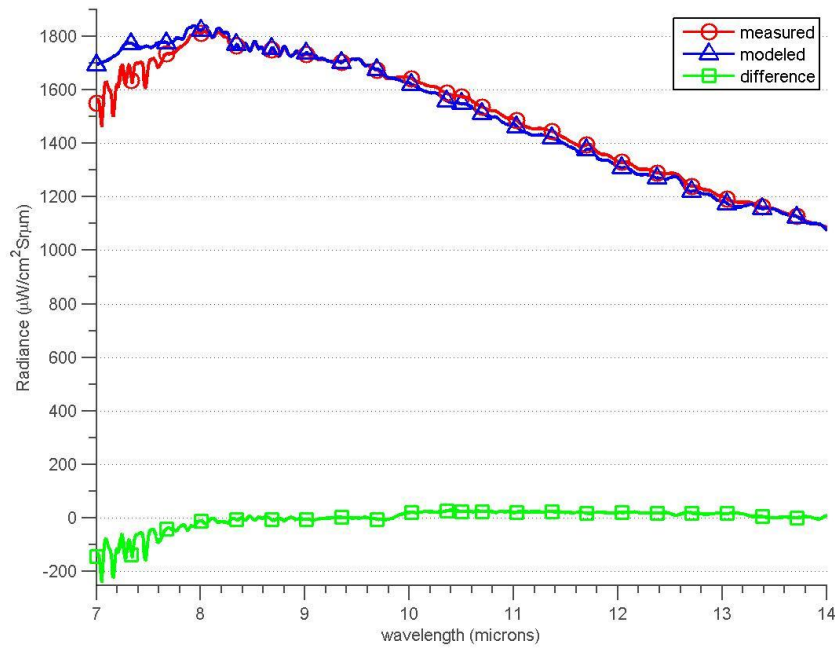


Figure 52. The measured and modeled reflected radiances at M14 (medium emissivity material) are shown for the diffuse-specular model.

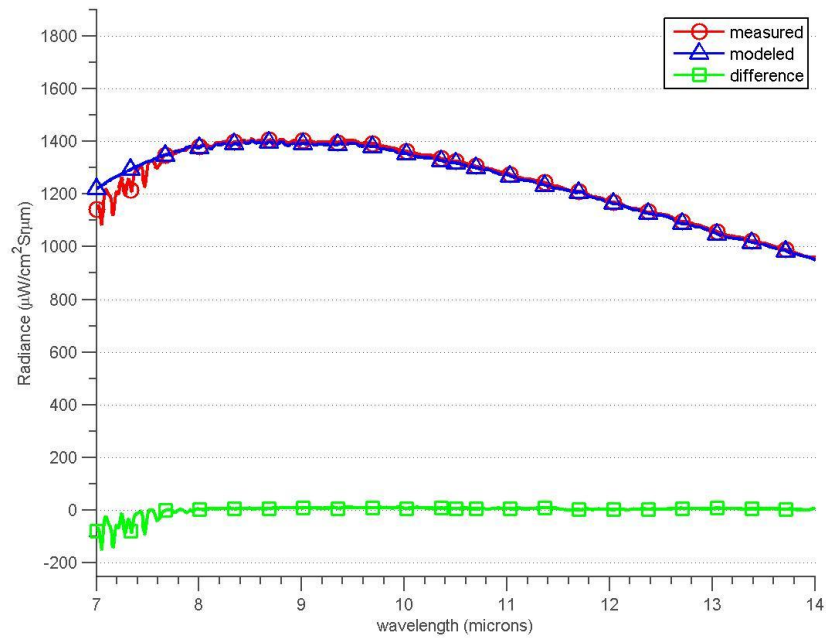


Figure 53. The measured and modeled reflected radiances at M7 (black vehicle paint) are shown for the diffuse-specular model.

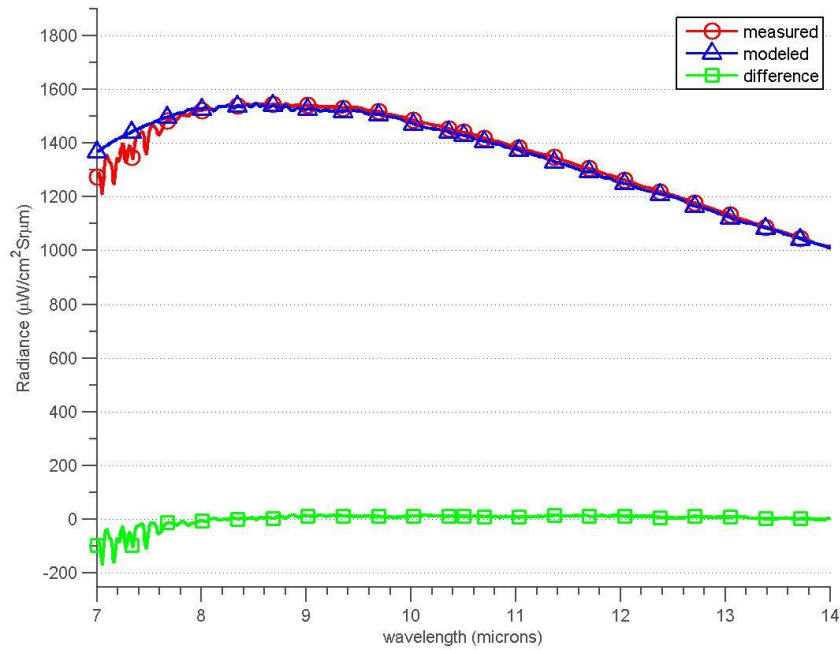


Figure 54. The measured and modeled reflected radiances at M15 (black vehicle paint) are shown for the diffuse-specular model.

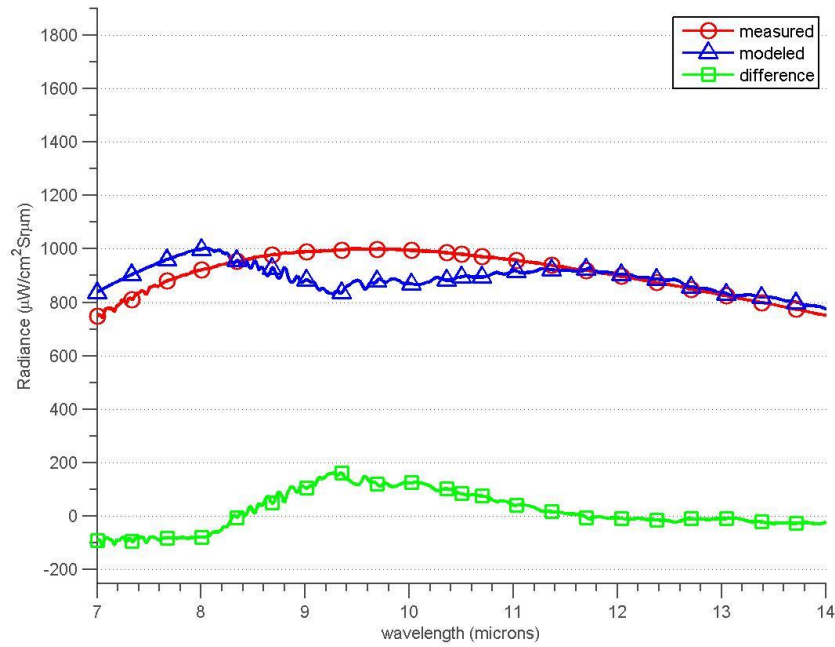


Figure 55. The measured and modeled reflected radiances at M8 (laminated safety glass) are shown for the diffuse-specular model.

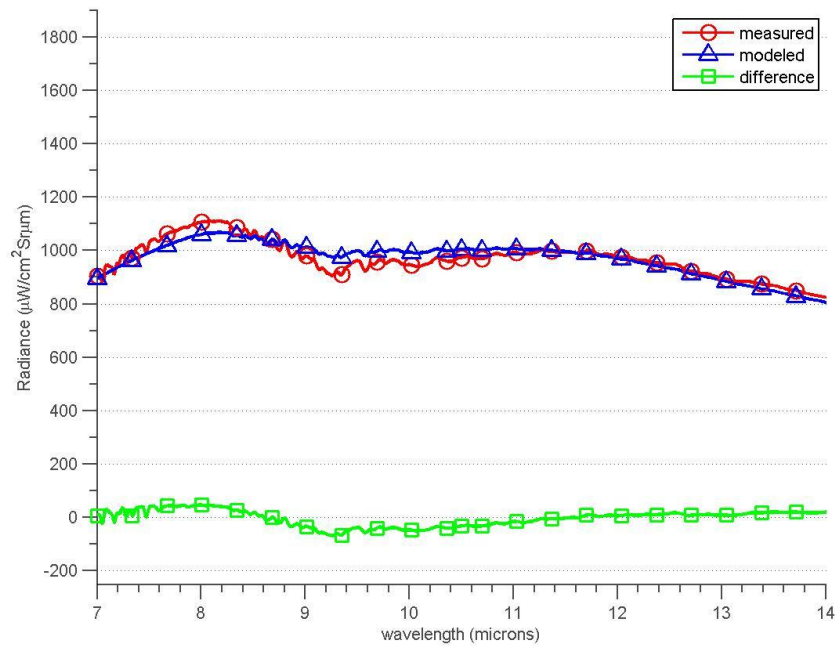


Figure 56. The measured and modeled reflected radiances at M16 (laminated safety glass) are shown for the diffuse-specular model.

The mean and standard deviation of the thermocouple temperatures are shown in Table 9, along with the optimized temperatures using the diffuse-specular model, for each panel. Table 10 shows the relative difference between the measured and optimized temperatures that was subsequently acquired.

For a more complete picture, Table 11 shows the corresponding relative differences between the measured and optimized, modeled spectra, and Table 12 shows the respective spectral angles for each panel.

Table 9. Mean and standard deviation of thermocouple temperatures, and diffuse-specular optimized panel temperatures.

Panel	Thermocouple Mean Temp (°C)	Thermocouple Standard Deviation (°C)	Optimized Temp (°C)
M1	56	0.26	64
M2	54	3.36	52
M3	53	0.36	56
M4	39	1.08	30
M5	29	0.54	28
M6	67	0.59	69
M7	48	0.47	51
M8	35	0.22	32
M9	60	0.33	60
M10	66	2.77	63
M11	57	0.42	59
M12	43	0.68	38
M13	35	0.85	107
M14	73	0.82	75
M15	52	0.98	57
M16	39	0.34	35

Table 10. Relative difference between measured and optimal panel temperatures using the diffuse-specular model.

Panel $\theta_{tip}=0^\circ$	Relative Difference (%)	Panel $\theta_{tip}=45^\circ$	Relative Difference (%)
M1	2.52	M9	0.08
M2	0.70	M10	0.80
M3	0.96	M11	0.64
M4	3.11	M12	1.49
M5	0.23	M13	19.04
M6	0.72	M14	0.59
M7	0.92	M15	1.39
M8	1.09	M16	1.24

Table 11. RMS relative difference between measured and modeled diffuse-specular reflected radiance data.

Panel $\theta_{tip}=0^\circ$	Relative Difference (%)	Panel $\theta_{tip}=45^\circ$	Relative Difference (%)
M1	4.57	M9	3.49
M2	1.61	M10	1.70
M3	2.34	M11	2.32
M4	5.65	M12	2.51
M5	1.79	M13	14.80
M6	2.54	M14	2.52
M7	1.70	M15	1.90
M8	7.77	M16	3.03

Table 12. SAM values between measured and modeled diffuse-specular reflected radiance data.

Panel $\theta_{tip}=0^\circ$	Spectral Angle ($^\circ$)	Panel $\theta_{tip}=45^\circ$	Spectral Angle ($^\circ$)
M1	2.67	M9	1.99
M2	0.88	M10	0.97
M3	1.27	M11	1.27
M4	3.20	M12	1.39
M5	0.76	M13	8.00
M6	1.45	M14	1.47
M7	0.91	M15	1.04
M8	4.48	M16	1.73

It is evident from Table 10 that most of the optimal panel temperatures were less than approximately 3% different than the measured thermocouple temperatures for all panels except M13. This means that there is very adequate agreement between what the diffuse-specular model simulated, and what the thermocouples recorded, when comparing the panel temperatures. The corresponding RMS relative difference in reflected radiance for each panel is less than approximately 8% for all panels, except most notably, again, M13. This means that the measured and modeled spectra for the panels agree closely in magnitude. The spectral angle between the measured and modeled spectral reflected radiance is also very low, less than approximately 4.5% for all panels except M13.

It is rather interesting that, for the diffuse-only model, both M5 and M13 were the worst-performing panels, while in the diffuse-specular model, M5 is actually modeled quite well, with a relative difference in temperature of 0.23%, and a relative difference in spectral radiance of 1.79%. It is likely that the reason for this is because the down-welling radiance did not vary significantly between the time when it was measured, and when the reflected radiance of panel M5 was measured. Furthermore, the use of the diffuse-specular model accounts for the radiance received in the specular direction of observation, and likely assisted in bringing the modeled reflected radiance much closer to the measured, than the diffuse-only model could. This, of course, is observed in the sense that the optimized temperature is very near the thermocouple temperature, as the panel's self-emission was not required to make up the difference in the measured and modeled reflected radiances.

It is slightly disturbing, however, that the diffuse-only and diffuse-specular results otherwise look fairly similar. Therefore, the next course of action is to look at the differences between the diffuse-only and diffuse-specular models.

Comparison of Diffuse-Only and Diffuse-Specular Models

The differences between the diffuse-only and diffuse-specular models are shown in Table 13 as a difference between the RMS relative differences given in Tables 7 and 11, respectively, and in Table 14 as the differences between spectral angles given in Tables 8 and 12, respectively. A positive number indicates that the diffuse-only model produced a lower metric, and therefore performed better. A negative number indicates that the diffuse-specular model performed better.

Table 13. Difference in RMS relative difference between measured and modeled reflected radiance between the diffuse-only and diffuse-specular models.

Panel $\theta_{tip}=0^\circ$	RMS Relative Difference Difference (%)	Panel $\theta_{tip}=45^\circ$	RMS Relative Difference Difference (%)
M1	0.12	M9	-0.38
M2	0.00	M10	0.00
M3	0.00	M11	0.00
M4	-0.31	M12	-0.17
M5	-11.27	M13	4.03
M6	0.02	M14	-0.01
M7	0.06	M15	-0.01
M8	0.94	M16	1.10

The data shown in Tables 13 and 14 does not conclude that the diffuse-specular method is better than the diffuse-only method, or vice versa. Panels M1/M9 and M5/M13 are inconclusive as the performance of the model depends on the tipping angle

of the panel. The diffuse-only model is as good or better for panels M6, M7, M8, and M16, as the values are negative.

Table 14. Difference in spectral angles between the diffuse-only and diffuse-specular models.

Panel $\theta_{tip}=0^\circ$	Spectral Angle ($^\circ$)	Panel $\theta_{tip}=45^\circ$	Spectral Angle ($^\circ$)
M1	0.12	M9	-0.39
M2	0.00	M10	0.00
M3	0.00	M11	0.00
M4	-0.31	M12	-0.18
M5	-6.57	M13	2.96
M6	0.02	M14	-0.01
M7	0.07	M15	0.00
M8	0.90	M16	1.12

The diffuse-specular model, however, does not produce a large specular contribution to radiance for panels with a very low SDR, and so should not produce results that are much worse than those of the diffuse-only model. This is supported as all differences shown in Table 13 are less than 1.2%, except for panels M5 and M13. Panels M4/M12, on the other hand, are the only ones definitively better simulated using the diffuse-specular model. This does not necessarily have a strong connection to their SDR since it is also very low, as shown in Figure A4 in Appendix A. Lastly, these results are eerily similar to the results of the spectral angle analysis.

The lack of clear-cut evidence that shows one model as superior to the other suggests that the models were largely affected by variation in the data. This has so far been supported by both the standard deviation of the down-welling measurements and the large variations in relative difference in Infragold® modeled versus measured reflected radiance. In other words, there is too much variation in the down-welling radiance,

which is further exasperated by the fact that measurements were separated in time, where the measured down-welling radiance for a particular panel may change by the time the panel's reflected radiance is actually measured.

PLEXUS as a Tool for Reverse Radiative Transfer Modeling

Figures 15-18 showed the comparison of the mean field-collected sky radiances versus the PLEXUS-generated sky radiances. Additionally, in order to quantify the difference between the two, the mean relative difference (as calculated using Equation (51)) across all wavelengths of interest (7-14 μ m) is presented in Table 15.

Table 15. The mean relative difference between mean measured down-welling radiance and PLEXUS-generated down-welling radiance is presented per zenith angle.

θ_{sky} (Degrees from zenith)	Relative Difference (%)
0	34.07
30	20.18
60	30.08
90	13.76

The presented data suggests that it is not a trivial matter to generate realistic data using PLEXUS. The mean relative differences range from 13.76% to 34.07%, which is anecdotally too high of an error for this generated down-welling radiance to be used as a replacement for measured down-welling radiance values. The most likely reason for the differences is that cloud cover data was not rigorously utilized in estimating the proper parameters within PLEXUS. There could be additional unaccounted radiance as the horizon on-set was certainly not flat, and was likely higher than that modeled, and there was certainly scattering due to up-welling radiance of nearby objects, which would

produce yet more radiance that was neither measured, nor modeled.

Reverse Radiative Transfer Model

It is of great interest to be able to calculate a material's spectral reflectance as viewed from a remote location. This would allow an observer to determine what type of material is being observed, and to detect materials of interest when provided with a cross-referencing database.

The diffuse-only reverse radiative transfer model was used as it has only one unknown variable, the HDR. Using the diffuse-specular reverse radiative transfer model would require a solution in two unknown variables, DDR and SDR, which would be more difficult to do. Furthermore, given the results in Tables 13 and 14, it may even be futile to attempt this, when there is no notable difference between the diffuse-only and diffuse-specular models.

The relative differences between measured and modeled spectral reflected radiances are presented in Table 16, while the spectral angles between them are presented in Table 17. All applicable spectral reflectance plots may be found in Appendix C.

Table 16. Relative difference between SOC-100 reflectometer measured and reverse-modeled reflectance data for panels across 7-14 μ m.

Panel $\theta_{tip}=0^\circ$	Relative Difference	Panel $\theta_{tip}=45^\circ$	RMS Reflectance (HDR)
M1	4.79	M9	5.88
M2	55.13	M10	51.41
M3	56.72	M11	55.03
M4	186.28	M12	52.53
M5	3300.70	M13	3.44
M6	15.58	M14	15.34
M7	61.04	M15	63.56
M8	1032.80	M16	227.50

Table 17. SAM values between SOC-100 reflectometer measured and reverse, diffuse-only modeled reflectance data for panels across 7-14 μ m.

Panel $\theta_{tip}=0^\circ$	Spectral Angle ($^\circ$)	Panel $\theta_{tip}=45^\circ$	Spectral Angle ($^\circ$)
M1	2.86387	M9	3.3828
M2	19.9842	M10	19.782
M3	25.4623	M11	27.3651
M4	59.0434	M12	18.6561
M5	86.4766	M13	1.94943
M6	8.20132	M14	8.04892
M7	27.2356	M15	29.7188
M8	54.0575	M16	13.5104

Some of the relative differences in Table 16 unfortunately are large, over 100%. This is a result of the spectral reflectance being too close to zero, on average, driving the relative differences to very high values. Nevertheless, it is still a fair indicator of how well the spectral reflectance is modeled, when paired with the spectral angle values in Table 17. It appears that the best-modeled materials are M1/M9 and M6/M14. The only correlation, when observing their spectral reflectances as measured by the SOC-100 and shown in Appendix A, is that they all have a low SDR. More interestingly, M1/M9 are the panels with the highest mean DDR over the 7-14 μ m range. If anything, this exercise suggests that the spectral reflectance of a material is most easily backed out for materials that have high DDR. This is likely because materials with a high DDR (diffuse directional reflectance) would be more correctly modeled using a diffuse-only reverse model, whereas materials with appreciable SDR, and lower DDR, would be modeled less accurately as their specular properties would not be taken into account in a diffuse-only reverse model.

Conversely to M1/M9, M5 is the worst-modeled material in both Tables 16 and 17. It has a high HDR, but is very specular with a relatively low DDR. The same material, M13, however, is actually the best-modeled material in both Tables 16 and 17. More importantly, the results in Table 16 are opposite of those in Table 11, altogether, and also Table 7 except for panel M5. This seems to be due to the fact that the reverse-modeled reflectances are derived from the diffuse-only model – the two are essentially the same inequality applied in ways opposite of one another. Expectedly, if the self-emission of each panel is increased such that the modeled reflected radiance matches the measured reflected radiance, this would have the effect of drifting the reverse-modeled reflectance away from its previous value. Since a decrease in relative differences for the forward models results to an increase in relative differences for the reverse model, this suggests that, since both are coupled and dependent on the measured HDR, measured reflected radiance, and measured down-welling radiance, then the relationship between the two will be fixed. This relationship appears to be inverse in nature as an increase in one relative difference, appears to result in a decrease in the other's relative difference.

Summary

In this chapter, the important practices used in the models, spline interpolation to resample data and integration of hemispherical radiance, were shown to produce very accurate results. Furthermore, the solar contribution to the models was shown to be rather insignificant when compared to the present down-welling irradiances, since none of the data was collected with the Sun at the specular angle with respect to the observer.

The overall performance of the diffuse-only and diffuse-specular radiative transfer models was presented. The specular-diffuse model was not shown to be more accurate than the diffuse-only radiative transfer model, likely due to the time-based variation in down-welling radiance data.

Lastly, a diffuse-only reverse radiative transfer model was shown to produce satisfactory results in calculating the HDR of a few materials only. The performance of this method was also dependent on the tip angle of the panels.

VI. Conclusions and Recommendations

Chapter Overview

In this chapter, appropriate conclusions are drawn from the given results by answering the previously-posed investigative questions. Then, the significance of the research is re-affirmed, and recommendations are given for future research in this area.

Investigative Questions Answered

I have found that both diffuse-only and diffuse-specular radiative transfer models produce reflected radiance values within a relative difference of 8% from the measured reflected radiances for all tested panels except the radiant barrier. Thus, the diffuse-only method is much more accurate for materials that have very low specular reflectances, unlike the worst-performing panels M5 and M13 in that case. However, the diffuse-specular model was able model panel M5 very accurately, though it was unable to match that for the tipped radiant barrier panel, M13, suggesting that it is a good step towards modeling highly specular materials, though the experimental conditions must be much more controlled in order to eliminate external sources of error. Since there was no significant evidence that either model performs better than the other, aside in the case of panel M5, it appears most likely that variation in time in the down-welling radiance produces errors that overshadow the difference in the diffuse-only and diffuse-specular models. Additionally, the radiances may be affected differently at different panels due to variation in adjacency effects from surrounding objects, such as other tipped panels!

The current version of PLEXUS was found insufficient in generating accurate sky down-welling radiance for modeling the reflected radiance of the panels. The likely

cause of this is a combination of that it uses an outdated version of MODTRAN, and that cloud profiles were not rigorously taken into account when generating the down-welling radiance. Additionally, the down-welling radiances were shown to have quite a bit of variation, further adding to the difficulty in using PLEXUS to model these variations.

The diffuse-only reverse radiative transfer model was shown to have some accuracy when modeling the HDR of a material, but, on average, did not have reliable results as evidenced by the spectral angles produced from most panels.

Conclusions of Research

This paper investigated the use of diffuse-only and diffuse-specular radiative transfer models as a replacement for the more-accurate (but much more computationally intensive) spectral BRDF-based radiative transfer models. The use of diffuse-only and diffuse-specular radiative transfer models showed that both may accurately represent a variety of materials. The diffuse-only radiative transfer model, as may be expected, loses accuracy when it is used to model materials that have a high specular reflectance. This suggests that, if simplicity is of particular importance, a diffuse-only model may sufficiently represent the reflected radiance of a material, depending on the accuracy required, as long as that material is not highly reflective and specular.

The specular properties of materials become even more important to take into account in remote sensing applications. As was shown, the diffuse-only reverse radiative transfer model was able to reproduce the spectral HDR of the diffuse panels better than the specular panels.

Lastly, the variation in down-welling radiance unfortunately were larger than the variation in radiance produced by either model, thereby overshadowing any difference between the diffuse-only and the diffuse-specular model. This made it impossible to see the smaller differences between the two models, and suggests that taking the next step – BRDF-based modeling – may be a futile endeavor, as the radiance differences produced with this model may also be overshadowed by the inherent variation in the down-welling radiance data.

Lastly, only measured sky down-welling radiance was utilized in the reverse radiative transfer model. This was done because I was not able to reproduce realistic sky down-welling radiance using PLEXUS (which uses MODTRAN 4).

Significance of Research

This research has shown that the specular properties of materials must be taken into account when they are used in radiative transfer models, though they may be ignored if the modeled materials will not be highly reflective or highly specular. This is of interest to both remote sensing and the computer-generated graphics industry. The criticality of this becomes even more apparent when using reverse radiative transfer models, which is of interest in remote sensing for backing out the spectral reflectance of a material. As shown in this research, reverse models are a lot more sensitive to errors in measurements.

Additionally, this research shows that the variation and uncertainty in down-welling measurements is of great interest when attempting to gauge the accuracy of different radiative transfer models, as no such comparison may be made if the difference

is minimal compared to the variation in measured data. This suggests that the field conditions must be more ideal in order to perform an experiment to compare the accuracy of radiative transfer models.

Recommendations for Future Research

Future research should focus on further improving the accuracy of the radiative transfer models. This includes finding better ways of accounting for the observation angles during collection of data, such that all sources of error are satisfactorily minimized. This is, of course, a requirement, as the large number of variables make it increasingly difficult to narrow down sources of error within the radiative transfer models.

Furthermore, a more highly controlled experiment should be made, where the field-collected data is taken in a much shorter time-span, or during very atmospherically-uneventful days (no winds or clouds).

A natural extension to this research is to use modeled sky down-welling radiance as opposed to the measured sky down-welling radiance. This is needed so that the reverse radiative transfer model may truly be stand-alone, such that it can be used in a remote sensing scenario. Two modeling utilities that come to mind are MODTRAN 5 and AFIT's own Laser Environmental Effects Definition and Reference (LEEDR). It will likely be imperative, however, that the modeling include as many relevant meteorological parameters that match the conditions during collection as possible.

Lastly, the research needs to be expanded to include the BRDF-based modeling of the reflected radiance of the materials used. This expansion requires that BRDF data be

collected over a number of wavelengths for each panel of interest. The number of wavelengths would have to be large enough such that there will exist sufficient information to show whether, and in what specific cases, BRDFs have a large impact on the radiance reflected and emitted from the panels.

Backing out the spectral reflectance of a panel was simple enough in a diffuse-only case (HDR). Future work may include developing a method to back out the spectral DDR and SDR of a material, though the problem is inherently more complicated as the solution is in two variables. Since the correct DDR and SDR are determined from a spectral reflected radiance equation, similar to but more complicated than, that shown in equation (31), they may vary in different ways but still combine to a single spectral HDR. This means that the correct DDR and SDR may have to be determined using additional limiting criteria.

Appendix A

HDR, DDR, and SDR Data Figures

The following plots show the HDR, SDR, and DDR of each panel when measured at an angle of incidence of 30° .

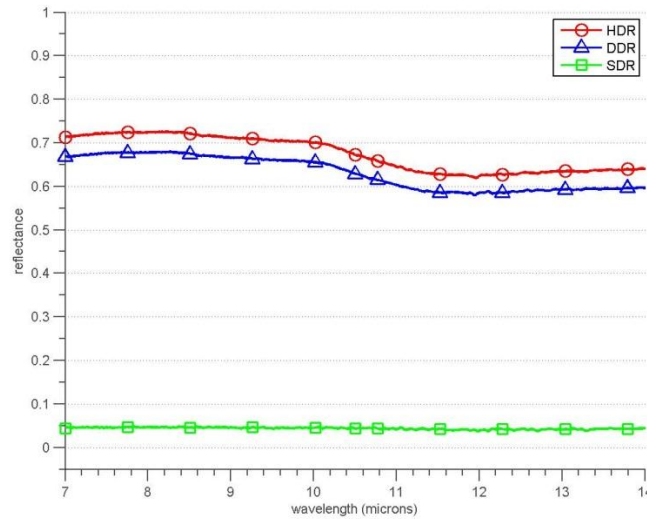


Figure A1. The HDR, SDR, and DDR for panels M1 and M9 (flame-sprayed aluminum) are shown at an angle of incidence of 30° .

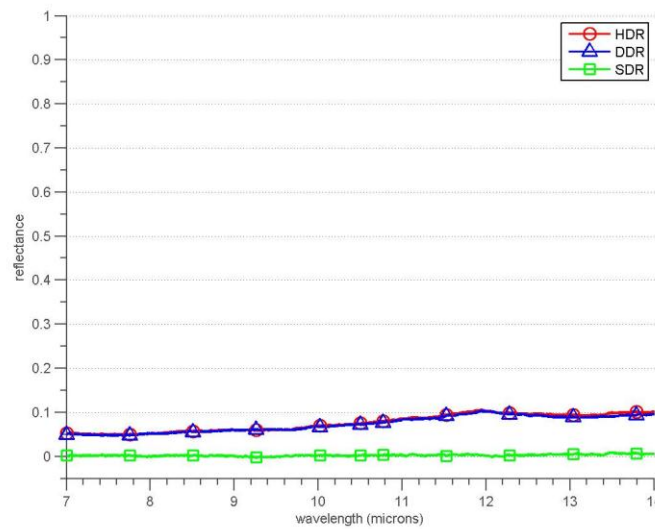


Figure A2. The HDR, SDR, and DDR for panels M2 and M10 (320-grit sandpaper) are shown at an angle of incidence of 30° .

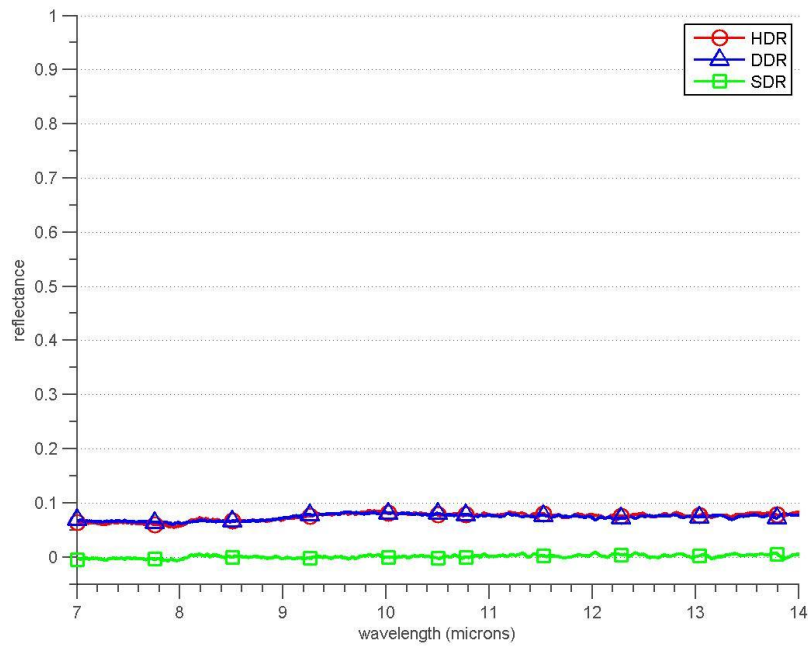


Figure A3. The HDR, SDR, and DDR for panels M3 and M11 (high emissivity, low reflectance material) are shown at an angle of incidence of 30° .

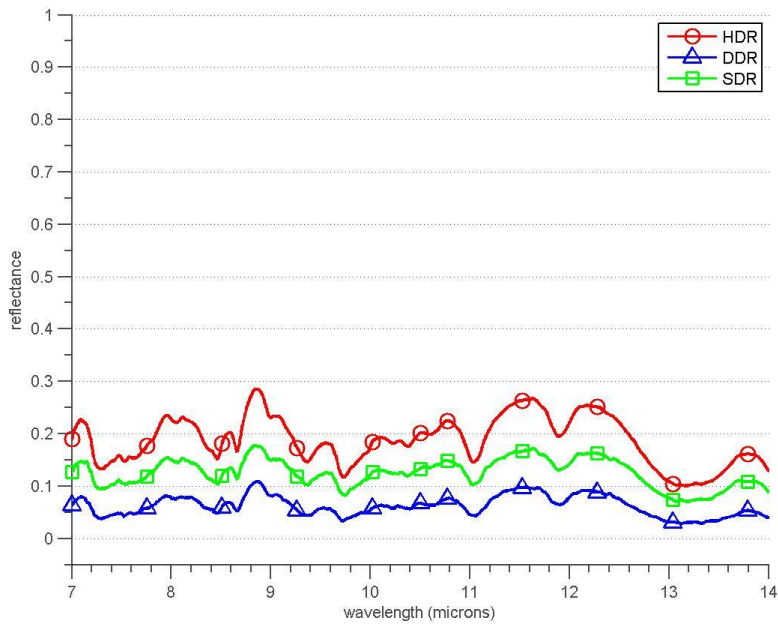


Figure A4. The HDR, SDR, and DDR for panels M4 and M12 (foamboard) are shown at an angle of incidence of 30° .

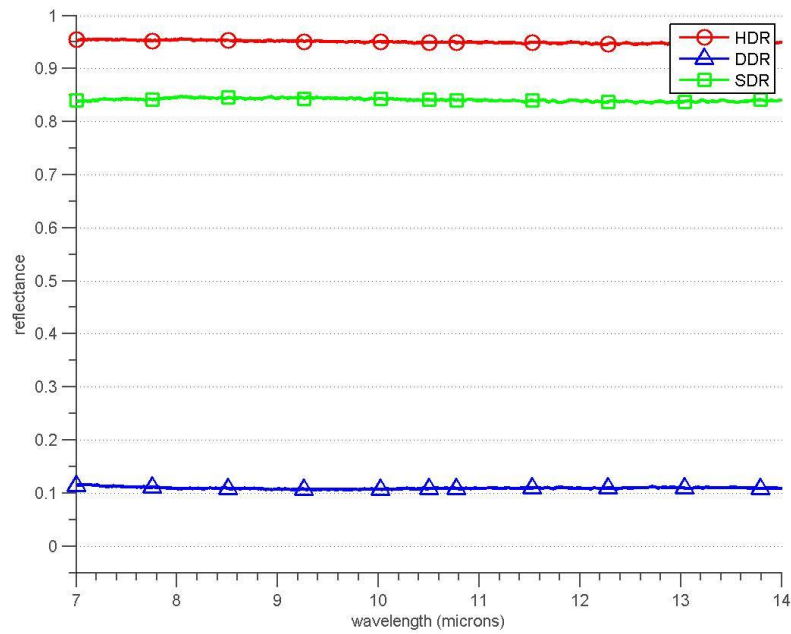


Figure A5. The HDR, SDR, and DDR for panels M5 and M13 (radiant barrier) are shown at an angle of incidence of 30°.

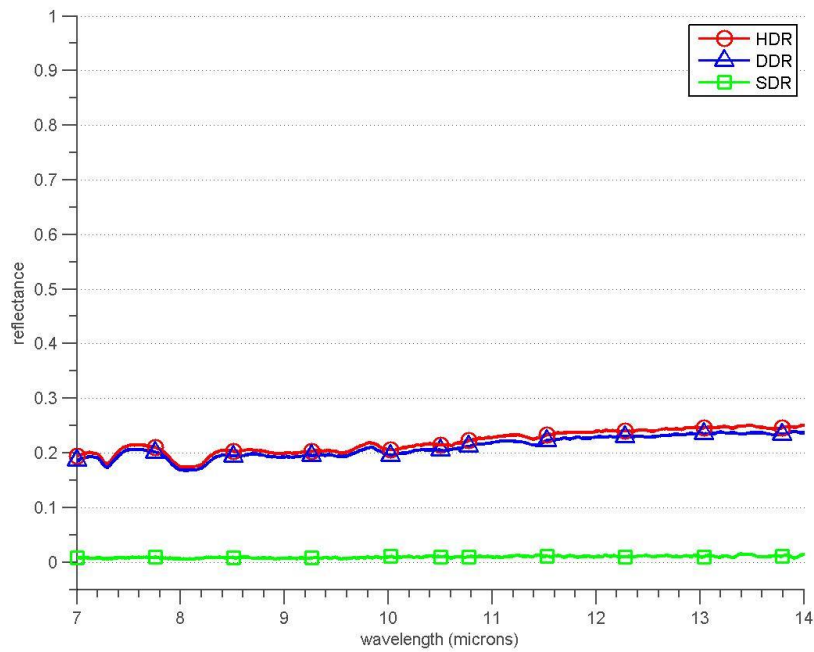


Figure A6. The HDR, SDR, and DDR for panels M6 and M14 (medium emissivity material) are shown at an angle of incidence of 30°.

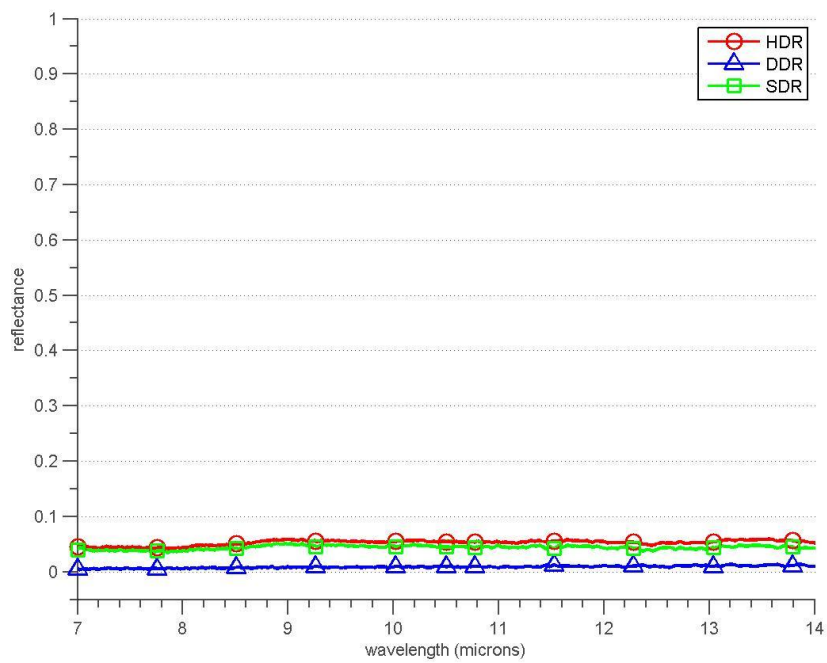


Figure A7. The HDR, SDR, and DDR for panels M7 and M15 (black vehicle paint) are shown at an angle of incidence of 30°.

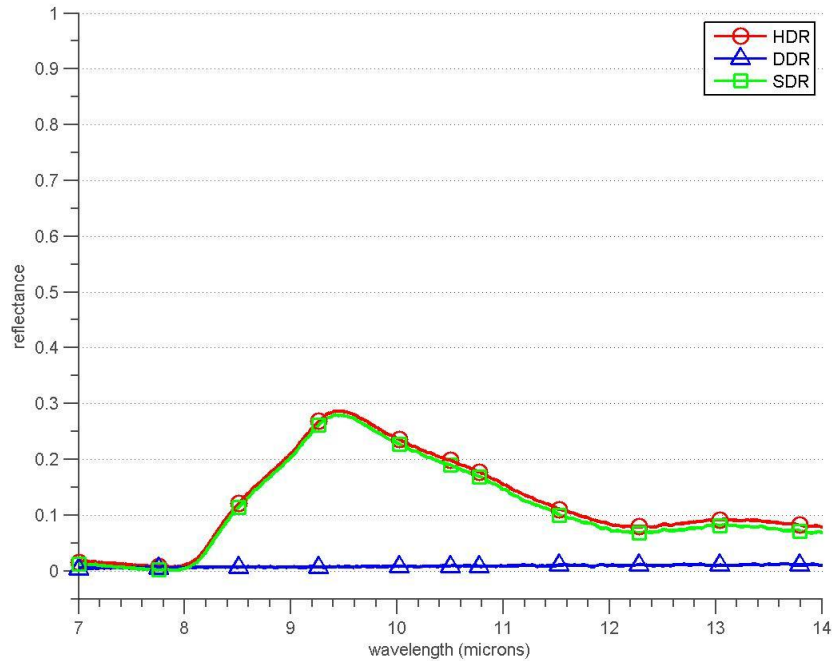


Figure A8. The HDR, SDR, and DDR for panels M8 and M16 (laminated safety glass) are shown at an angle of incidence of 30°.

Appendix B

Angular HDR, DDR, and SDR Reflectance of Materials

The following figures show the interpolated HDR, DDR, and SDR of materials as measured by the SOC-100, and extrapolated for incident angles below 20° and over 70° .

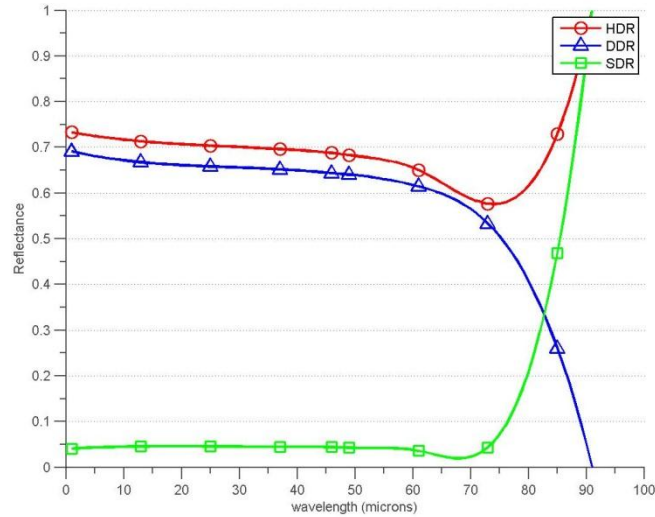


Figure B1. The HDR, SDR, and DDR for panels M1 and M9 (flame-sprayed aluminum) are shown at $10\mu\text{m}$ as a function of angle of incidence.

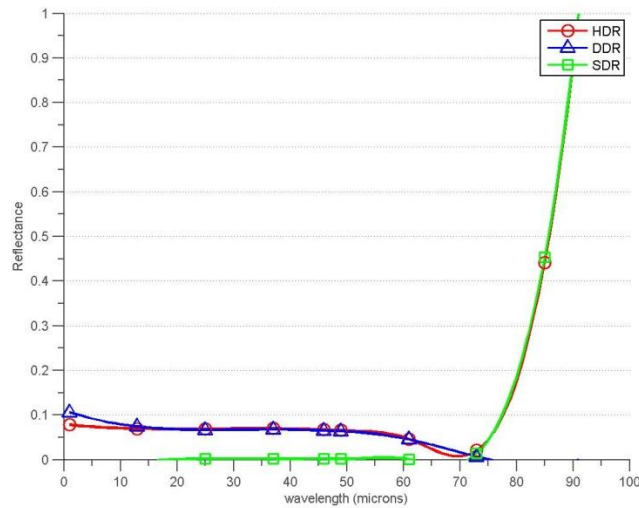


Figure B2. The HDR, SDR, and DDR for panels M2 and M10 (320-grit sandpaper) are shown at $10\mu\text{m}$ as a function of angle of incidence.

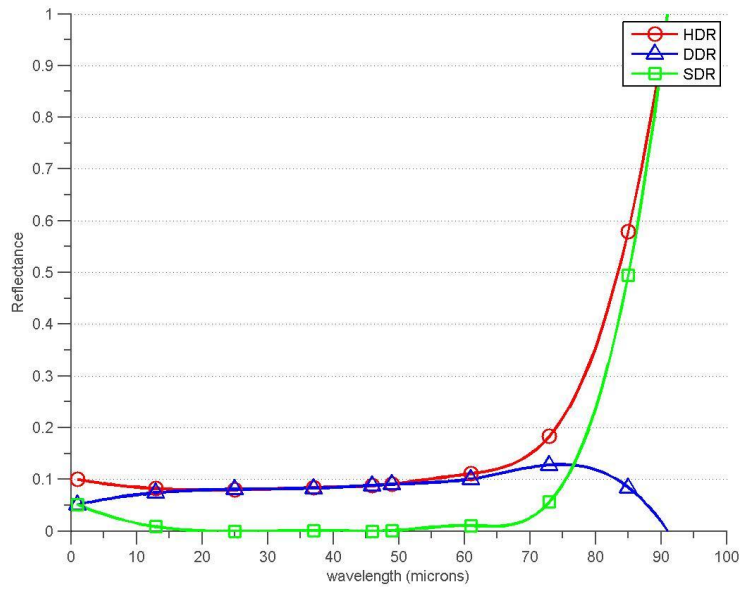


Figure B3. The HDR, SDR, and DDR for panels M3 and M11 (high emissivity, low reflectance material) are shown at $10\mu\text{m}$ as a function of angle of incidence.

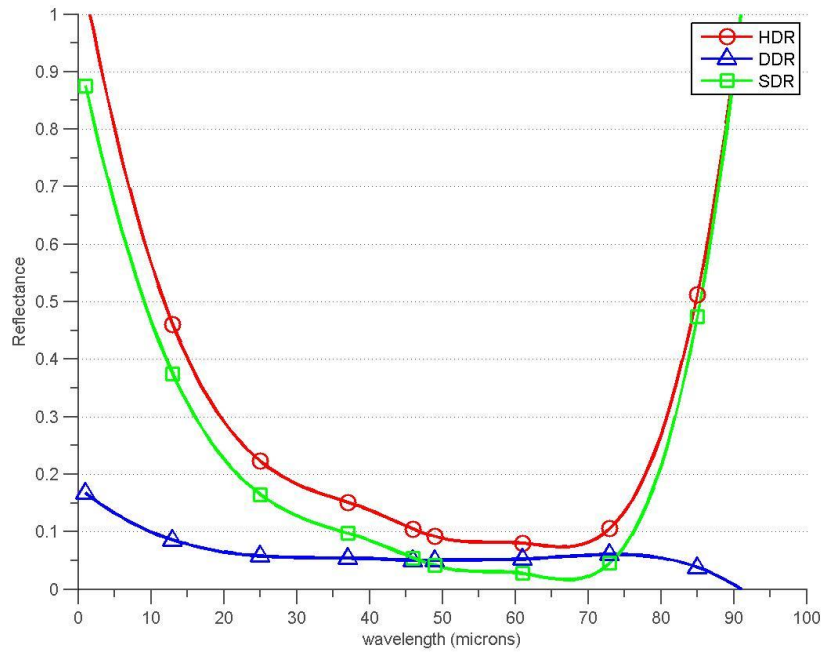


Figure B4. The HDR, SDR, and DDR for panels M4 and M12 (foamboard) are shown at $10\mu\text{m}$ as a function of angle of incidence.

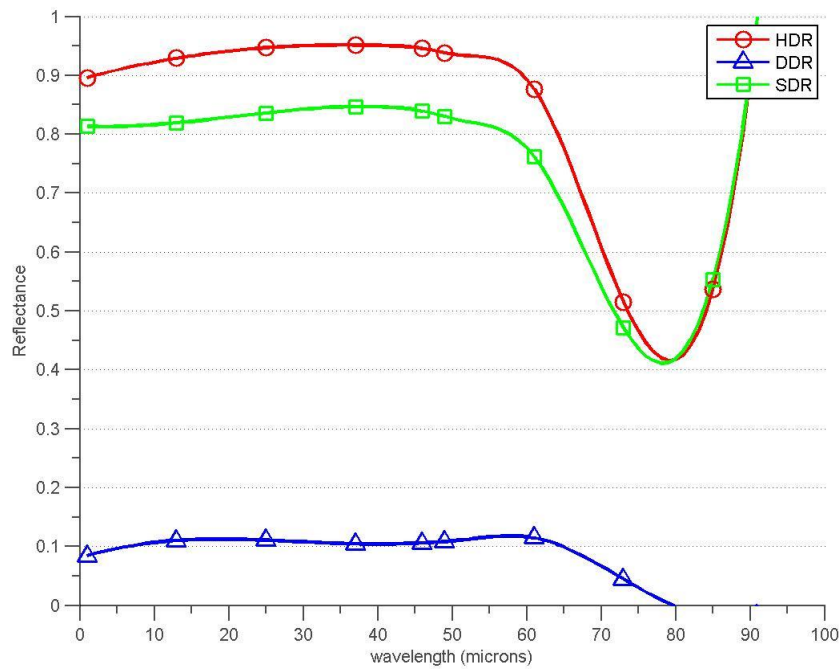


Figure B5. The HDR, SDR, and DDR for panels M5 and M13 (radiant barrier) are shown at $10\mu\text{m}$ as a function of angle of incidence.

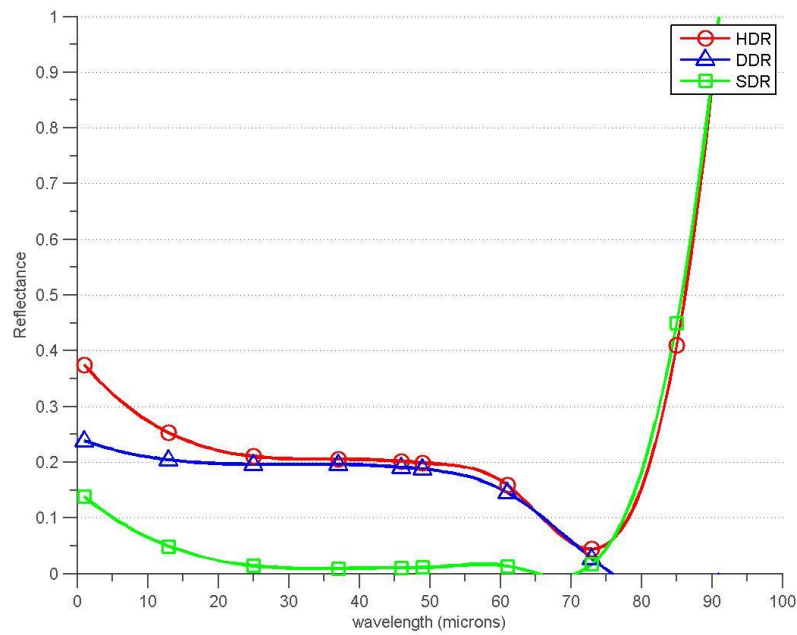


Figure B6. The HDR, SDR, and DDR for panels M6 and M14 (medium emissivity material) are shown at $10\mu\text{m}$ as a function of angle of incidence.

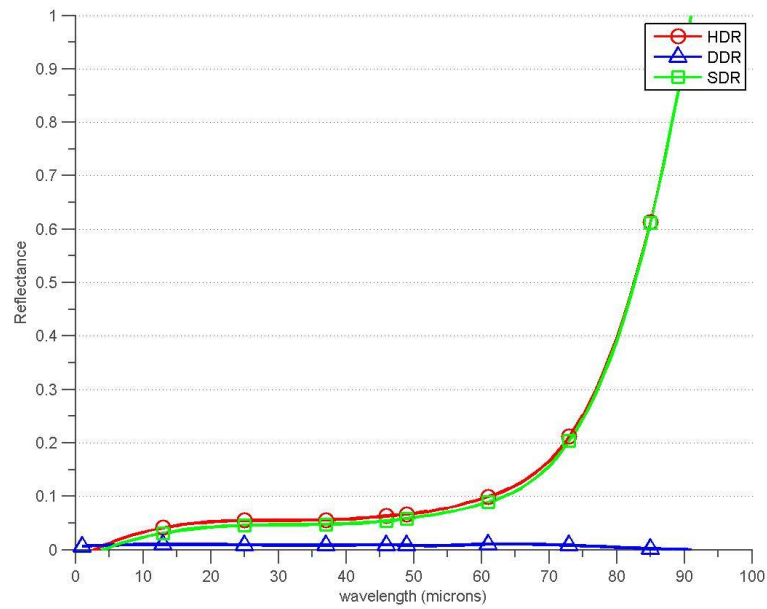


Figure B7. The HDR, SDR, and DDR for panels M7 and M15 (black vehicle paint) are shown at $10\mu\text{m}$ as a function of angle of incidence.

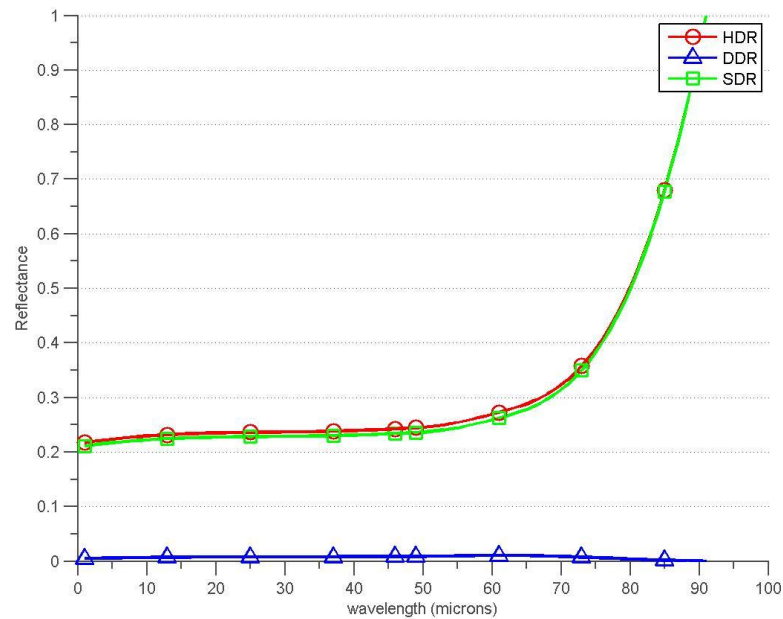


Figure B8. The HDR, SDR, and DDR for panels M8 and M15 (laminated safety glass) are shown at $10\mu\text{m}$ as a function of angle of incidence.

Appendix C

Measured and Reverse-Modeled HDR

The following figures show the measured and reverse modeled HDR at each panel for the diffuse-only model, where the collected HDR data was interpolated to match the appropriate viewing orientation.

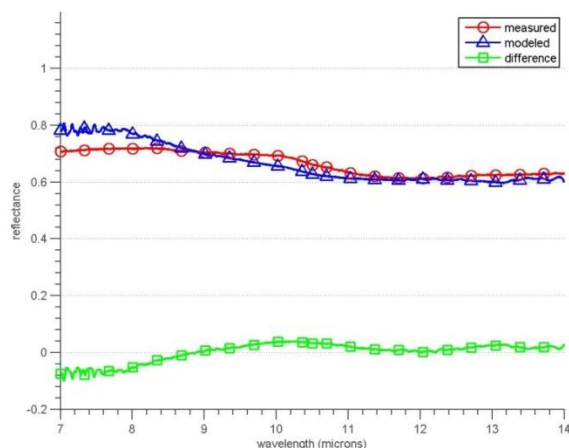


Figure C1. The measured and reverse modeled HDR at M1 (flame-sprayed aluminum) are shown for the diffuse-only reverse model. The measured HDR shown is interpolated to match the observation angle which was used for the model.

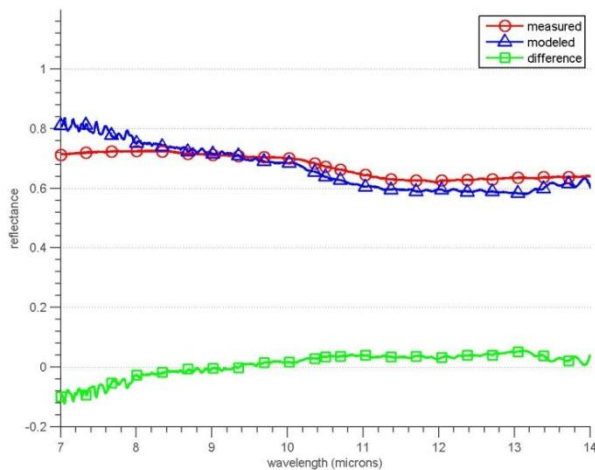


Figure C2. The measured and reverse modeled HDR at M9 (flame-sprayed aluminum) are shown for the diffuse-only reverse model. The measured HDR shown is interpolated to match the observation angle which was used for the model.

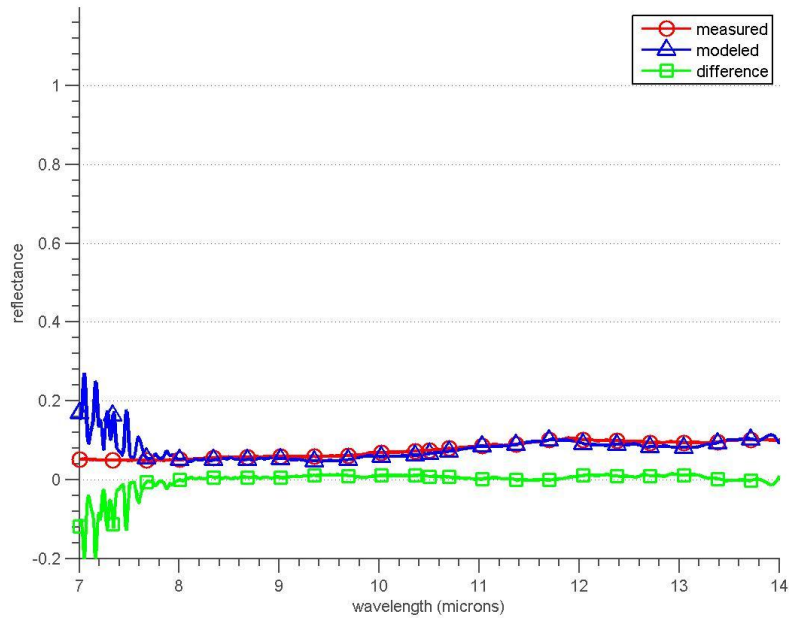


Figure C3. The measured and reverse modeled HDR at M2 (320-grit sandpaper) are shown for the diffuse-only reverse model. The measured HDR shown is interpolated to match the observation angle which was used for the model.

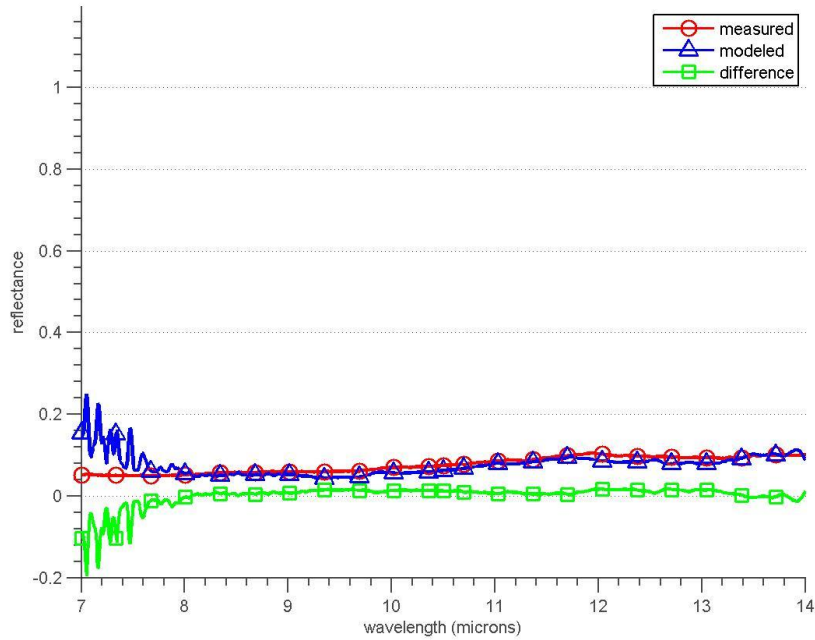


Figure C4. The measured and reverse modeled HDR at M10 (320-grit sandpaper) are shown for the diffuse-only reverse model. The measured HDR shown is interpolated to match the observation angle which was used for the model.

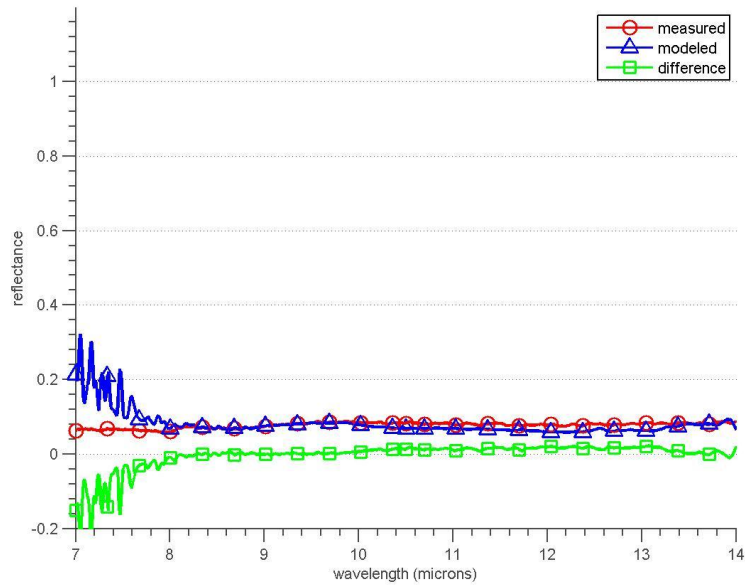


Figure C5. The measured and reverse modeled HDR at M3 (high emissivity, low reflectance material) are shown for the diffuse-only reverse model. The measured HDR shown is interpolated to match the observation angle which was used for the model.

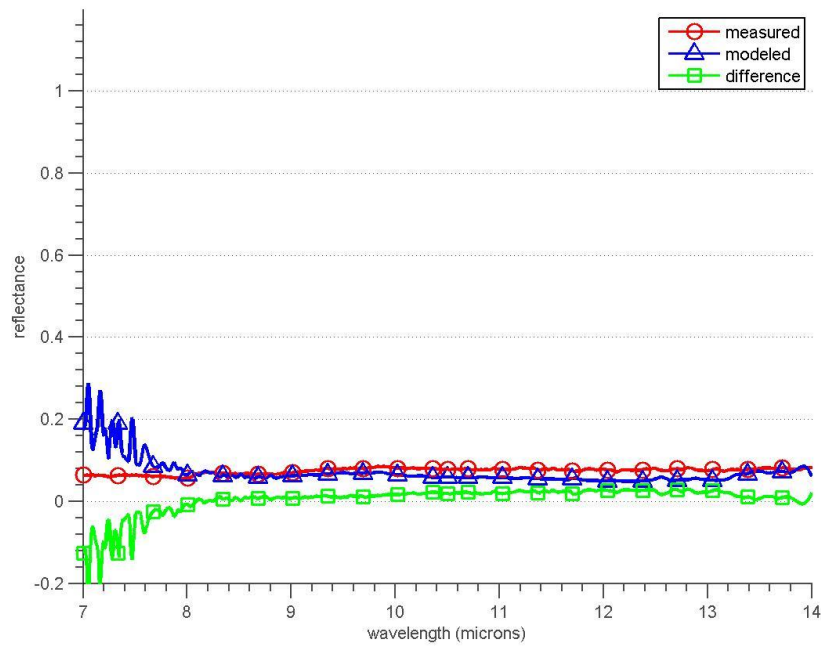


Figure C6. The measured and reverse modeled HDR at M11 (high emissivity, low reflectance material) are shown for the diffuse-only reverse model. The measured HDR shown is interpolated to match the observation angle which was used for the model.

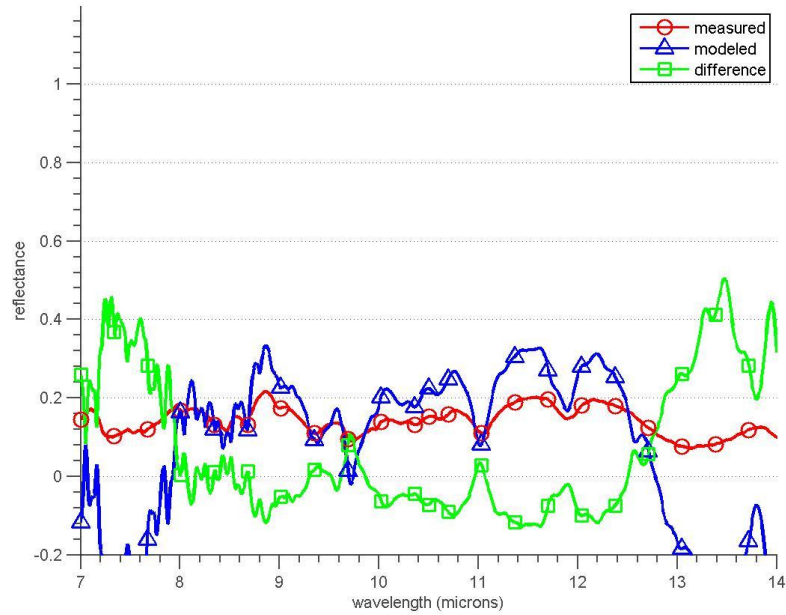


Figure C7. The measured and reverse modeled HDR at M4 (foamboard) are shown for the diffuse-only reverse model. The measured HDR shown is interpolated to match the observation angle which was used for the model.

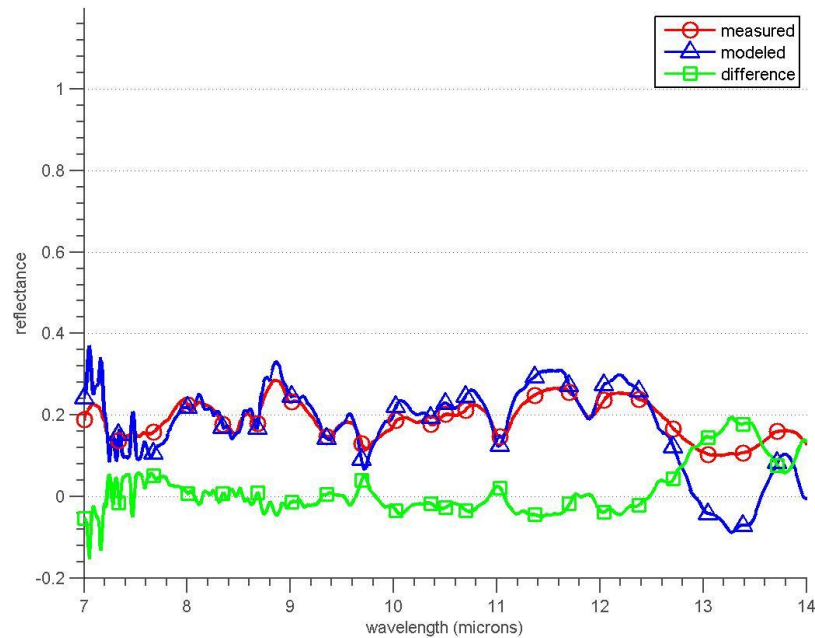


Figure C8. The measured and reverse modeled HDR at M12 (foamboard) are shown for the diffuse-only reverse model. The measured HDR shown is interpolated to match the observation angle which was used for the model.

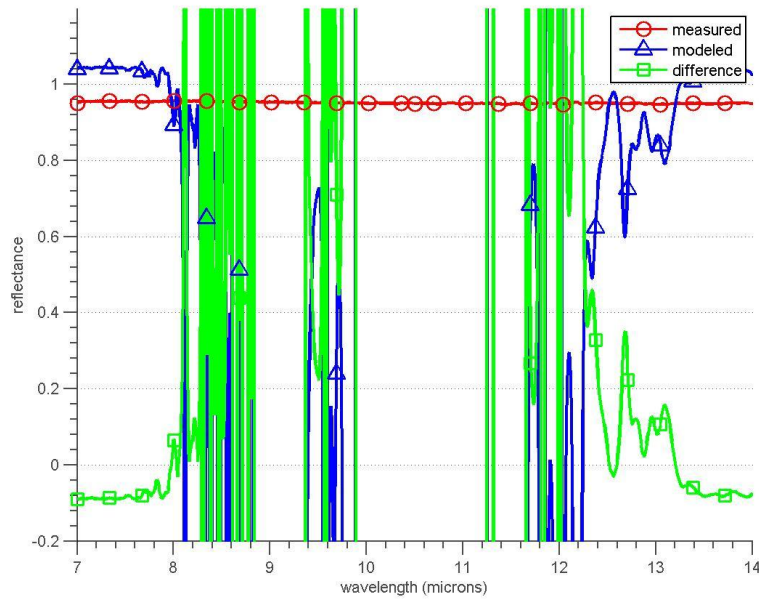


Figure C9. The measured and reverse modeled HDR at M5 (radiant barrier) are shown for the diffuse-only reverse model. The measured HDR shown is interpolated to match the observation angle which was used for the model.

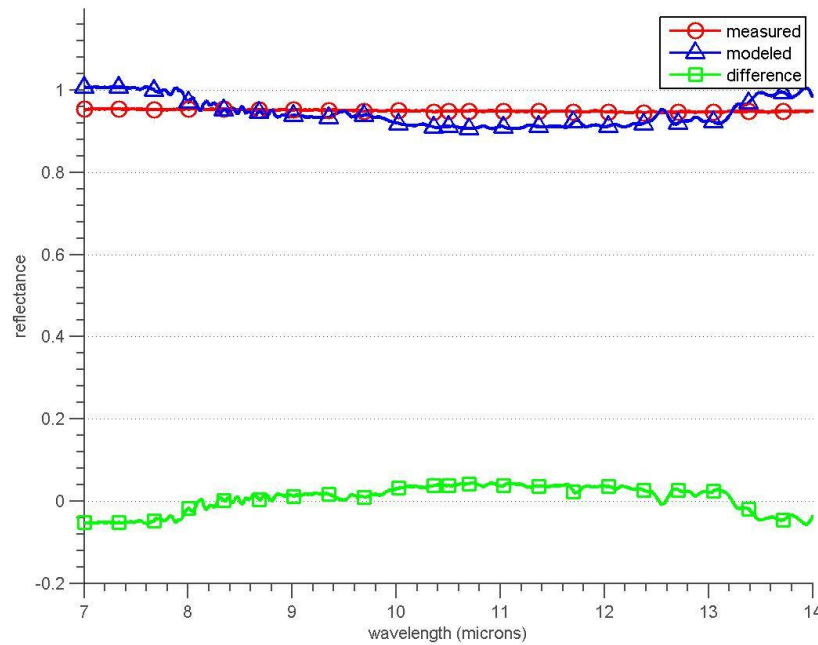


Figure C10. The measured and reverse modeled HDR at M13 (radiant barrier) are shown for the diffuse-only reverse model. The measured HDR shown is interpolated to match the observation angle which was used for the model.

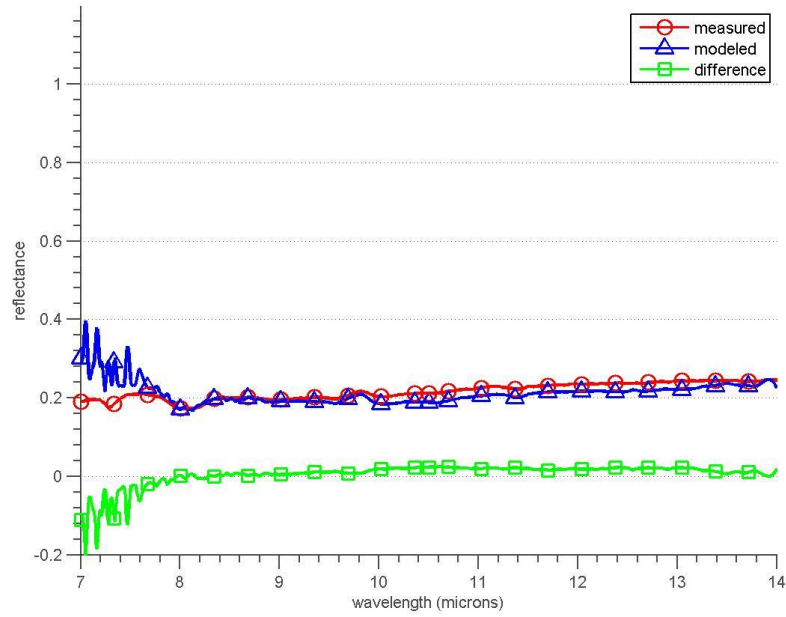


Figure C11. The measured and reverse modeled HDR at M6 (medium emissivity material) are shown for the diffuse-only reverse model. The measured HDR shown is interpolated to match the observation angle which was used for the model.

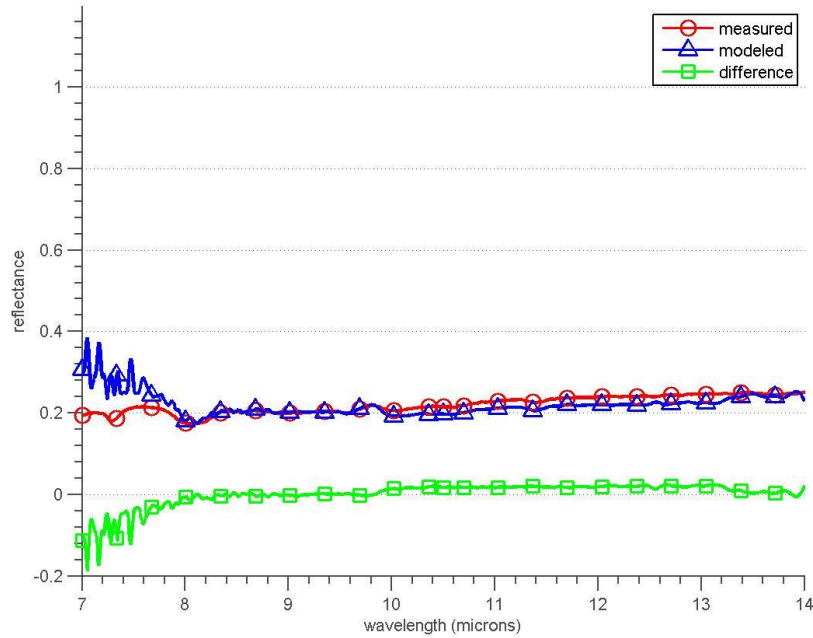


Figure C12. The measured and reverse modeled HDR at M14 (medium emissivity material) are shown for the diffuse-only reverse model. The measured HDR shown is interpolated to match the observation angle which was used for the model.

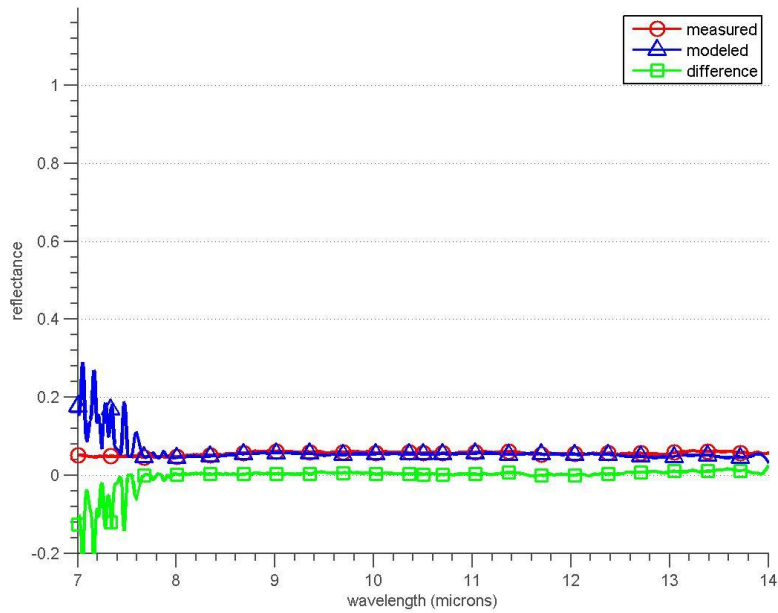


Figure C13. The measured and reverse modeled HDR at M7 (black vehicle paint) are shown for the diffuse-only reverse model. The measured HDR shown is interpolated to match the observation angle which was used for the model.

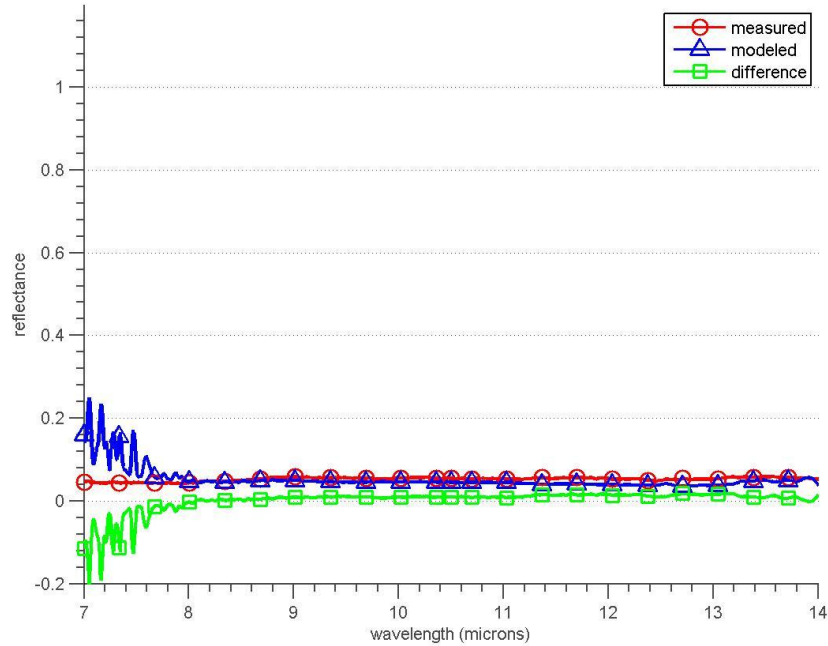


Figure C14. The measured and reverse modeled HDR at M15 (black vehicle paint) are shown for the diffuse-only reverse model. The measured HDR shown is interpolated to match the observation angle which was used for the model.

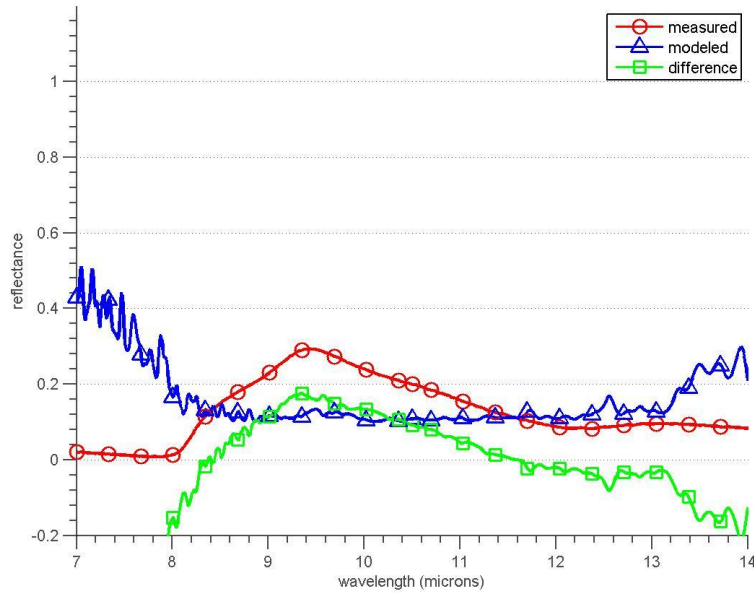


Figure C15. The measured and reverse modeled HDR at M8 (laminated safety glass) are shown for the diffuse-only reverse model. The measured HDR shown is interpolated to match the observation angle which was used for the model.

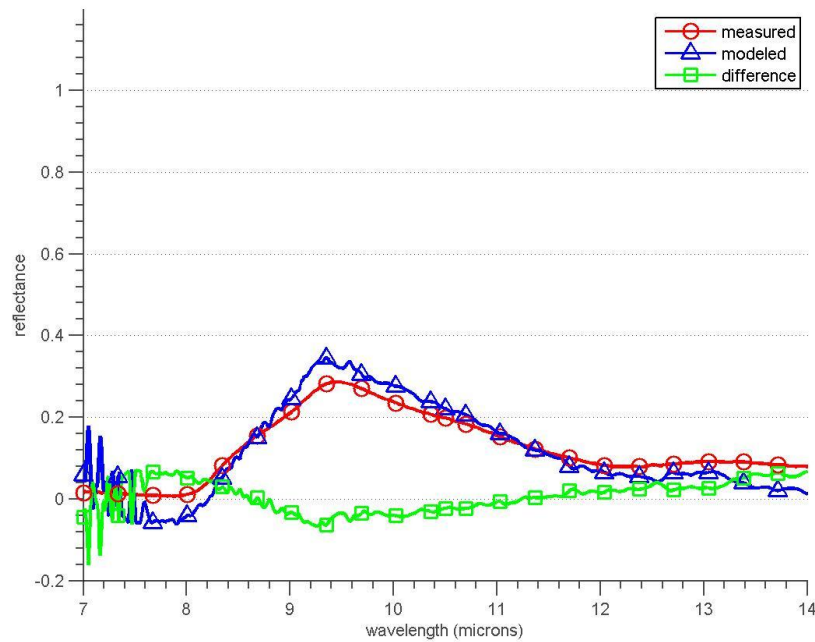


Figure C16. The measured and reverse modeled HDR at M16 (laminated safety glass) are shown for the diffuse-only reverse model. The measured HDR shown is interpolated to match the observation angle which was used for the model.

Bibliography

- Butler, Samuel D., Michael A. Marciniak, and Joseph Meola. "Modeling Effects of Bidirectional Reflectance Distribution Function on Remote Sensing in the Long Wave Infrared Spectrum." SPIE 9222 (2014): n. pag. 2015.
- Callieco, F.Dell'Acqua, F. "A Comparison Between Two Radiative Transfer Models For Atmospheric Correction Over A Wide Range Of Wavelengths." *International Journal Of Remote Sensing* 32.5 (2011): 1357-1370. *Computer Source*. 8 Jan. 2015.
- Dereniak, Eustace L., and G. D. Boreman. *Infrared Detectors and Systems*. New York: Wiley, 1996.
- Durikovic, Roman, and Andrej Mihalik. "Modeling the BRDF from Spectral Reflectance Measurements of Metallic Surfaces." *Applied Surface Science* 312 (2014): 87-90. 2013.
- Earp, A., G. Smith, and J. Franklin. "Simplified BRDF Of A Non-Lambertian Diffuse Surface." *Lighting Research & Technology* 39.3 (2007): 265-281. *Science & Technology Collection*. 8 Jan. 2015.
- Eismann, Michael Theodore. "Atmospheric Compensation." *Hyperspectral Remote Sensing*. Bellingham WA: SPIE, 2012.
- Guanter, LuisRichter, RudolfKaufmann, Hermann. "On The Application Of The MODTRAN4 Atmospheric Radiative Transfer Code To Optical Remote Sensing." *International Journal Of Remote Sensing* 30.6 (2009): 1407-1424. *Computer Source*. 8 Jan. 2015.
- Hecht, Eugene. *Optics. Hecht*. Reading MA: Addison-Wesley, 1998.
- Ientilucci, Emmett J., and Michael Gartley. "Impact of BRDF on Physics Based Modeling as Applied to Target Detection in Hyperspectral Imagery." SPIE 7334 (2009): n. pag. 2014.
- Kuester, Theres, Daniel Spengler, Jean-Francois Barczi, Karl Segl, Patrick Hostert, and Hermann Kaufmann. "Simulation of Multitemporal and Hyperspectral Vegetation Canopy Bidirectional Reflectance Using Detailed Virtual 3-D Canopy Models." *IEEE Transactions on Geoscience and Remote Sensing* 52.4 (2014): 2096-108. 2014.
- Machida, Takashi, Haruo Takemura, and Naokazu Yokoya. "Inverse Reflectometry for Real Objects with Diffuse and Specular Interreflections." *Electronics and Communications in Japan (Part II: Electronics)* 90.1 (2007): 50-60.
- Platnick, Steven, and Juan M. Fontenla. "Model Calculations of Solar Spectral Irradiance in the 3.7-m Band for Earth Remote Sensing Applications." *Journal of Applied*

Meteorology and Climatology 47.1 (2008): 124-34.

Sae Byul, Kang, Lee Woo Il, and Lee Joon Sik. "An Effective Calculation Method For Radiative Exchange In An Enclosure With Specular Surfaces." *Numerical Heat Transfer: Part A -- Applications* 50.9 (2006): 865-881. *Science & Technology Collection*. 8 Jan. 2015.

Shell, James R., II. "Bidirectional Reflectance: An Overview with Remote Sensing Applications & Measurement Recommendations." *Caltech*. 2004. Center for Imaging Science. 2014 <<http://web.gps.caltech.edu/~vijay/Papers/BRDF/shell-04.pdf>>.

SOC-100 User's Manual Hemispherical Directional Reflectometer (HDR). San Diego: Surface Optics Corporation, 2009.

Torrance, K.E., and E.M. Sparrow. "Theory for Off-Specular Reflection From Roughened Surfaces." *Journal of the Optical Society of America*, Vol. 57, No. 9, September 1967.

Wilson, Marcus, Ross Elliott, and Keith Youern. "The Use of Measured Sky Radiance Data to Improve Infrared Signature Modelling." *International Journal of Remote Sensing* 29.7 (2008): 1929-944.

Wöhler, Christian, and Pablo d'Angelo. "Stereo Image Analysis Of Non-Lambertian Surfaces." *International Journal Of Computer Vision* 81.2 (2009): 172-190. *Academic Search Premier*. 8 Jan. 2015.

Xu, Tao, and Yan Yan Suo. "Numerical Modeling of the Spectral and Diffuse Reflectance of Silicon Photodiodes." *Nonlinear Optics and Quantum Optics* 41 (2009): 125-35.

Yang, Guijun, Qinhua Liu, Qiang Liu, Wenjiang Huang, and Jihua Wang. "Simulation of High-resolution Mid-infrared (3–5 μm) Images Using an Atmosphere Radiative Transfer Analytic Model." *International Journal of Remote Sensing* 30.22 (2009): 6003-022.

Vita

Second Lieutenant Dimitar M. Stoyanov graduated from Central High School in St. Joseph, Missouri, and promptly enlisted in the United States Air Force, where he served as an Electrical & Environmental Systems Specialist at Offutt AFB, NE. He entered undergraduate studies at the University of Nebraska-Omaha, where he studied for a year and a half before he transferred, as a full-time student, to the Missouri University of Science and Technology, from which he acquired a Bachelor of Science in Physics in May 2013. He was commissioned through Officer Training School, Maxwell AFB, AL, in August 2013.

His first assignment as a commissioned officer was at Wright-Patterson AFB as a student in MS Applied Physics at the Air Force Institute of Technology. Upon graduation, he will be assigned to the Air Force Research Laboratory at Eglin AFB, FL.

REPORT DOCUMENTATION PAGE				Form Approved OMB No. 074-0188	
<p>The public reporting burden for this collection of information is estimated to average 1 hour per response, including the time for reviewing instructions, searching existing data sources, gathering and maintaining the data needed, and completing and reviewing the collection of information. Send comments regarding this burden estimate or any other aspect of the collection of information, including suggestions for reducing this burden to Department of Defense, Washington Headquarters Services, Directorate for Information Operations and Reports (0704-0188), 1215 Jefferson Davis Highway, Suite 1204, Arlington, VA 22202-4302. Respondents should be aware that notwithstanding any other provision of law, no person shall be subject to a penalty for failing to comply with a collection of information if it does not display a currently valid OMB control number.</p> <p>PLEASE DO NOT RETURN YOUR FORM TO THE ABOVE ADDRESS.</p>					
1. REPORT DATE (DD-MM-YYYY) 13-03-2015		2. REPORT TYPE Master's Thesis		3. DATES COVERED (From - To) October 2013 - March 2015	
TITLE AND SUBTITLE INVESTIGATION OF FIELD-COLLECTED DATA USING DIFFUSE AND SPECULAR, FORWARD AND REVERSE RADIATIVE TRANSFER MODELS				5a. CONTRACT NUMBER	
				5b. GRANT NUMBER	
				5c. PROGRAM ELEMENT NUMBER	
6. AUTHOR(S) Stoyanov, Dimitar M., Second Lieutenant, USAF				5d. PROJECT NUMBER	
				5e. TASK NUMBER	
				5f. WORK UNIT NUMBER	
7. PERFORMING ORGANIZATION NAMES(S) AND ADDRESS(S) Air Force Institute of Technology Graduate School of Engineering and Management (AFIT/ENP) 2950 Hobson Way, Building 640 WPAFB OH 45433-8865				8. PERFORMING ORGANIZATION REPORT NUMBER AFIT-ENP-MS-15-M-100	
9. SPONSORING/MONITORING AGENCY NAME(S) AND ADDRESS(ES) Sensors Directorate, Air Force Research Laboratory 2241 Avionics Circle, Area B, WPAFB OH 45433 (937)528-8200 Michael.Eismann@us.af.mil ATTN: Dr. Michael Eismann				10. SPONSOR/MONITOR'S ACRONYM(S) AFRL/RV	
				11. SPONSOR/MONITOR'S REPORT NUMBER(S)	
12. DISTRIBUTION/AVAILABILITY STATEMENT DISTRIBUTION STATEMENT A. APPROVED FOR PUBLIC RELEASE; DISTRIBUTION UNLIMITED.					
13. SUPPLEMENTARY NOTES This material is declared a work of the U.S. Government and is not subject to copyright protection in the United States.					
14. ABSTRACT The effect of specular and diffuse properties of a set of eight materials is investigated when used in diffuse-only and diffuse-specular radiative transfer models in the wavelength range of 7-14µm. The materials were selected and measured by the Sensors Directorate, Air Force Research Laboratory (AFRL/RV) as a set of panels in two orientations, flat and 45° with respect to the ground, and ranging in reflective and specular properties. The field-collected data includes down-welling spectral radiance, ground spectral radiance, panel temperatures, and panel spectral reflected radiance. Aside from field data, the chosen radiative transfer models utilize laboratory-collected data to calculate the spectral reflected radiance from each panel. The laboratory-collected data is comprised of spectral hemispherical, specular, and diffuse directional reflectance (HDR, SDR, and DDR) at incident angles of 20°, 30°, 40°, 45°, 50°, 60°, and 70°, as collected by an SOC-100 HDR Reflectometer from Surface Optics Corporation. The modeled spectral reflected radiances are compared to field-collected spectral reflected radiances in order to gauge each radiative transfer model for its accuracy in modeling each panel. Additionally, a diffuse-only reverse radiative transfer model is used to model the spectral HDR of the materials, and is gauged against lab-collected spectral reflectance data.					
15. SUBJECT TERMS Lambertian, diffuse, specular, specularity, BRDF, reflectance					
16. SECURITY CLASSIFICATION OF:			17. LIMITATION OF ABSTRACT UU	18. NUMBER OF PAGES 133	19a. NAME OF RESPONSIBLE PERSON Dr. Michael A. Marciniak, AFIT/ENP
a. REPORT U	b. ABSTRACT U	c. THIS PAGE U			19b. TELEPHONE NUMBER (Include area code) (937) 255-3636, ext 4529 Michael.Marciniak@afit.edu

Standard Form 298 (Rev. 8-98)
Prescribed by ANSI Std. Z39-18